Modèles avancés pour le recalage d'images multimodales

Mohamed Lajili

LAMSIN
Ecole Nationale d'Ingénieurs de Tunis
Université de Tunis El Manar
Campus Universitaire Farhat Hached
ROMMANA, 1068 Tunis

Institut de Recherche en Informatique,
Mathématiques, Automatique et Signal
Université de Haute–Alsace
18 rue des frères Lumière
68093 Mulhouse

Thèse de Doctorat

Spécialité

Mathématiques Appliquées

Présentée par

MOHAMED LAJILI

Pour obtenir le grade de

Docteur de l'Université de Haute–Alsace

et l'école nationale d'ingénieurs de tunis

Modèles avancés pour le recalage d'images multimodales

Soutenue le 29 septembre 2023 *devant le jury composé de :*

Rapporteur :	Frédéric Hecht	*Professeur (émérite),*	*Université de la Sorbonne*
Rapporteur :	Maatoug Hassine	*Professeur,*	*Université de Monastir*
Examinatrice :	Renata Bunoiu	*Maître de Conférences HDR,*	*Université de Lorraine*
Examinateur :	Privat Yannick	*Professeur,*	*Université de Strasbourg*
Directeur de thèse :	Zakaria Belhachmi	*Professeur,*	*Université de Haute–Alsace*
Directeur de thèse :	Maher Moakher	*Professeur,*	*Université de Tunis El Manar*

Thesis Plan

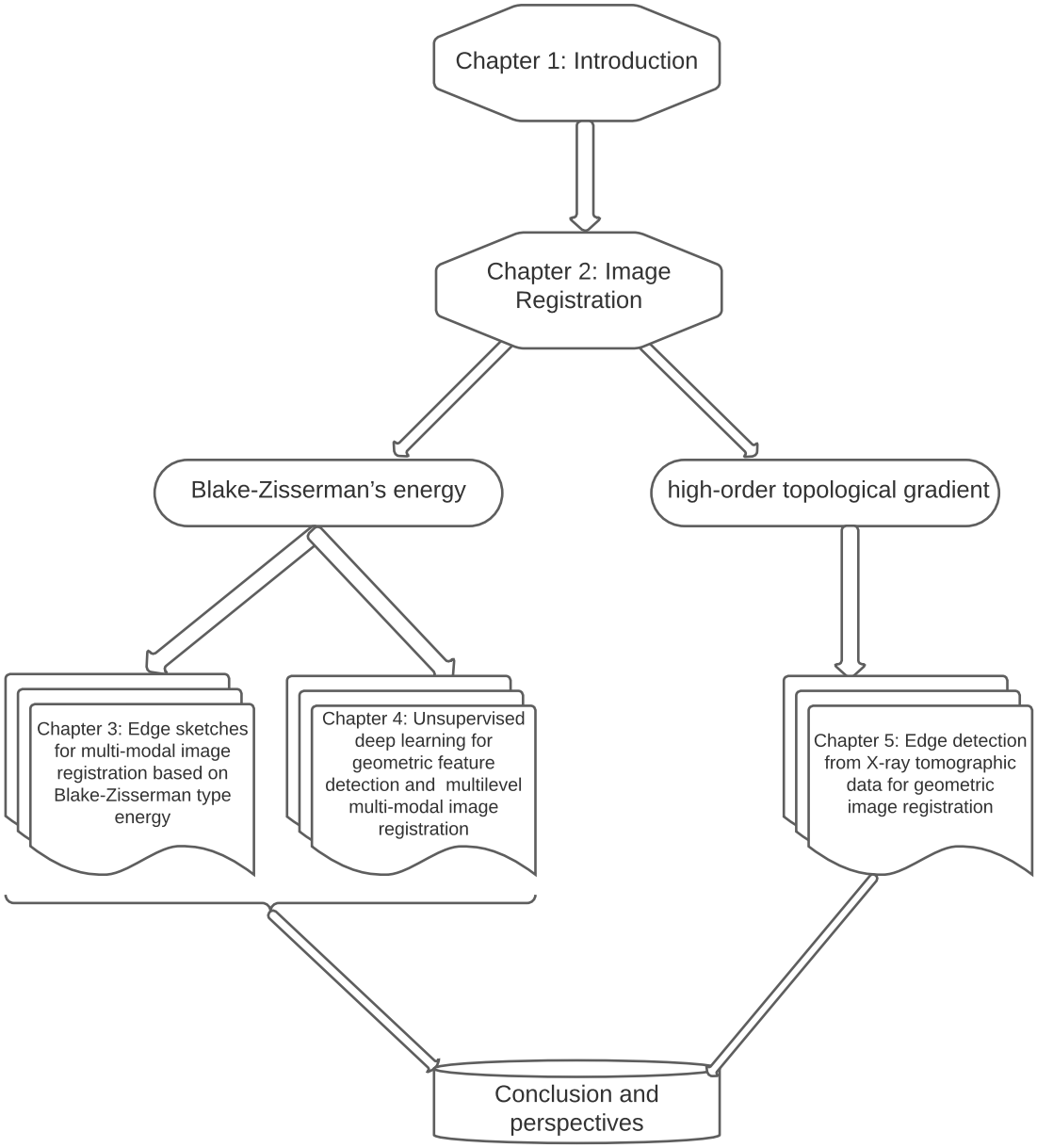
Chapter 1: Introduction
Chapter 2: Image Registration
Blake-Zisserman's energy
high-order topological gradient
Chapter 3: Edge sketches for multi-modal image registration based on Blake-Zisserman type energy
Chapter 4: Unsupervised deep learning for geometric feature detection and multilevel multi-modal image registration
Chapter 5: Edge detection from X-ray tomographic data for geometric image registration
Conclusion and perspectives

Abstract

Image registration is a crucial task in medical image processing, as it allows correcting for positional and orientation differences between images acquired from different modalities or at different times. This correction is necessary to merge the images into a single coherent image, to facilitate data visualization and analysis, and to improve the accuracy of quantitative measurements.

There are different methods of image registration, each with its own advantages and disadvantages. The most commonly used image registration methods are feature-based methods such as histograms and textures, edge-based methods, and point-based methods that use specific character in the images to align them.

In this thesis we present three important contributions to image registration. The first part introduces a new similarity term based on the geometric information extracted from the images. This term uses the Blake-Zisserman energy to extract geometric information such as edges and fine structures from the images. This new registration method improves performance in terms of precision and robustness compared to classical methods.

The second part of this thesis introduces an effective approach for unsupervised multilevel image registration by leveraging geometric information extracted using the Blake-Zisserman energy. This energy enables the detection of geometric information from two images during the training. We propose a neural network architecture that predicts the geometric information of an image. This neural network is guided by the Blake-Zisserman energy, allowing us to achieve unsupervised detection of geometric information. Subsequently, we use this geometric information to define a second neural network dedicated to the process of multi-modal image registration. In order to achieve efficient registration, we propose a novel deep neural network architecture that performs multilevel registration.

The third part of this thesis focuses on constructing a robust similarity term for deformable image registration models from tomographic data. The topological gradient associated with a second-order derivative is calculated for the proposed cost function. This gradient is then used to construct an efficient and robust similarity term that can handle contrast variations and significant deformations. This registration method is tested on tomographic data, and the results demonstrate the effectiveness and efficiency of this method.

Résumé

Le recalage d'images est une tâche cruciale en traitement d'images médicales, car elle permet de corriger les différences de position et d'orientation entre les images acquises à partir de différentes modalités ou à différents moments. Cette correction est nécessaire pour fusionner les images en une seule image cohérente, faciliter la visualisation et l'analyse des données, et améliorer la précision des mesures quantitatives. Il existe différentes méthodes de recalage d'images, chacune ayant ses propres avantages et inconvénients. Les méthodes de recalage d'images les plus couramment utilisées sont les méthodes basées sur les caractéristiques telles que les histogrammes et les textures, les méthodes basées sur les contours et les méthodes basées sur les points d'intérêts qui utilisent des points spécifiques de l'image pour aligner les images.

Cette thèse présente trois contributions importantes pour le recalage d'images. La première partie introduit un nouveau terme de similarité basé sur les informations géométriques extraites des images. Ce terme utilise l'énergie de Blake-Zisserman pour extraire les informations géométriques telles que les contours et les structures fines des images. Cette nouvelle méthode de recalage améliore les performances en termes de précision et de robustesse, par rapport aux méthodes classiques.

La deuxième partie introduit une approche efficace de recalage d'images multiniveaux basée sur l'apprentissage profond non supervisé, en exploitant les informations géométriques extraites à l'aide de l'énergie de Blake-Zisserman. Cette énergie permet de détecter les informations géométriques de deux images lors de l'entraînement. On construit un réseau de neurones qui prédit les informations géométriques d'une image. Ce réseau de neurones est guidé par l'énergie de Blake-Zisserman, ce qui nous permet d'obtenir une détection des informations géométriques dans le cas non supervisé. Ensuite, on utilise ces informations géométriques pour définir un deuxième réseau de neurones dédié au processus de recalage d'images multimodale. Afin d'obtenir un recalage plus précis et efficace, on présente une nouvelle architecture de réseau neuronal profond qui réalise un recalage multiniveaux.

La troisième partie se concentre sur la construction d'un terme de similarité robuste pour des modèles de recalage d'images à partir de données tomographiques. Le gradient topologique associé à une dérivée de second ordre est calculé pour la fonction coût. Ce gradient est ensuite utilisé pour construire un terme de similarité efficace et robuste qui permet de traiter les variations de contraste et les déformations importantes. Cette méthode de recalage est évaluée sur des données tomographiques et les résultats montrent l'efficacité et l'efficience de cette méthode.

Remerciements

*J*e tiens tout d'abord à remercier en premier lieu mes directeurs de thèse: le professeur Maher Moakher et le professeur Zakaria Belhachmi, pour leur encadrement, leur complémentarité, et pour leur aide continu. Leur modestie, simplicité et patience m'ont parfois fait oublier qu'ils étaient mes directeurs de thèse et cela m'a permis d'avoir confiance en ce que je faisais. Je les remercie pour ce qu'il m'a apporté sur le plan scientifique, pour ses disponibilités et ses bonnes humeurs. Je suis fier d'avoir pu partager avec eux mes premiers moments d'euphorie générés par la recherche.

*U*n énorme merci à Anis Theljani, chargé de recherche, qui m'a aidé dans mes recherches, pour ce qu'il m'a apporté sur le plan scientifique, pour ses disponibilités et ses bonnes humeurs, pour toutes les heures passées à la relecture attentive de mes différents travaux quel que soit numériques ou bien théoriques. Je tiens ensuite à remercier Badreddine Rjaibi, Maître assistant à l'école nationale d'ingénieurs de Tunis, et Didier Auroux, Professeur à l'université de Nice Sophia Antipolis, pour ses collaborations dans des productions écrites.

*J*e tiens à exprimer mes sincères remerciements aux rapporteurs, Monsieur Hecht Frédéric, Professeur à l'université de la Sorbonne et Monsieur Hassine Maatoug Professeur à l'université de Monastir, d'avoir accepté d'être membres du jury, d'avoir eu le courage de lire ce manuscrit attentivement et pour leurs soutiens ainsi que leurs commentaires utiles. Je suis également extrêmement reconnaissant à Madame Bunoiu Renata Maître de conférences à l'université de Lorraine, et Monsieur Yannick Privat, Professeur à l'université de Strasbourg, pour avoir également accepté de faire partie de mon comité de suivi de thèse.

*C*e travail a été mené en étroite collaboration entre le Laboratoire de Modélisation Mathématique et Numérique dans les Sciences de l'Ingénieur (LAMSIN, Tunis) et le département de mathématiques de l'IRIMAS (Mulhouse) dans le cadre d'une thèse en cotutelle. la période que j'ai passée au sein de ces deux laboratoires a été pour moi très enrichissante.

*E*nsuite, je salue tous les membres du laboratoires LAMSIN et le département de mathématiques de l'IRIMAS qui ont contribué à y faire régner une ambiance cardiale, et qui ont, de près ou de loin, aidé à rendre ce travail possible, que ce soit par des idées ou par des encouragements.

*E*nfin, je souhaite également adresser un énorme merci tout particulier à ma famille: ce travail n'aurait jamais vu le jour sans vos encouragements, ma réussite est également la vôtre car nous étions toujours unis. De plus, mes amis vous étiez toujours à côtés dans les moments difficiles et de joie aussi.

Contents

List of Figures

List of Tables

1 Introduction

1.1 Motivation

Dans les années 1920, Harry G. Bartholomew et Maynard D. McFarlane effectuent la première tâche en traitement d'images qui s'appelle la numérisation d'image afin d'envoyer des fax de Londres à New York. Après, vers la fin de la Seconde Guerre mondiale, le traitement d'images a commencé comme un domaine de recherche pour les informaticiens et ne semble pas susciter l'intérêt des mathématiciens. Progressivement, il est devenu hautement interdisciplinaire et a attiré beaucoup d'attention de la part de la communauté mathématique. De nos jours, le traitement d'images joue un rôle très important pour les recherches en mathématiques. Jusqu'à maintenant, diverses approches mathématiques, dans des cadres différents, sont disponibles pour traiter et analyser les images comme les méthodes de la transformée de Fourier, la modélisation statistique et stochastique [AKR97; GG84] et les méthodes des équations aux dérivées partielles (EDP)[AKA06; Mas02b; Wei98]. Généralement, il existe différents types de traitement d'images tels que:

- La restauration d'images afin de corriger les distorsions dues lors des étapes de l'acquisition ou de la transmission d'images.

- La segmentation d'images qui consiste à rassembler des pixels entre eux suivant des critères prédéfinis dont le but est de partitionner l'image.

- Le recalage d'images qui consiste à trouver une transformation géométrique qui aligne les objets physiquement homologues.

De plus, les domaines d'application de ces différents types de traitement d'images sont très nombreux. Parmi eux il y a deux principaux domaines: le domaine militaire (la photo-interprétation, la télédétection à partir d'images satellites, etc.) et le domaine médical (scanner, imagerie par résonance magnétique (IRM), échographie, radiographie, etc.). La recherche médicale devient un domaine de recherche en traitement d'images à partir les années 1990 afin de mettre à la disposition des médecins des images améliorées pour un meilleur diagnostic. En effet, l'objectif du traitement d'images médicales est l'amélioration de l'image, l'extraction des informations dans l'image comme la présence des tumeurs, la comparaison des

images et la reconstruction 3D. C'est le cas illustré dans l'exemple présenté dans la Figure 1.1

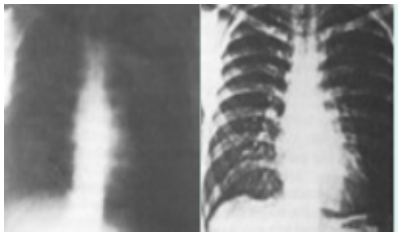

(a) Restauration d'images: Amélioration d'une image

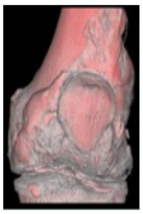

(b) Reconstruction 3D

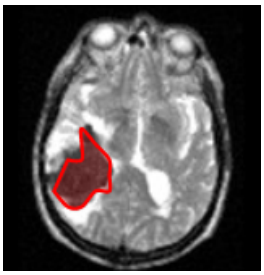

(c) Segmentation: Extraction d'information dans l'image

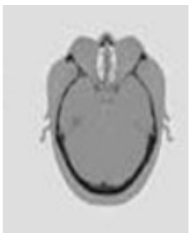

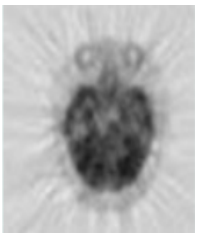

(d) Recalage et fusion: Comparaison de deux images

Fig. 1.1 Les différents objectifs en traitement d'images médicales. https://slideplayer.fr/slide/1324048

Du point de vue mathématique, les différentes tâches de traitement d'images font partie d'une vaste classe de problèmes mathématiques appelée problèmes inverses. En fait, le défi consiste à récupérer une image "originale" souhaitée à partir d'une image observée. Cette dernière souffre généralement d'imperfections indésirables telles que du bruit, des pertes et même des flous produits par les dispositifs d'acquisition qui rendent la solution associée à une fonction qui n'est pas exactement calculable ni unique ou le procédé est instable. Afin d'expliquer les problèmes de traitement d'images comme étant des problèmes inverses, nous devons d'abord préciser brièvement la différence entre un problème inverse et un problème direct. Ainsi, comprendre les concepts de base des problèmes inverses et de leur caractère 'bien' ou 'mal posé'.

Dans cette thèse, on se concentre sur le problème du recalage d'images qui est l'un des problèmes courants en imagerie médicale. En effet, durant les étapes d'enregistrement, de reconstruction et de transmission de l'image, une déformation géométrique est possible. Le recalage d'images peut être vu comme un problème

d'optimisation qui consiste à trouver une image qui correspond à sa version transformée (référence). On propose trois nouvelles approches variationnelles pour résoudre ce problème en se basant sur les informations géométriques (contours et structures fines) détectées à l'aide de deux méthodes: l'énergie de Blake-Zisserman et le gradient topologique. Ces informations sont utilisées pour définir un terme de similarité approprié dans les fonctionnelles des approches proposées.
Dans le deuxième chapitre, on donne une introduction générale au recalage d'images. On discute les concepts de base du recalage d'images, les différents types de transformations couramment utilisées pour aligner les images ainsi que les méthodes numériques. Dans le troisième chapitre, on introduit un nouveau terme de similarité pour le recalage d'images basé sur les informations géométriques (contours et structures fines) extraites à partir des images en utilisant l'énergie de Blake-Zisserman. Dans le quatrième chapitre, on aborde le problème du recalage d'images en utilisant la technique de l'apprentissage profond. On propose la construction de deux réseaux de neurones dans un contexte d'apprentissage non supervisé. Le premier réseau a pour objectif de prédire les informations géométriques présentes dans les deux images, c'est à dire l'image de référence et l'image source. Ce réseau analyse les caractéristiques géométriques des images et les représente de manière appropriée. Le deuxième réseau utilise ces informations géométriques prédites afin d'effectuer le recalage entre les deux images. Son rôle est de prédire le champ de déformation qui permet d'aligner les deux images de manière optimale. En combinant ces deux réseaux de neurones, on est en mesure de résoudre le problème du recalage d'images de manière efficace et précise grâce à l'apprentissage profond. Dans le cinquième chapitre, on calcule le gradient topologique pour le problème de Laplace à partir des données tomographiques qui nous permet de détecter les informations géométriques d'une image. En utilisant cette approche, on définit une mesure de similarité appropriée basée sur les informations géométriques (contours et structures fines) détectées par un opérateur d'ordre élevé pour le processus de recalage d'images.

Avant de détailler le problème du recalage d'images et notre contribution dans cette thèse, ce premier chapitre est consacré à la description des différents types de traitement d'images et présente quelques notions fondamentales pour ce domaine du point de vue mathématique.

1.2 Problème direct et problème inverse

D'une part, un problème direct consiste à déterminer des effets connaissant des causes. Mathématiquement, cela revient à déterminer une (des) image(s) qui correspond(ent) à un (des) antécédent(s) donné(s) par une fonction ou bien par

un opérateur bien défini. En effet, soient f une fonction et a une valeur donnée de x, le problème direct consiste à trouver y pour une valeur de x, connaissant f. Ce problème peut s'exprimer simplement comme la résolution de l'équation

$$y = f(a). \tag{1.1}$$

Les problèmes directs sont généralement uniques, c'est-à-dire qu'il n'y a qu'une seule solution possible pour un problème donné. Ils sont également importants en mathématiques et en physique, notamment dans les domaines de la mécanique, de l'électromagnétisme, de la thermodynamique, de la géométrie, et de l'optimisation. Les techniques de résolution de systèmes d'équations, du calcul numérique et de modélisation mathématique sont souvent utilisées pour résoudre les problèmes directs.

D'autre part, un problème inverse est l'inverse du problème dit 'direct' (C'est illustré dans l'exemple affiché dans la Figure 1.2). C'est une situation dans laquelle le but est de déterminer les causes connaissant les effets. En effet, essayons de traduire de façon mathématique à l'aide d'une équation: soient f une fonction connue et b une valeur donnée de y. Un problème inverse consiste à trouver l'antécédent x pour une valeur de y et cela revient à résoudre l'équation suivante:

$$f(x) = b. \tag{1.2}$$

Les solutions d'un problème inverse sont souvent non uniques, c'est-à-dire qu'il y a plusieurs causes possibles pour un même effet. Les problèmes inverses sont fréquents en mathématiques, en physique, en ingénierie et en biologie, et sont utilisés pour résoudre des problèmes tels que la reconnaissance de formes, la compression d'image, la reconstruction d'image, la reconstruction 3D, la localisation d'objet, la traçabilité, la géolocalisation, etc. Mais le plus souvent, la plupart des problèmes sont des problèmes inverses mal posés. Une importante notion de 'bien posé' pour un problème inverse a été définie par Hadamard [Had53]. Les algorithmes de traitement d'images et de signal sont souvent utilisés pour résoudre les problèmes inverses.

Définition 1.2.1 *Un problème est dit bien posé si et seulement si les trois conditions suivantes sont vérifiées:*

- *La solution existe.*
- *La solution est unique.*
- *La solution dépend continûment des données.*

Si (au moins) une des conditions précédentes échoue, on dit que le problème est mal posé au sens d'Hadamard.

En résumé, les problèmes inverses et les problèmes directs sont des concepts importants en mathématiques et dans divers domaines de la science et de la technologie, où ils sont utilisés pour résoudre des problèmes concrets de manière efficace.

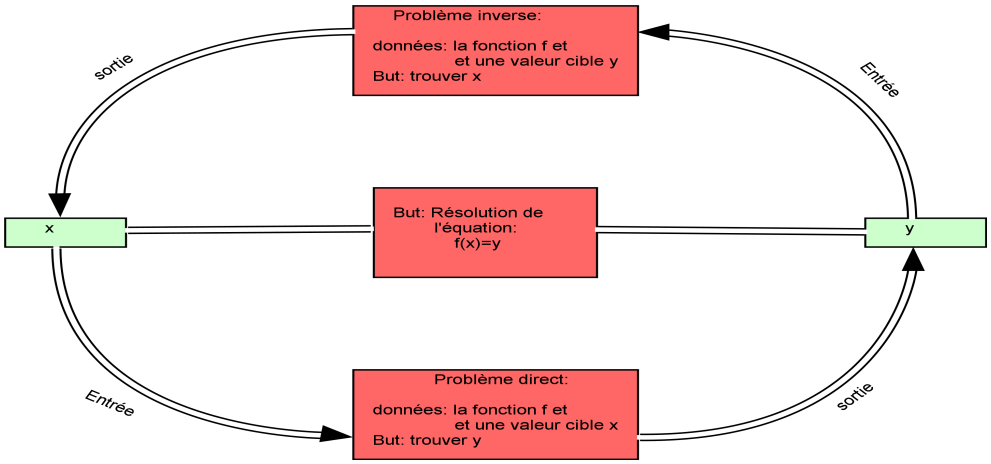

Fig. 1.2 Problème direct contre problème inverse.

1.3 Image numérique

Une image numérique consiste en unités élémentaires appelées pixels "(picture elements)" qui représentent les plus petits éléments constitutifs de l'image et qui représentent différentes nuances de couleur et de luminosité. Ces pixels sont répartis sur une grille rectangulaire où la position de chaque pixel est décrite par un couple (i, j) et prend la valeur $I(i, j)$ qui représente l'intensité, ou généralement sa couleur. Mathématiquement, l'image est considérée comme étant une fonction:

$$\begin{aligned} I : \mathbb{R} \times \mathbb{R} &\longrightarrow \mathbb{R} \ (ou \ \mathbb{R}^3) \\ (x, y) &\longrightarrow I(x, y) \end{aligned} \tag{1.3}$$

Les images numériques peuvent être créées à partir de nombreuses sources, notamment des photographies, des dessins numériques, des images capturées par des caméras vidéo et des caméras numériques, des images générées par ordinateur, et bien plus encore. De plus, il existe de nombreux formats d'images numériques, chacun ayant ses propres avantages et inconvénients en termes de qualité d'image, de taille de fichier et de compatibilité avec les différents logiciels et appareils. Les images numériques peuvent être modifiées, retouchées et améliorées et par la suite on peut faire des ajustements tels que la correction des couleurs, le recalage, la suppression des imperfections, l'ajout de filtres, et bien plus encore.

Les images numériques sont utilisées dans de nombreux domaines, tels que la publicité, le cinéma, les jeux vidéo, la reconnaissance de formes, la robotique, la médecine, la cartographie, la géolocalisation, la télédétection, etc. Les algorithmes de traitement d'images et de reconnaissance d'image sont utilisés pour extraire des informations utiles à partir des images numériques. Généralement, on distingue trois types d'images (Voir Figure 1.3):

- Image binaire: chaque pixel ne peut avoir comme valeur d'intensité que 0 ou 1.
- Image en niveaux de gris: les intensités des pixels prennent des valeurs dans l'intervalle $[0, 255]$.
- Image couleur: les intensités des pixels sont des vecteurs dans $[0, 255]^3$.

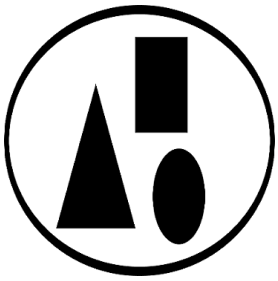

(a) Image binaire

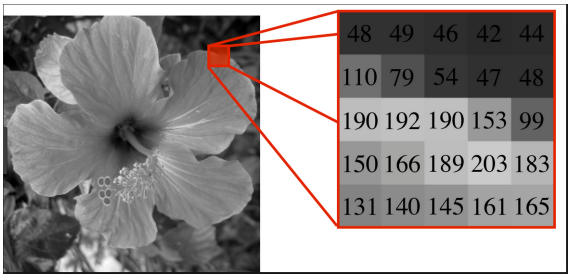

(b) Image en niveaux de gris

(c) Image couleur

Fig. 1.3 Les différents types d'images.
http://images.math.cnrs.fr/Le-traitement-numérique-des-images.html

Généralement, les images jouent un rôle très important dans de nombreux domaines et il existe différents types de traitements d'images. Dans la suite, nous allons brièvement rappeler quelques tâches courantes dans le domaine du traitement d'images.

1.4 Restauration d'images

La restauration d'images est un problème très important dans différents domaines tels que l'imagerie médicale, l'astronomie, la restauration des films, ... [ST90].

Ce problème consiste à corriger les distorsions causées par différents phénomènes (bruit, bougé de l'appareil photographique, ...) et qui sont introduites lors des étapes de l'acquisition ou de la transmission d'images.
Mathématiquement, étant donné deux images I_0 et I qui sont respectivement l'image inconnue à restaurer, et l'image observée qui est bruitée, le but est de trouver I_0 à partir de l'équation:

$$I = \mathcal{K}(I_0), \tag{1.4}$$

où $\mathcal{K}$ est un **opérateur de dégradation** qui est généralement inconnu. L'opérateur $\mathcal{K}$ dépend du type de dégradation et peut prendre plusieurs expressions. Dans la suite, on donne quelques exemples de $\mathcal{K}$:

- **Débruitage d'image dans le cas additif:** Dans ce cas, l'opérateur $\mathcal{K}$ s'écrit sous la forme:

  $$\mathcal{K}(I_0) = I_0 + \eta, \tag{1.5}$$

  où η est un bruit additif blanc qui suit la loi normale.

- **Débruitage d'image dans le cas multiplicatif:** Dans ce cas, l'opérateur $\mathcal{K}$ s'écrit sous la forme:

  $$\mathcal{K}(I_0) = I_0 \times \eta, \tag{1.6}$$

  où η est un bruit multiplicatif qu'on peut le désigner aussi bruit impulsionnel.

- **Déconvolution:** Le but est d'inverser les effets d'une convolution d'image par un opérateur de convolution R qui peut être connu ou non. Ce problème est modélisé par l'équation:

  $$\mathcal{K}(I_0) = RI_0 + \eta. \tag{1.7}$$

  Si l'opérateur R est inconnu, on parle dans ce cas de la **déconvolution**. Le problème est dit déconvolution aveugle si R est imparfaitement connu.

Problème inverse

La restauration d'image est typiquement un problème inverse mal posé au sens d'Hadamard. Dans notre problème (1.4), le caractère mal posé est dû aux raisons suivantes:

- L'existence et/ou l'unicité des solutions ne sont pas assurées car l'opérateur $\mathcal{K}$ dans (1.4) n'est pas généralement inversible.

- Même si $\mathcal{K}$ est inversible, son inverse n'est pas toujours continu. Ceci rend la solution n'est pas stable vis-à-vis des petites perturbations sur les données.

Fig. 1.4 Restauration d'images. https://slideplayer.fr/slide/493624/

Approches variationnelles et régularisations

Une formulation mathématique équivalente au problème (1.4) consiste à trouver I_0 qui minimise l'énergie suivante:

$$\|\mathcal{K}I_0 - I\|_{\mathcal{Y}}^2, \tag{1.8}$$

avec $(\mathcal{Y}, \|\cdot\|_{\mathcal{Y}})$ est un espace de Banach à préciser. L'énergie (1.8) est mal posée. Pour remédier à ce problème, l'ajout d'un terme de régularisation à (1.8) est indispensable.

Régularisation

La régularisation revient à remplacer le problème (1.8) qui est mal posé par un problème qui est bien posé. Ceci consiste à chercher une approximation de la solution I_0 dans un ensemble de solutions qui dépendent du choix du terme de régularisation ajouté. Généralement, on considère le problème de minimisation suivant:

$$\min_{I_0 \in \mathcal{Y}} \left\{ \|\mathcal{K}I_0 - I\|_{\mathcal{Y}}^2 + \lambda J(I_0) \right\}. \tag{1.9}$$

La première partie dans (1.9) est le terme d'attachement aux données initiales. La deuxième partie $J(I_0)$ est dite terme de régularisation et qui contient généralement une information sur la régularité de la solution et qui représente l'effet de lissage du modèle. λ est un paramètre de régularisation.

Exemples

- **Modèle linéaire**: le modèle de diffusion isotrope pour le problème de restauration d'images est donné par:

$$\min_{I_0 \in H^1(\Omega)} \|I - \mathcal{K}I_0\|_2^2 + \frac{\lambda}{2}\int_\Omega |\nabla I_0|^2 dx.$$

Ce qui revient à résoudre l'équation d'Euler-Lagrange suivante:

$$\begin{cases} -\operatorname{div}(\lambda \nabla I_0) + \mathcal{K}^*\mathcal{K}I_0 = \mathcal{K}^*I & \text{dans } \Omega, \\ \dfrac{\partial I_0}{\partial n} = 0 & \text{sur } \partial\Omega, \end{cases} \tag{1.10}$$

où λ est une constante positive. L'EDP (1.10) a une propriété de diffusion isotrope. Par conséquent, ceci aboutit à un effet de lissage très fort qui ne distingue pas entre le bruit et les contours.

- **Modèle non linéaire**: le modèle de la **variation totale** [ROF92a] revient à minimiser l'énergie suivante:

$$\min_{I_0 \in BV(\Omega)} \|I - \mathcal{K}I_0\|_2^2 + \frac{\lambda}{2}\int_\Omega |\nabla I_0| dx,$$

où $BV(\Omega)$ est l'espace des fonctions à variations bornées. L'équation d'Euler-Lagrange correspond à la condition d'optimalité de ce problème de minimisation consiste à résoudre l'EDP suivante:

$$\begin{cases} -\operatorname{div}(\lambda \Phi(|\nabla I_0|)\nabla I_0) + \mathcal{K}^*\mathcal{K}I_0 = \mathcal{K}^*I & \text{dans } \Omega, \\ \Phi(|\nabla I_0|)\dfrac{\partial I_0}{\partial n} = 0 & \text{sur } \partial\Omega, \end{cases} \tag{1.11}$$

où $\Phi(|\nabla I_0|) = \dfrac{\nabla I_0}{|\nabla I_0|}$.

1.5 Segmentation d'images

La segmentation d'images est l'un des problèmes fondamentaux du traitement d'images. Durant les dernières années, la segmentation d'image s'est affirmée comme une voie de développement très prometteuse. Cette technique a été développée avec succès dans des domaines divers et très variés. La segmentation d'images consiste à partitionner une image donnée en région qui sont uniformes par rapport à certaines caractéristiques de l'image et éventuellement à extraire des objets à partir d'une image donnée (Extraction de points, lignes ou régions). Cette tâche peut être

effectuée avant ou après le recalage. Dans le domaine de l'imagerie médicale, le problème de la segmentation d'image a été l'un des défis majeurs. La segmentation est une condition préalable pour de nombreux types d'applications telles que la segmentation du cerveau [BM15], segmentation des organes abdominaux [Rot+17] et la segmentation cellulaire dans les images biologiques [RFB15a]. En outre, Mumford et Shah ont proposé dans [MS89] une approche variationnelle pour la segmentation d'image. Ainsi, la méthode du gradient topologique[Dro14; Hou+19] fournit un outil topologique d'optimisation efficace pour la segmentation d'image.

1.5.1 Segmentation d'images et détection des informations géométriques

La segmentation d'images et la détection de contours sont des tâches liées en imagerie, mais elles sont différentes.

La segmentation d'image consiste à diviser une image en différentes régions ou segments, chacun représentant une classe ou une structure particulière de l'image. Le but est de diviser une image en régions semblables en termes de propriétés telles que la couleur, la texture, la forme, etc. C'est une tâche de reconnaissance d'objet qui consiste à identifier et à séparer les différentes parties d'une image.

La détection des informations géométriques, par contre, consiste à identifier les bords ou les frontières entre les différents objets ou régions d'une image. Elle se concentre sur la localisation des contours d'un objet dans l'image, plutôt que sur la segmentation de l'image en région. Elle peut être considérée comme une étape préliminaire pour la segmentation d'images.

Pour conclure, on peut dire que la segmentation d'image est une tâche plus globale qui consiste à identifier et à séparer les différentes parties d'une image, tandis que la détection de contours se concentre sur la localisation des bords des objets dans l'image.

1.5.2 Gradient topologique

L'un des principaux défis en analyses d'images médicales est la détection de contours et des structures fines. Jusqu'à nos jours, plusieurs méthodes ont été développées, parmi ces méthodes on cite la méthode du gradient topologique qui a été introduite par Sokolowski [SZ99] et Masmoudi [Mas02a] pour l'optimisation de forme géométrique des objets. C'est une technique d'optimisation qui consiste à trouver

la géométrie optimale d'un objet vis-à-vis certains critères. Mathématiquement, ce problème peut être modélisé de la façon suivante:

$$\min_{\Omega \in E} J(\Omega, u_\Omega)$$

où E est un ensemble de domaines admissibles et u_Ω est la solution d'une équation aux dérivées partielles définie dans Ω. L'idée consiste à étudier le comportement asymptotique du critère $J(\cdot,\cdot)$ en perturbant le domaine initial Ω par la création de trous, supposés être des cercles (ou des ellipses) de tailles $(\varepsilon_i)_{i=1,\dots,N}$ et centrés en $(x_i)_{i=1,\dots,N}$. Par la suite, le gradient topologique qui permet de trouver la forme optimale nécessite l'obtention du développement asymptotique de la variation

$$J(\Omega \setminus \overline{\omega_\varepsilon}, u_\Omega) - J(\Omega, u_\Omega) = f(\varepsilon)G(x) + o(f(\varepsilon)),$$

lorsque $\varepsilon := \|(\varepsilon_1, \dots, \varepsilon_N)\|$ tend vers 0, avec $\omega_\varepsilon = x + \varepsilon\omega$, ω est un trou de taille unitaire et $f(\varepsilon)$ est une fonction positive qui tend vers 0.
Cette méthode a montré ces preuves en plusieurs travaux sur l'optimisation des formes et en particulier en traitement d'images tels que la restauration, la classification et la segmentation. Afin de trouver l'"asymptotique topologique", on peut utiliser la technique de troncature de domaine et une généralisation de la méthode adjointe [SAM03; Mas02a].

La méthode adjointe généralisée

Cette méthode a été introduite par M. Masmoudi dans [Mas02a].
Soit $\mathcal{V}$ un espace de Hilbert. Pour tout $\varepsilon \geq 0$, on considère une forme bilinéaire $a_\epsilon(\cdot,\cdot)$ et une forme linéaire $l_\epsilon(\cdot)$ tel qu'il existe trois réels strictement positifs ξ, ζ et α, indépendants de ε tel que pour tout $\varepsilon \geq 0$, on a:

$$\begin{aligned}
|a_\varepsilon(u,v)| &\leq \xi \|u\| \|v\|, \quad \forall\, u, v \in \mathcal{V},\\
|l_\varepsilon(v)| &\leq \zeta \|v\|, \quad \forall\, v \in \mathcal{V},\\
a_\varepsilon(u,u) &\geq \alpha \|u\|^2, \quad \forall\, u \in \mathcal{V}.
\end{aligned}$$

Soit u_ε la solution du problème suivant:

$$\begin{cases} \text{Trouver } u_\varepsilon \in \mathcal{V} \text{ tel que :} \\ a_\varepsilon(u_\varepsilon, w) = l_\varepsilon(w) \ \forall\, w \in \mathcal{V}. \end{cases} \tag{1.12}$$

L'existence et l'unicité de la solution du problème (1.12) sont assurées par le théorème de Lax-Milgram [KLV09].

On considère maintenant une famille de fonctions $J_\varepsilon(\cdot)$ définies sur $\mathcal{V}$ telle que J_0 est différentiable sur $\mathcal{V}$. Dans la suite on considère la notation suivante $j(\varepsilon) = J_\varepsilon(u_\varepsilon)$.

Hypothèses: On suppose qu'il existe une forme bilinéaire δ_a continue sur $\mathcal{V}$, δ_l une forme linéaire continue et une fonction δ_J, ainsi qu'une fonction $f : \mathbb{R}_+ \longrightarrow \mathbb{R}_+$ telles que:

- $\lim_{\varepsilon \longrightarrow 0} f(\varepsilon) = 0,$
- $\|a_\varepsilon - a_0 - f(\varepsilon)\delta_a\|_{L_2(\mathcal{V})} = o(f(\varepsilon)),$
- $\|l_\varepsilon - l_0 - f(\varepsilon)\delta_l\|_{L(\mathcal{V})} = o(f(\varepsilon)),$
- $J_\varepsilon(v) - J_0(u) = DJ_0(u)(v-u) + f(\varepsilon)\ \delta_J(u) + o(\|v-u)\| + f(\varepsilon)),$

où $L_2(\mathcal{V})$ *et* $L(\mathcal{V})$ désignent respectivement les espaces des formes bilinéaires et linéaires continues sur $\mathcal{V}$.

Theorem 1 *La fonction coût $j(\cdot)$ admet un développement asymptotique donné sous la forme suivante:*

$$J_\varepsilon(u_\varepsilon) - j_0(u_0) = f(\varepsilon)(\delta_j + \delta_a - \delta_l) + o(f(\varepsilon)).$$

Preuve 1 *Voir le chapitre 4 du [Ams03].*

1.5.3 Contours et structures fines

La détection des contours a être formalisée pour la première fois en 1980 par un neuroscientifique anglais qui s'appelle David Marr (1945-1980)[MH80]. À partir de l'année 1980, cette tache prend de l'importance pour le traitement d'images dans des domaines aussi variés (médical, télévision, imagerie satellite, multimédia, musée, etc). En effet, une partie très importante de l'image et sur laquelle se base tous les types de traitements est les contours. En traitement d'images et en vision par ordinateur, on appelle détection de contours un procédé permettant de repérer les points d'une image qui correspondent à un changement brutal de l'intensité lumineuse. En effet, ces ensembles représentent des courbes qui séparent des parties homogènes qui décrivent l'image et les objets y sont contenus. De plus, on peut définir les contours comme étant les lignes qui définissent les limites d'un objet dans une image. Ils peuvent être nets ou flous, réguliers ou irréguliers, et peuvent avoir différentes épaisseurs. Les contours sont importants car ils permettent de définir les formes des objets et de les distinguer les uns des autres.

Il existe de nombreuses approches pour la détection de contours. En fait, les méthodes les plus connues sont basées sur les dérivées telles que le gradient, opérateurs de Sobel [GM13], critère de Canny [DG01], Opérateurs de Robinson [EL06].

En outre, on peut définir les structures fines comme des détails à l'échelle microscopique qui composent les objets. Ces détails peuvent inclure des motifs, des textures, des veines, des nervures, des cristaux, etc. Les structures fines peuvent fournir des informations sur la composition et la formation des objets. Autrement dit, on appelle structure fine, tous objet qui a une largeur qui ne dépasse pas quelques pixels et de dimension 0 ou 1 c'est-à-dire **des points** ou **des filaments**. Généralement les méthodes basées sur les dérivées du premier ordre telles que le gradient sont inadéquats pour détecter ce type de structures. Il existe alors de nombreuses méthodes pour se remédier, les plus connues sont basées sur les dérivées d'ordre supérieur. En effet, ils correspondent aux passages par zéro d'un opérateur d'ordre deux tel que le Laplacien et l'hessien [AD14].

Dans l'art, les contours et les structures fines sont des éléments importants pour créer des œuvres expressives et réalistes. Les artistes utilisent souvent des techniques telles que le dessin, la gravure et la peinture pour capturer les contours et les structures fines des objets. Les techniques de rendu 3D, telles que la modélisation par ordinateur, permettent également de reproduire des contours et des structures fines de manière réaliste.

Pour conclure, les contours et les structures fines sont également importants dans les domaines de la reconnaissance de formes et de l'analyse d'images. Les algorithmes de traitement d'images peuvent être utilisés pour détecter les contours et les structures fines dans des images, ce qui peut être utilisé pour la reconnaissance de formes, la segmentation d'images et l'analyse de textures. On présente quelques différences entre les contours et les structures fines dans le Tableau 1.1 et la Figure 1.5:

	Contour	**Structure fine**
1	Objet de dimension supérieure à 1	Objet de dimension 0 ou 1
2	Profil sous la forme de la fonction Delta (voir Figure 1.5)	Profil sous la forme de la fonction Heaviside (voir Figure 1.5)
3	La taille dépend de la résolution de l'image	La taille ne dépend pas de la résolution de l'image

Tab. 1.1 Différences entre contour et structure fine.

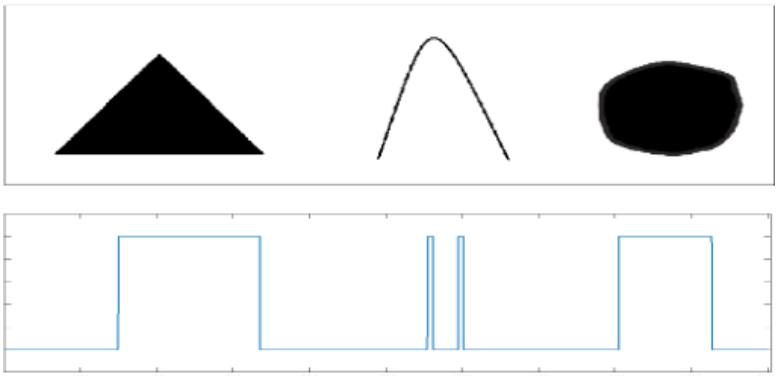

Fig. 1.5 Représentation de la variation des niveaux de luminosité le long d'une ligne d'une image binaire contenant différents objets.

1.6 Recalage d'images

Le recalage d'images est un domaine de recherche en traitement d'images qui vise à aligner deux ou plusieurs images de manière à améliorer la qualité de l'image ou pour effectuer une analyse comparative. Il est utilisé dans de nombreux domaines tels que la médecine, la robotique, la cartographie, la reconnaissance de formes et la télédétection. Le recalage d'images est souvent nécessaire lorsque les images ont été acquises à des moments différents ou avec des paramètres différents, ou lorsque les images sont de différentes modalités. Il existe différentes méthodes de recalage d'images, chacune ayant ses propres avantages et inconvénients. Les méthodes de recalage d'images les plus couramment utilisées sont les méthodes basées sur les caractéristiques, les méthodes basées sur les contours et les méthodes basées sur les points d'intérêts. Les méthodes basées sur les caractéristiques utilisent des caractéristiques spécifiques de l'image, telles que les histogrammes et les textures, pour aligner les images. Les méthodes basées sur les contours utilisent les contours des objets pour aligner les images, tandis que les méthodes basées sur les points d'intérêts utilisent des points spécifiques de l'image pour aligner les images. Il y a des méthodes de recalage d'images telles que la déformation difféomorphique qui sont des méthodes non-rigides. Elles permettent de conserver la forme et les propriétés topologiques de l'image originale en utilisant des transformations mathématiques continues, dérivables et bijectives. Ces méthodes ont été largement utilisées dans le domaine médical pour améliorer la qualité de l'image ou pour comparer des images de différentes études.

Les outils de recalage d'images sont devenus d'un grand intérêt et affectent plusieurs domaines applicatifs comme l'imagerie de surveillance, la robotique, la cartographie, la reconnaissance de formes et surtout l'imagerie médicale. Le recalage peut être utilisé principalement pour la fusion de données provenant de différentes sources

[Mäk+03]. Dans certains cas, différentes sources apportent des informations supplémentaires. Pour cette raison, il faut les fusionner pour ne pas exclure aucune information. L'utilisation de ces informations provenant de différentes sources exige que les données soient ramenées géométriquement aligné et c'est le rôle du recalage d'images.
Dans le but de bien expliquer et montrer le rôle et l'importance de fusion d'images, un exemple illustratif affiché dans la Figure 1.6. En fait, la figure montre des images préopératoires qui illustrent des données sur le patient sur lequel l'intervention doit être pratiquée, provenant de diverses sources: la première image est issue de la tomographie d'émission mono-photonique (TEMP), la deuxième est acquise par imagerie par résonance magnétique (IRM) et la troisième prise par magnéto-encéphalographie (MEG). Pour repérer dans ces images les informations utiles et les présenter au neurochirurgien de la façon la plus ergonomique possible, l'informatique intervient en service à mettre en correspondance les images obtenues.

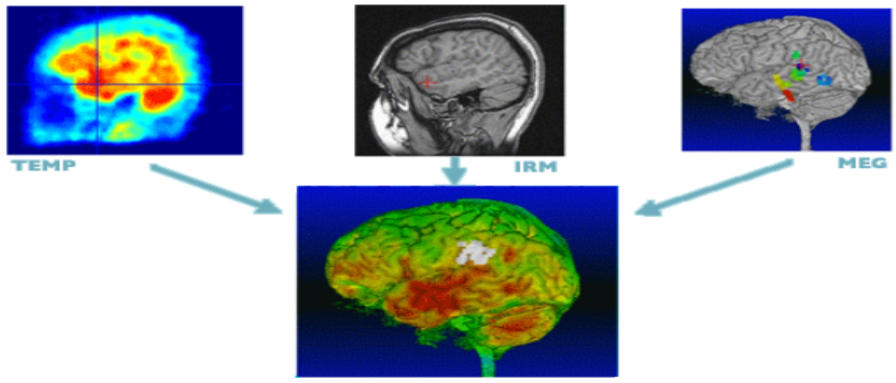

Fig. 1.6 Représentation d'un exemple de recalage et fusion d'images: On obtient une image multimodale à partir d'images issues de diverses sources. https://interstices.info/fusion-d'images-des-outils-au-service-des-neurochirurgiens/

Dans cette section, on va parler brièvement et d'une façon générale du recalage d'images, c'est ce qu'on appelle en anglais 'image registration'. Dans le chapitre suivant, on donne une explication plus détaillée concernant ce problème.
Le recalage d'images est l'un des problèmes très courant en imagerie médicale. En effet, durant les étapes d'enregistrement, de reconstruction et de transmission de l'image, une déformation géométrique est possible. Pour cette raison, on utilise le recalage d'images qui consiste à construire une correspondance géométrique entre deux (ou plusieurs) images d'un même objet prises a des moments différents et/ou à l'aide de dispositifs différents afin de localiser et analyser l'information issue des différents sources (scanner, IRM, rayons X ...). La première image qu'on la note par R est dite image de référence et à laquelle sera comparée à une deuxième image T appelée image source. L'objectif est d'aligner l'image source avec l'image de référence en appliquant une transformation spatiale à l'image d'entrée T.

Mathématiquement, le recalage d'images peut être écrit comme un problème inverse tel que le but est trouver une déformation qu'on la note par φ et cela revient à résoudre l'équation suivante:

$$G_1\left(T\left[\varphi(\mathbf{x})\right]\right) = G_2\left(R(\mathbf{x})\right), \tag{1.13}$$

où G_i sont deux fonctions qui dépendent des deux modalités des images T et R. Généralement, il y a deux types de recalage d'images:

- Recalage paramétrique: φ est une transformation géométrique paramétrique: translation, rotation, homothétie, etc.

- Recalage non paramétrique: φ est une transformation géométrique non paramétrique telle que $\varphi(x) = x + \mathbf{u}(x)$, avec $\mathbf{u}$ représente le champ de déplacement qui appartient à un espace de Banach $\mathcal{W}(\Omega, \mathbb{R}^d)$ à préciser.

Dans cette thèse, on s'intéresse au problème du recalage non paramétrique qui peut être modélisé par:

$$\begin{cases} \text{Trouver } \mathbf{u} \in \mathcal{W}(\Omega, \mathbb{R}^d) \text{ tel que } : \\ G_1(T(\mathbf{x} + \mathbf{u}(\mathbf{x}))) = G_2(R(\mathbf{x})) \ \ \forall \mathbf{x} \in \Omega. \end{cases} \tag{1.14}$$

Le problème (1.14) est typiquement un problème inverse non linéaire et mal posé au sens d'Hadamard. Le principe général pour la résolution de ce type de problème est l'ajout d'un terme de régularisation à l'équation d'attache aux données. D'où les approches variationnelles en recalage d'images consistent à résoudre un problème d'optimisation bien posé qui s'écrit généralement sous la forme suivante;

$$\min_{\mathbf{u} \in (\mathcal{W}(\Omega, \mathbb{R}^d))} \left\{ D\left[G_1(T(\mathbf{x} + \mathbf{u}(\mathbf{x}))), G_2(R(\mathbf{x}))\right] + \lambda J(\mathbf{u}) \right\}, \tag{1.15}$$

où:

- $\mathcal{W}(\Omega, \mathbb{R}^d)$ un espace bien choisi de Ω à $\mathbb{R}^d$,

- $D\left[G_1(T(\mathbf{x} + \mathbf{u}(\mathbf{x}))), G_2(R(\mathbf{x}))\right]$ est un terme de similarité qui mesure l'approximité entre $G_1(T(\mathbf{x} + \mathbf{u}(\mathbf{x})))$ et $G_2(R(\mathbf{x}))$,

- $J(\mathbf{u})$ est un terme de régularisation basé sur des informations a priori sur le niveau de régularité de $\mathbf{u}$.

Déformation difféomorphique

La déformation difféomorphique est une technique utilisée pour recaler des images. Elle consiste à définir une transformation mathématique permettant de déplacer les pixels d'une image de manière à la faire correspondre à une autre image. Cette transformation est appelée déformation difféomorphique car elle conserve la forme et les propriétés topologiques de l'image originale. Par contre, les approches variationnelles en recalage d'images consistent à minimiser une énergie qui est non convexe. Par conséquent, l'unicité de la solution n'est pas garantie. Généralement, une solution qui préserve la topologie des objets est privilégiée, i.e., des déformations difféomorphiques.

Les algorithmes de déformation difféomorphique utilisent généralement des méthodes d'optimisation pour trouver la meilleure transformation pour recaler les images. Ces méthodes d'optimisation peuvent utiliser des contraintes qui garantissent que la transformation est difféomorphique. Cela se traduit par le contrôle du déterminant du jacobien de la déformation pour garantir sa positivité. Plus précisément, la déformation $\varphi(\mathbf{x}) = (\varphi_1(\mathbf{x}), \varphi_2(\mathbf{x}))$ préserve la topologie si on a:

$$\det J_\varphi(\mathbf{x}) = \begin{vmatrix} \frac{\partial \varphi_1}{\partial x}(x,y) & \frac{\partial \varphi_1}{\partial y}(x,y) \\ \frac{\partial \varphi_2}{\partial x}(x,y) & \frac{\partial \varphi_2}{\partial y}(x,y) \end{vmatrix} > 0. \tag{1.16}$$

La déformation difféomorphique est souvent utilisée pour recaler des images médicales, telles que des IRM ou des images de tomographie, pour améliorer la qualité de l'image ou pour comparer des images de différentes études. Le recalage des images est utile pour aligner les images pour une analyse de suivi, pour la comparaison de différents éléments anatomiques.

1.7 Contributions

De nos jours, le recalage d'images joue un rôle très important dans différents domaines et en particulier en imageries médicales afin d'analyser et d'interpréter les images médicales. En effet, plusieurs recherches scientifiques ont été publiées pour ce domaine jusqu'à nos jours et cela due à l'intérêt croissant qui a été porté. Ce type de traitements d'images pourrait se résumer par la recherche d'une déformation pour une image afin qu'elle soit alignée le plus possible à une autre image, avec ces deux images ont les mêmes objets. Dans ce but, de nombreux auteurs ont attaqués à cette difficile tâche en posant un certain nombre de questions: comment déformer

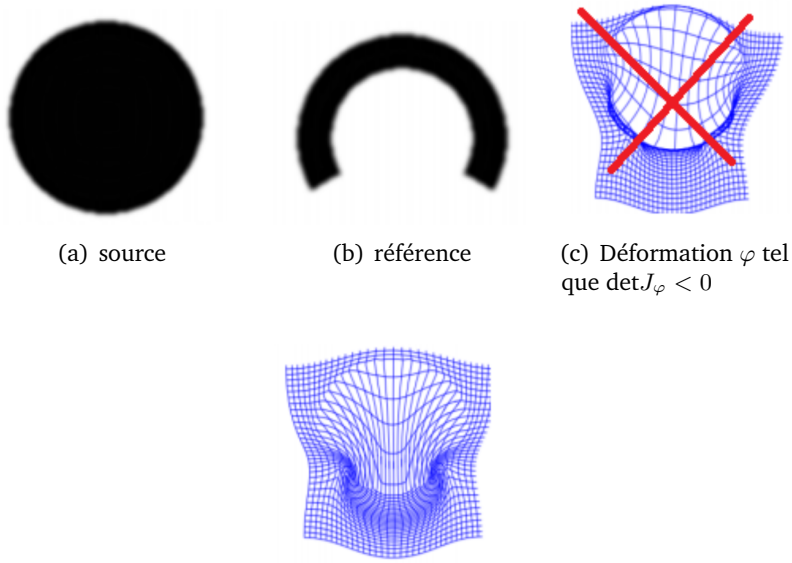

(a) source (b) référence (c) Déformation φ tel que $\det J_\varphi < 0$

(d) Déformation φ tel que $\det J_\varphi > 0$

Fig. 1.7 Recalage d'un disque à une lettre par une déformation difféomorphique et une autre qui n'est pas difféomorphique.

une image? Comment modéliser l'alignement de deux images? Comment trouver la bonne déformation? Comment définir la relation entre deux ou plusieurs images et quelles informations devraient être utilisées pour guider le recalage? Ces différentes questions mènent aux différentes indications pour aligner les images:

- Le modèle de déformation: les modèles linéaires qui modélisent les déformations rigides et affines, et les modèles non linéaires qui peut adapter à n'importe quelles déformations.
- Le caractère de similarité: consiste à définir une certaine distance entre les deux images. Cette distance doit être minimisée (ou maximisée selon le cas) afin que l'alignement entre les objets de deux images est la plus forte.
- L'optimisation: on peut distinguer quatre méthodes d'optimisation numériques: Résolution explicite, méthodes non déterministes, méthodes d'ordre zéro et méthodes d'ordre supérieur.
- Les caractéristiques et les attribus: l'utilisation de ces informations pour guider le recalage est critique. Ce qui entraîne la distinction de trois méthodes de recalage: les méthodes iconiques qui utilisent les valeurs des pixels en comparent directement les intensités. Les méthodes géométriques qui consistent à extraire les informations géométriques (contours, surfaces, etc.) de deux

images et à les aligner. Finalement, les méthodes hybrides qui consistent à combiner ces deux différentes méthodes.

Cette thèse se concentre sur l'analyse théorique, les méthodes numériques et les applications du recalage d'images en se basant sur des informations géométriques. En effet, l'un des principaux objectifs de ce travail est l'analyse théorique et numérique du terme de similarité dans les méthodes de recalage d'images. On aborde trois aspects principaux: la transférabilité des résultats et des techniques de détection d'informations géométriques par des opérateurs d'ordre élevé ou par le calcul variationnel dans le domaine du recalage d'images, l'analyse théorique de la détection des caractéristiques importantes via la méthode du gradient topologique, et l'intégration de l'énergie de Blake-Zisserman dans le domaine de recalage d'images en utilisant l'apprentissage profond pour créer des réseaux de neurones qui permettent la prédiction de la détection des informations géométriques et de la déformation nécessaire pour le processus de recalage. On montre également que les modèles proposés garantissent l'existence d'une solution. On présente des résultats numériques pour illustrer l'efficacité et l'efficience des modèles proposés. En somme, cette thèse fournit une vue d'ensemble des développements récents dans le domaine du recalage d'images basé sur des informations géométriques.

1.8 Structure de la thèse

Chapitre 2
Ce chapitre fournit une introduction générale au recalage d'images. Il donne un aperçu général des techniques mathématiques utilisées pour le recalage d'images, incluant à la fois les méthodes traditionnelles et modernes. On discute les concepts de base du recalage d'images, puis les différents types de transformations couramment utilisées pour aligner les images. De plus, on abordera les défis et les limites du recalage d'images et comment les surmonter en pratique. Finalement, on présente quelques algorithmes d'optimisation utilisés pour trouver les paramètres optimaux de la transformation.

Chapitre 3: Basé sur l'article présenté dans [Laj+22b].
Dans ce chapitre, on s'intéresse aux modèles de recalage pour les images multimodales. On introduit un nouveau terme de similarité pour le recalage d'images qui est basé sur les informations géométriques (contours et structures fines) extraites à partir des images en utilisant l'énergie de Blake-Zisserman. Cette dernière est particulièrement adaptée pour détecter les discontinuités à différentes échelles, c'est-à-dire du premier et du deuxième ordre. On commence par donner une analyse théorique

du modèle proposé. Ensuite, on utilise la méthode de Gauss-Newton et la technique multi-niveau ('multilevel') pour éviter de tomber dans des minimums locaux et pour accélérer les calculs numériques pour la résolution de ce modèle. Enfin, on présente les résultats numériques de la nouvelle approche et on les compare à ceux obtenus par des méthodes existantes. Les expériences numériques illustrent l'efficacité et l'efficience du modèle proposé.

Chapitre 4
Dans ce chapitre, on propose une approche efficace de recalage d'images multi-niveaux basée sur l'apprentissage profond non supervisé, en exploitant les informations géométriques extraites à l'aide de l'énergie de Blake-Zisserman. Cette énergie permet de détecter les informations géométriques des deux images lors de l'entraînement. On propose de construire un réseau de neurones qui prédit les informations géométriques d'une image. Ce réseau est guidé par l'énergie de Blake-Zisserman, ce qui nous permet d'obtenir une détection des informations géométriques dans le cas non supervisé. Ensuite, on utilise ces informations géométriques pour définir un deuxième réseau dédié au processus de recalage d'images. Afin d'obtenir un recalage plus précis et efficace, on propose une nouvelle architecture du réseau de neurones profond qui réalise un recalage multiniveaux. Les résultats numériques illustrés confirment l'efficacité et l'efficience du modèle proposé. De plus, on compare la méthode proposée avec celle présentée dans le chapitre 3, et on utilise des erreurs relatives pour évaluer les résultats obtenus par les deux modèles.

Chapitre 5: Basé sur l'article présenté dans [Laj+22a].
Dans ce chapitre, on propose un nouveau modèle variationnel pour le recalage d'images à partir des données tomographiques. Tout d'abord, on utilise l'approche du gradient topologique pour une reconstruction tomographique qui utilise les discontinuités du premier et du deuxième ordre afin de détecter les objets importants dans les données tomographiques (sinogrammes). Pour cela, on a utilisé des ellipses comme cavités plutôt que des fissures pour calculer le gradient topologique pour le problème de Laplace à partir des données tomographiques. On montre les avantages de cette approche. Ensuite, on utilise ces informations géométriques fournies par un opérateur d'ordre élevé pour définir une mesure de fidélité appropriée pour le processus du recalage d'images. Une étude théorique du modèle proposé est fournie, la méthode de Gauss-Newton et la technique multiniveau sont utilisées pour sa mise en œuvre numérique. Les expériences numériques effectuées montrent l'efficacité et l'efficience de notre modèle.

1.9 Publications liées à la thèse

1. Lajili, Mohamed, et al. "Multimodal image registration based on geometric similarity term", African Conference on Research in Computer Science and Applied Mathematics - CARI'22. 2022. https://hal.science/hal-03703711/

2. Lajili, Mohamed, et al. "Edge sketches for multi-modal image registration based on Blake–Zisserman type energy", Comp. Appl. Math. 41, 315 (2022). https://doi.org/10.1007/s40314-022-02020-z

3. Lajili, Mohamed, et al. "Edge detection from X-ray tomographic data for geometric image registration", Math. Meth. Appl. Sci., 1-35 (2022). https://doi.org/10.1002/mma.8905

4. Lajili , Belhachmi, Moakher, and Theljani. "Unsupervised deep learning for geometric feature detection and multilevel multi-modal image registration", International Journal of Computer Vision. Submitted.

Image Registration

2

Image registration is a fundamental problem in computer vision, with numerous applications ranging from medical imaging to autonomous robotics. Its main objective is to align two or more images of the same scene or object, so that corresponding points in the images are spatially matched. From a mathematical perspective, image registration consists in solving an optimization problem that seeks to minimize the discrepancy or the deformation between the images to be registered. This chapter provides a general introduction to image registration, offering an overview of the mathematical techniques used in both traditional and modern methods. This chapter begins by discussing the basic concepts of image registration, followed by an overview of some different types of transformations commonly used to align images. Moreover, in this chapter we will address some challenges and limitations of image registration and practical solutions to these issues. Finally, this chapter will provide an overview of the optimization algorithms that are used to find the optimal transformation parameters.

2.1 Basic concepts in image registration

Image registration is a well-known concept and it is a challenging image processing task that has applications in various fields like life sciences [Sch+15], astronomy [BCS20], optics [Qua+20], biology [AB20], chemistry [Zha+21], as well as, remote sensing [Gos05] in which researchers generate a global picture from different partial views. We can also also mention security [AD04] which compares current images with those in a data base, and robotics [Liu+19] which uses image registration for the tracking of objects. In addition, image registration is a crucial inverse problem in the domain of medical imaging, which has been extensively studied and summarized in [Hil+01; LA99; MV98].

A geometric deformation can occur during the steps of recording, reconstruction, and transmission of images of the same object. Therefore, it is necessary to geometrically align the images for better interpretation, especially in clinical diagnosis using medical images. The task of image registration consists in determining a geometrical transformation that aligns points of an object in a given image with the corresponding points of that object in another image. The two images could be different because

they were taken with the same imaging device but at different times, this is the case in the example displayed in Fig. 2.1, or were acquired using different imaging modalities or different devices like scanner, positron emission tomography (PET), magnetic resonance imaging (MRI), computer tomography (CT), T1-weighted MR, T2-weighted MR, etc. This is the case in the example displayed in Fig. 2.2. Hence, to apply image registration, the following two main aspects must be defined. First, an important aspect of image registration is to define a measure that quantifies the dissimilarity/distance between each point in the given image and the corresponding point in another image (measuring the disparity between the images). This measure allows to determine the geometrical transformation. Second, another crucial aspect of image registration is to define a regularization that renders the problem well-posed and controls the smoothness of the estimated transformation by penalizing unlikely transformations. The optimal transformation is the one that makes the deformed image as similar as possible to the other image, which remains fixed. Once these two aspects are defined, the image registration problem will be treated as an optimization problem, aiming to find the optimal geometrical transformation. Until now, in order to numerically solve this problem, various optimization methods have been proposed in the literature, such as gradient descent [Rud16], nonlinear conjugate gradient [Dai03], augmented Lagrangian method [TC19], Gauss-Newton [BF95] and quasi-Newton [DM77]. For further details on image registration, interested readers are referred to [Gig+11; Mod09; SDP13; TC19].

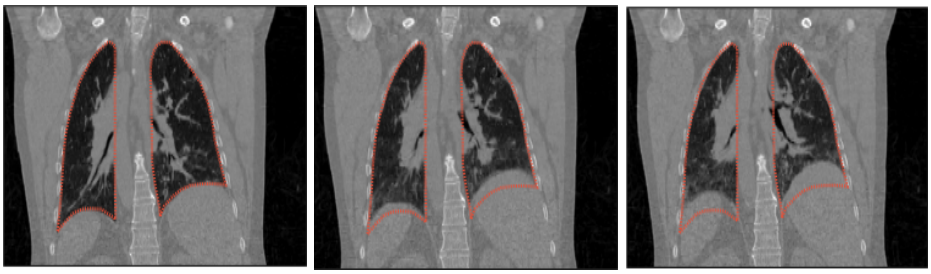

(a) (b) (c)

Fig. 2.1 The figure displays examples of CT scans of the thorax of the same patient taken at three different times. It is evident from the images that there is a geometric deformation between the three scans. The lack of spatial correspondence between the images can be attributed to the respiratory motion in this particular case. https://www.semanticscholar.org/paper/Advanced-Medical-Image-Registration-Methods-for-and-Guyader/0a6ec6cdfed3748f90c0c7e2b775b89c411f1c8d

The concept of image registration can be demonstrated by considering a pair of images: a fixed image called the reference and denoted R, and a moving image called the template and denoted T. The aim of image registration is to find a geometric

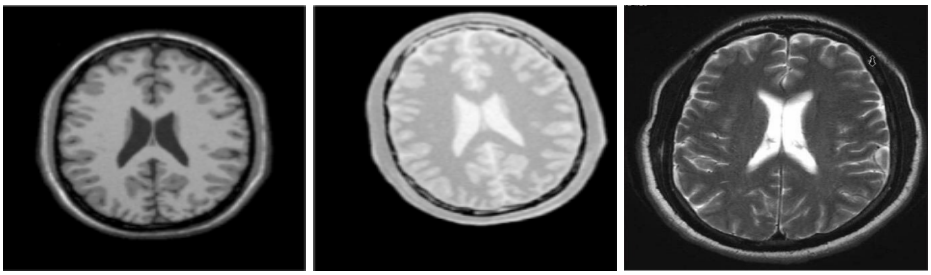

(a) T1 MR brain image (b) PD MR brain image (c) T2-weighted axial MRI of the brain

Fig. 2.2 Images of the brain acquired from the same subject using different imaging modalities are shown in the figure. The images display a geometric deformation as well as a difference in pixel intensity between the three images. The lack of spatial correspondence between the images is due to differences in brain morphology and subject posture during acquisition. https://www.mdpi.com/2072-4292/9/11/1174

transformation that maps T to R. In practice, the objective is to approximately align the image T with the reference R by finding a reasonable deformation, in a way that the distance between R and a deformed version of T (registered image) is as small as possible. This is illustrated in Fig. 2.3. Unfortunately, each application area such as real-time applications in industrial inspection or tracking, remote sensing, high-resolution 3D images, medical treatment planning, etc, has developed its own approaches and implementations, leading to a lack of a generalized theory for image registration.

There are two main ways to characterize an image registration method:

- The first one involves determining the type of deformation between the images, i.e., whether a registration method is parametric or non-parametric. We will give further details on this latter on.

- The second way involves determining whether the registration method is intensity-based or features-based. Intensity-based methods use the voxel intensities directly to measure the degree of shared information between the images. In this case, there is no need for feature extraction. Features-based registration approaches are usually based on two distinct steps: segmentation and calculation of an optimal spatial transformation. Segmentation involves extracting the geometric information (geometric primitives) of the two images to be registered. Three types of geometric information can be identified: points [Roh+96], lines or curves [DPB96] and surfaces [SL96]. The choice of the geometric primitive should be guided by a number of properties, such as easy and accurate detection, robustness to noise and changes related to the acquisition. The second step involves calculating an optimal spatial transformation

by minimizing the distance between corresponding features in the two images. To overcome some problems related to the use of primitives or intensity in the registration process of medical images, various authors have introduced a new category of approaches called hybrid approaches. These approaches aim to improve the robustness of the registration algorithm by combining the advantages related to each type of information used. Some examples of hybrid approaches can be found in [Roc+01; JC02; Cac+01].

(a) Reference image (b) Template image (c) deformed version of T

(d) $|T - R|$, i.e., the error before registration (e) $|T - R|$, i.e., the error after registration

Fig. 2.3 Example of image registration of two images from human hands. The geometric transformation between the reference and the template images is unknown. The deformation is recovered by image registration, resulting in image (c).

2.2 Mathematical framework

In this section we set the problem into a mathematical term, the image registration problem can be described as follows: Given a fixed image R, which is called the reference image, and a moving image T, which is called the template image, both images are represented in a proper feature space by scalar functions $R, T : \Omega \subset \mathbb{R}^d \longrightarrow \mathbb{R}$, where d denotes the spatial dimension of the images. The aim of the image registration problem is to align the template image with the reference one by applying a spatial transformation on the template image so that the transformed

image is as similar to the reference one as possible. The ultimate goal of image registration is to find the best transformation $\varphi : \Omega \longrightarrow \Omega$ that minimizes the similarity measure and achieves the best alignment between the two images, i.e.,

$$G_1\left(T\left[\varphi(\mathbf{x})\right]\right) = G_2\left(R(\mathbf{x})\right), \tag{2.1}$$

where G_1, G_2 must be suitably chosen in the multi-modality scenario. Generally, the solution of the image registration problem depends on several factors, including the quality and amount of available image data, and the chosen optimization algorithm. The type of deformation applied to the images also plays an essential role in determining the solution of the problem (2.1). Indeed, there are two types of image registration. The first one is called parametric image registration and the second one is called non-parametric image registration.

2.2.1 Parametric image registration

In this case, the geometric transformation between the images is represented by a fixed set of parameters that define the transformation, such as translation, rotation, scaling, and other types of transformations, see Fig.2.4. Then, we have a linear transformation function which maps any straight line to straight line. For example:

- **Translation**: The transformation is a simple translation, which is written in the form $\varphi(\mathbf{x}) = \mathbf{x} + \mathbf{t}$ where $\mathbf{t} = (t_1, t_2)$. In this case, the problem consists in finding the two parameters t_1 and t_2 such that:

$$G_1\left(T\left[\mathbf{x} + \mathbf{t}\right]\right) = G_2\left(R(\mathbf{x})\right)$$

- **Rotation**: The transformation consists of rotating objects in the image with an angle θ and which is written in the form $\varphi(\mathbf{x}) = \mathbf{Rx}$ where $\mathbf{R} = \begin{pmatrix} \cos\theta & -\sin\theta \\ \sin\theta & \cos\theta \end{pmatrix}$ is a rotation matrix. In this case, the problem reduces to finding the parameter θ such that:

$$G_1\left(T\left[\mathbf{Rx}\right]\right) = G_2\left(R(\mathbf{x})\right)$$

- **Scaling (geometry)** : The transformation makes it possible to reduce or enlarge the image in one or two directions of space (in 2D), and it is written in the form $\varphi(\mathbf{x}) = \mathbf{Ex}$ with $\mathbf{E} = \begin{pmatrix} k_x & 0 \\ 0 & k_y \end{pmatrix}$ is a scaling matrix where k_x (respectively k_y) represents the change of scale according to the rows (respectively

the columns) of the image . In this case, the problem reduces to finding the parameters k_x and k_y such that:

$$G_1\left(T\left[\mathbf{Ex}\right]\right) = G_2\left(R(\mathbf{x})\right)$$

- **Shearing**: The transformation consists in distortion the shape of the object in the image, and it is written in the form $\varphi(\mathbf{x}) = \mathbf{x} + \mathbf{Cx}$ where $\mathbf{C} = \begin{pmatrix} 0 & \alpha \\ \beta & 0 \end{pmatrix}$. In this case, the problem reduces to finding the parameters α and β such that:

$$G_1\left(T\left[\mathbf{x} + \mathbf{Cx}\right]\right) = G_2\left(R(\mathbf{x})\right)$$

- **General linear transformation**: $\varphi(\mathbf{x})$ is a linear combination of the above transformations.

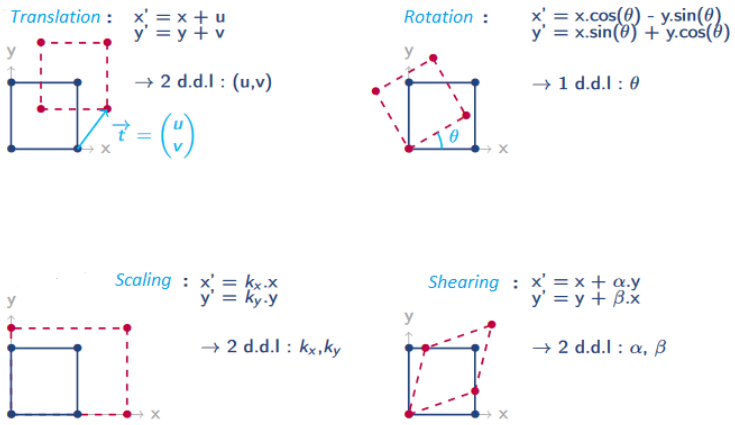

Fig. 2.4 Illustrative example of the parametric image registration problem. The object in the reference image is represented by a blue rectangle, while the deformed object in the template image is represented by broken lines. The geometric transformation between the reference and the template images is expressed using a finite number of parameters.

2.2.2 Non-parametric image registration

In the case of non-parametric image registration [Ver+09], the type of geometric transformation $\varphi(\mathbf{u})$ is unknown a priori. Therefore, the geometric transformation cannot be determined directly. For this reason, we introduce the displacement field

$\mathbf{u} : \mathbb{R}^d \longrightarrow \mathbb{R}^d$ such that $\mathbf{u}(\mathbf{x}) = \boldsymbol{\varphi}(\mathbf{x}) - \mathbf{x}$. This is the case in the example displayed in Fig.2.5. Therefore, the problem can be expressed as follows

$$G_1\left(T\left[\mathbf{x} + \mathbf{u}(\mathbf{x})\right]\right) = G_2\left(R(\mathbf{x})\right). \tag{2.2}$$

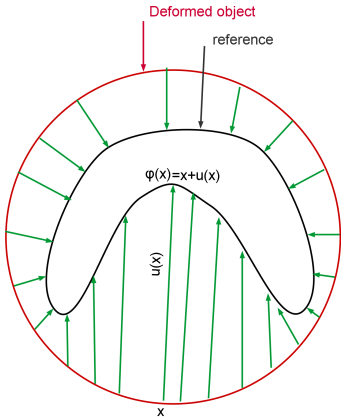

Fig. 2.5 Illustrative example of a displacement field between two 2D objects.

The reconstruction model (2.2) is an equation for the unknown displacement field $\mathbf{u}$, which is assumed to belong to a properly chosen functional space. Mathematically, we can define a warping operator denoted with the same symbol T as for the template image such that, see e.g., Fig.2.6:

$$\begin{aligned} T : \mathcal{W}(\Omega, \mathbb{R}^d) &\longrightarrow Im(\Omega) \\ \mathbf{u} &\longrightarrow T(\mathbf{x} + \mathbf{u}(\mathbf{x})). \end{aligned} \tag{2.3}$$

Then, we can express the problem of image registration in mathematical language as follows:

Proposition 2.2.1 *Given two scalar functions $R, T : \Omega \subset \mathbb{R}^d \longrightarrow \mathbb{R}$ (the reference and the template image, respectively), the non-parametric image registration problem can be modeled by:*

$$\begin{cases} \textit{Find } \boldsymbol{u} \in \mathcal{W}(\Omega, \mathbb{R}^d) \textit{ such that :} \\ G_1\left(T(\boldsymbol{u})\right) = G_2\left(R(\mathbf{x})\right). \end{cases} \tag{2.4}$$

The problem of computing an unknown displacement field $\mathbf{u}$ to obtain a transformed image is typically a nonlinear and an ill-posed inverse problem in the sense of Hadamard. This is because the warping function, T, may not be invertible, which leads to the non-existence and/or non-uniqueness of solutions. Even if T is invertible, its inverse may not be continuous, which makes the solution unstable in the presence of noise in the data, R and T.

In addition, the reference and moving images may be acquired from different devices, which further complicates the problem. To compute the unknown displacement fields and obtain the transformed image, various numerical methods have been developed, such as regularization methods, optimization methods, and deep learning-based methods.

2.2.3 Image registration as an ill-posed problem

This paragraph describes a mathematical formulation that can be used to overcome the ill-posed nature of image registration. The formulation consists in finding a quasi-solution to the problem (2.4) by minimizing or maximizing an energy function that measures the similarity between the images to be registered. Specifically, the energy function is of the form:

$$D\left[G_1\left(T(\mathbf{u})\right), G_2\left(R(\mathbf{x})\right)\right], \tag{2.5}$$

where D is a similarity function that measures similarities between $G_1\left(T(\mathbf{u})\right)$ and $G_2\left(R(\mathbf{x})\right)$ and which depends on the nature of the images to be registered (e.g., mono-modal or multi-modal, to be discussed in the next section). Indeed, the goal is to minimize (or to maximize) this term such that both images R and T become very similar according to some pre-defined metric.

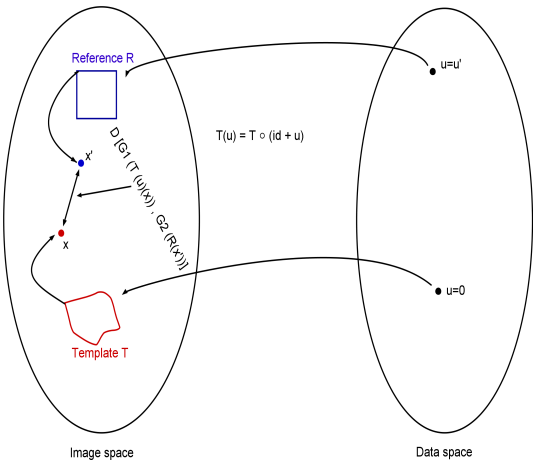

Fig. 2.6 Illustrative example of inverse problem formulation of image registration. **u'** represents the ideal displacement field which aligned the both images R and T, that one wishes to find it or approach it. $T(\mathbf{u})$ represents the warping operator which goes from the data space into the image space.

The reconstruction model (2.5) is an ill-posed inverse problem. Therefore, regularization techniques are necessary to overcome this ill-posedness. Regularization typically turns an ill-posed problem into a well-posed problem. The problem (2.5)

can be reformulated as a minimization problem of an energy known as a variational method, which consists of two parts [PS15; DR04; BMR13; XQ11]. The first part is the fidelity term that measures similarities between the reference image and the template image. The second part is the regularization term [HM04; Vog02], typically denoted as $J(\mathbf{u})$, which encourages smoothness or other desired properties of the displacement field $\mathbf{u}$. The overall energy is minimized with respect to $\mathbf{u} \in \mathcal{W}(\Omega, \mathbb{R}^d)$ and is given by

$$\min_{\mathbf{u}\in(\mathcal{W}(\Omega,\mathbb{R}^d))} \{D\left[G_1(T(\mathbf{x}+\mathbf{u}(\mathbf{x})), G_2(R(\mathbf{x}))\right] + \lambda J(\mathbf{u})\}, \tag{2.6}$$

where $\mathcal{W}(\Omega, \mathbb{R}^d)$ is a properly chosen space of mappings from Ω to $\mathbb{R}^d$, λ is a regularization parameter that balances the trade-off between the fidelity term and the regularization term. Various choices of $J(\mathbf{u})$ are possible, depending on the desired properties of the displacement field.

2.2.4 Regularization term

Non-parametric image registration is a technique used to estimate the transformation between two images without making assumptions about the form of the transformation function. The regularization term plays a crucial role in controlling the smoothness of the estimated displacement field $\mathbf{u}$ and reflecting our prior knowledge by penalizing unlikely transformations, depending only on its derivatives. The regularization term $J : \mathcal{W}(\Omega, \mathbb{R}^d) \longrightarrow \overline{\mathbb{R}}$ is a properly chosen positive regularizer, and λ is a positive regularization parameter. From a mathematical point of view, the regularization term should turn the problem into a well-posed one, i.e., leads to a unique minimizer and, if possible, to a convex objective function.

The choice of the regularization term is a crucial factor in the success of the registration method and the challenge is how to choose the best regularization term which gives the most plausible transformation.

Various regularization terms have been proposed in the literature, such as first-order derivatives based on total variation (see e.g., [Hu+14; PSS13]) and diffusion (see e.g., [FM02a]) and L_2-norm-based regularizers such as elastic and higher-order derivatives based on the curvature.

In Fig. 2.7, the importance and effectiveness of the regularization term are shown. In Fig.2.7(d),(e) and (f), it is clear that the energy (2.5) is unable to minimize the dissimilarity between R and T, such that both images R and deformed version of T are as similar as possible. Then, in Fig.2.7(g),(h) and (i), it is shown that the

variational method (2.6) is efficient in ensuring that the obtained transformation corresponds to a plausible deformation. These results highlight the importance of the regularization term in controlling the characteristics of the deformation, as shown in Fig. 2.7(e) and (h).

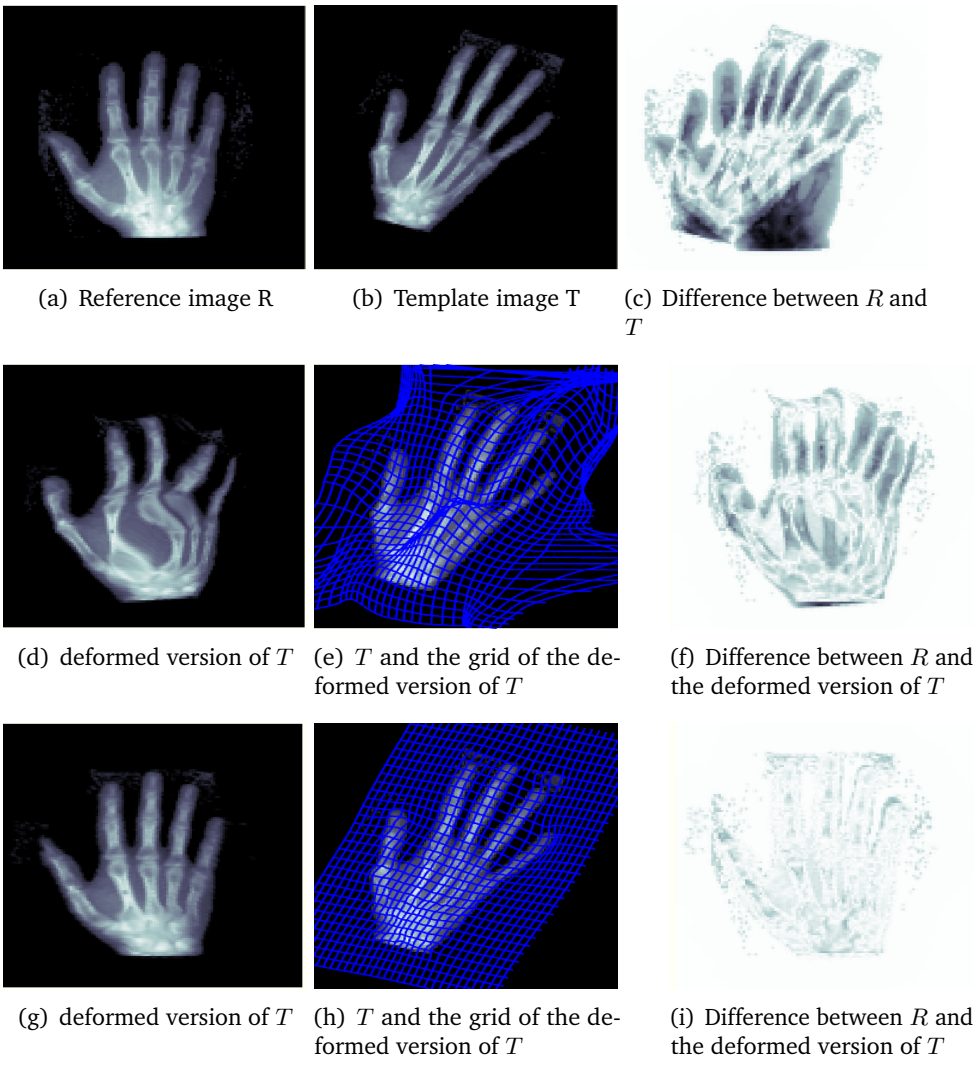

(a) Reference image R (b) Template image T (c) Difference between R and T

(d) deformed version of T (e) T and the grid of the deformed version of T (f) Difference between R and the deformed version of T

(g) deformed version of T (h) T and the grid of the deformed version of T (i) Difference between R and the deformed version of T

Fig. 2.7 Example of image registration results for human hands and illustrates the key role of the regularization term. The minimization problem (2.6) was tested with the fidelity term SSD, the mfElastic regularizer, and either $\lambda = 0$ (corresponding to Fig. (d)-(f)) or $\lambda = 1000$ (corresponding to Fig. (g)-(i)). The resulting deformations were obtained by image registration, and the images in Fig. (d) and (g) demonstrate the effectiveness of the registration method in recovering the deformation.

In conclusion, as the image registration problem (2.1) is an ill-posed inverse one, it can be phrased as an optimization problem in which the aim is to find a reasonable transformation such that the transformed version of a deformed image is aligned to the reference one as much as possible (It may be illustrated in Fig.2.8). In

this context, it is easy to consider the image registration problem as different combinations of choices for the following components:

- A properly chosen functional space $\mathcal{W}(\Omega, \mathbb{R}^d)$.
- The suitable metric on the feature space called by fidelity term (describes the distance/the closeness of the two images)
- The regularization term (to ensure the smoothness of the estimated transformation).

Moreover, the combinations of the above components leads to determining the registration method: mono-modal, multi-modal, elastic, curvature, diffusion, etc.

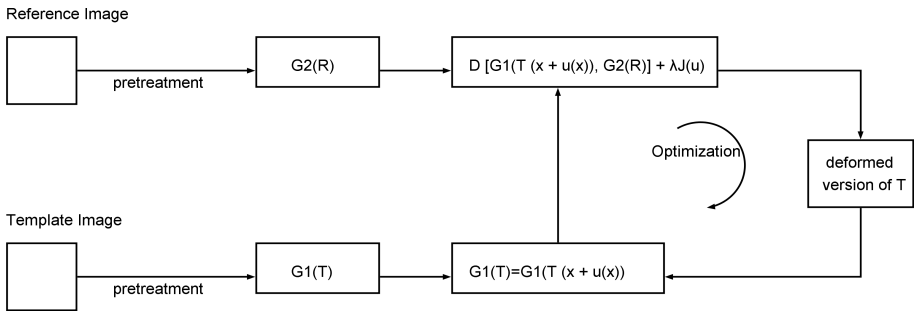

Fig. 2.8 General principle of image registration.

2.2.5 Fidelity term

The fidelity term quantifies the degree of similarity between intensity or between any information for both images. Actually, the choice of a fidelity term depends on the modality of the images to be registered. For monomodal images, i.e., when the images were acquired from the same modality (MRI T1, T2, X-ray laser, etc), both images R and $T(\mathbf{u})$ have the same contrast and similar features; i.e., the gray value of a point is more or less the same in the reference and template images. Then, the preferred fidelity term of the energy (2.6) is often given by:

- *Sum of Squared Differences*(SSD): The $L_2 - norm$ of the difference image is introduced as a prototype of a distance measure. Since this term makes the registration between the pixels, then it is clear that the measure only makes sense if the intensities of the two images are the same. The SSD measure is defined as follows:

Definition 1 *Given two scalar functions $R, T : \Omega \subset \mathbb{R}^d \longrightarrow \mathbb{R}$, the SSD measure is defined by*

$$D^{SSD}(T(\boldsymbol{u}), R) = \frac{1}{2}\|T(\boldsymbol{u}) - R\|_2^2 = \frac{1}{2}\int_\Omega (T(\boldsymbol{u}) - R)^2\, dx. \tag{2.7}$$

- *Correlation coefficient* (CC): It is the optimal measure of similarity for images with a linear relationship between their intensities. The CC measure is defined as follows:

  Definition 2 *Given two scalar functions $R, T : \Omega \subset \mathbb{R}^d \longrightarrow \mathbb{R}$, the CC measure is defined by*

  $$D^{CC}(T(\boldsymbol{u}), R) = \frac{\mathrm{cov}(T(\boldsymbol{u}), R)}{\sigma_{T(\boldsymbol{u})}\sigma_R} \tag{2.8}$$

  where

  $$\mathrm{cov}(T(\boldsymbol{u}), R) = \sum_{x,y}(T(x,y) - \overline{T})(R(x,y) - \overline{R})$$

  $$\sigma^2_{T(\boldsymbol{u})} = \mathrm{var}(T(\boldsymbol{u})) = \frac{1}{n}\sum_{x,y}(T(x,y) - \overline{T})^2 \text{ (the same applies to } \sigma_R)$$

  with

  $$\overline{T} = \frac{1}{n}\sum_{x,y} T(x,y), \text{ is the empirical mean of } T. \text{ (the same applies to } \overline{R}).$$

Since these two terms make the registration between the pixels, then it is clear that such a measure only makes sense for mono-modal images, where the reference and the moving images have similar intensity distributions. In the case of multi-modal images, the reference and the moving images were acquired from different devices. In some case, they most likely have different contrasts and the relation between the intensities of two images is often much more complex. To address this issue, two main approaches have been proposed. The first approach is to use information-theoretic measures and the second approach is to reduce the multi-modal problem to a mono-modal problem by mapping both modalities to a common domain or simulating one modality from another. In this context, various similarity measures have been used, such as the "Mutual Information" (MI) (see e.g., [Mae+97; PMV03; TC19]) and the "Normalized Gradient Field" (NGF) (see e.g., [Hod+14; KR14; Ruh+13; TC19]).

- *Mutual Information (MI):* The mutual information is a popular distance measure for multi-modality image registration, first proposed in 1995 [Col+95a]. Instead of comparing intensities, MI compares the histograms of both images, measuring the mutual information between R and $T(\mathbf{u})$. However, MI has

some limitations. It relies on approximations of the joint density of the gray value distribution, which may not always work well. Additionally, when features with different intensities in the first image have similar intensities in the second image, MI may fail (e.g., in perfusion imaging [Loe+09]). MI is also known to be highly non-convex and has many local maxima, as discussed in section 3 of [HM06]. Figure 2.9 shows an example of a T1 and T2-weighted magnetic resonance image (MRI) of a brain, where MI is highly non-convex. More precisely, the MI between the two images R and $T(\mathbf{u})$ is defined as follows:

Definition 3 *Given two scalar functions $R, T : \Omega \subset \mathbb{R}^d \longrightarrow \mathbb{R}$, the MI measure is defined by*

$$D^{MI}(T(\boldsymbol{u}), R) = -\int_{\mathbb{R}^2} p_{T,R}(t,r) \log \frac{p_{T,R}(t,r)}{p_T(t)p_R(r)} dtdr, \tag{2.9}$$

where $p_{T,R}$ is the joint probability of the gray values, derived from the joint histogram, and p_T and p_R are the probability distributions of the gray values in T and R, respectively.

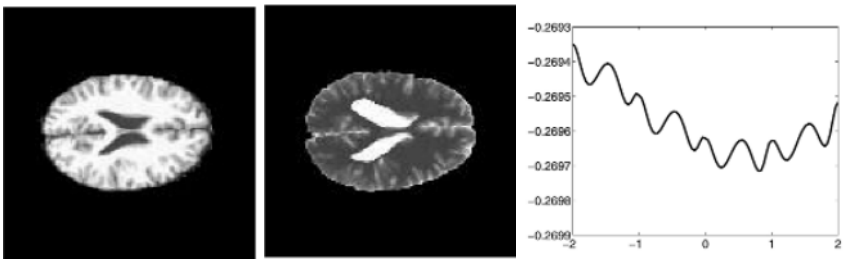

(a) Reference R (b) Template T (c) Mutual information versus shift

Fig. 2.9 An illustrative example of registration of two medical images which shows that mutual information is a highly non-convex function. [HM06]

- *Geometry-based measures:* As an alternative to MI, some approaches have been considered using the first order geometric information in the similarity term in different forms, such as the gradients fields [TC19], the gradient magnitude [PMV00], the normalized gradient fields (NGF) [HM06], and so on. The idea behind gradient-based measures is to minimize the angle between the two gradient vectors, which will result to aligned images.

  Since the NGF distance is based on a derived information from the image intensity, i.e, the gradient, then there are some examples of image registration where the NGF model does not work well. Specifically, this model may fail to detect and register thin structures in images where the gradients are null

or very weak. Moreover, if $\nabla T \perp \nabla R$, then $\nabla T \cdot \nabla R = 0$, which means that $D^{NGF}(T(\mathbf{u}), R) \approx \int_\Omega 1 dx$. As a result this model will fail. An example of such a failure case is given in [TC19], which is shown in Fig.2.10. The NGF measure is defined as follows:

Definition 4 *Given two scalar functions $R, T : \Omega \subset \mathbb{R}^d \longrightarrow \mathbb{R}$, the NGF measure is defined by*

$$D^{NGF}(T(\mathbf{u}), R) = \int_\Omega \left[1 - \left(\frac{\nabla T(\mathbf{u}) \cdot \nabla R}{\sqrt{|\nabla T(\mathbf{u})|^2} \sqrt{|\nabla R|^2}} \right)^2 \right] d\mathbf{x}. \tag{2.10}$$

This measure is based on the cosine distance between the two vectors.
Alternatively to use the images gradients, edges that are detected by minimizing the Mumford-Shah energy (**MS**) were also used to deal with image registration coupled with segmentation as a variational joint-free discontinuity problem [DR06].

(a) Reference R (b) Template T (c) Registered image by using NGF as similarity

Fig. 2.10 Example of registration of two synthetic images where $\nabla_n T \cdot \nabla_n R = 0$ (or one of $\nabla_n T, \nabla_n R$ is zero) a.e. in Ω. NGF similarity term fails completely. [TC19]

2.3 Optimization algorithms for finding the optimal transformation parameters

Image registration is the process of aligning two or more images of the same scene taken from different devices, times or viewpoints. Finding the optimal transformation parameters to align images is one of the main challenges in image registration. There are a wide variety of optimization algorithms that can be used for this purpose, ranging from traditional techniques such as gradient descent to more modern methods such as Gauss Newton algorithm and augmented Lagrangian method. In general, the choice of an optimization algorithm depends on the specific characteristics of

the images being registered, as well as the desired accuracy and computational efficiency of the registration process.

One of the most commonly used optimization algorithms in image registration is the gradient descent method [Laj+22c], which iteratively updates the transformation parameters in the direction of the negative gradient of the function being minimized. This method is also widely used in machine learning to optimize the parameters of a model, and it is a key component of many popular optimization techniques, such as stochastic gradient descent and mini-batch gradient descent.
The basic idea of gradient descent is to start with an initial set of parameters and then repeatedly update them in the direction of the negative gradient of the function to be optimized. This process continues until the parameters converge to a local minimum of the function, or until a stopping criterion is reached. One of the key advantages of gradient descent is its relative simplicity and applicability to a wide range of problems. However, there are also some limitations of the method, such as the possibility of getting stuck in a local minimum or the need for a good initial set of parameters.
Overall, gradient descent is simple to implement and often effective in practice, but it can be slow to converge.

Another popular optimization algorithm for image registration is the Gauss-Newton algorithm, which is an optimization method used to solve non-linear systems of equations. The Gauss-Newton algorithm updates the transformation parameters iteratively using a combination of the negative gradient and the Hessian matrix of the function being optimized. This can provide a more efficient optimization process than gradient descent, particularly for problems with a large number of parameters. The Gauss-Newton method is often used to solve non-linear least squares problems, as it generally converges faster than other optimization methods. However, it can be sensitive to the choice of initial parameters and may get stuck in local minima. Therefore, it is important to choose a reasonable initial parameters and to check the convexity of the function to avoid these problems.
The Gauss-Newton method solves the minimisation problem by approximating the original non-linear system with a linear one. Indeed, to minimize an energy $\mathcal{J}$, the Gauss-Newton algorithm consists of several steps: Starting from an initial guess δU, we compute the gradient $G_{\mathcal{J}}$ at each step. Then we improve this guess by updating δU which is solution of the linear system:

$$\mathcal{H}\delta U = -G_{\mathcal{J}}. \tag{2.11}$$

The process is repeated until convergence, which is achieved when $\|\delta U - \delta U_{old}\| \leq \varepsilon$, where ε is a given threshold. Note that the approximated Hessian $\mathcal{H}$ is symmetric and positive definite.

2.4 Motivation and problem statement

In image processing, there are many applications that are interested in the relationship between two or more images, and tracking changes. Image registration is the process of aligning two or more images of the same object which are obtained at different times or from different devices. Image registration can be considered as a necessary step for various image processing applications, such as image fusion, change detection, and motion analysis, that require the comparison of multiple images.
Image registration consists in finding a mathematical transformation that maps the pixels of one image onto the corresponding pixels of another image. This transformation can be a rigid transformation, an affine transformation, or a non-linear transformation, depending on the degree of deformation between the two images.
The task of image registration is more challenging in the case of multi-modal images, where the intensity variations between the images are not directly comparable. In such cases, image registration algorithms need to incorporate additional information, such as image features, to establish correspondences between the images. Moreover, the images provide a wealth of information, and there are many methods proposed in the literature for extracting this information. However, the main challenge in the image registration process is not only how to choose the best information but also how to align the images accurately.

The accuracy of image registration can be evaluated using a fidelity measure that quantifies the difference between the registered images. Choosing the appropriate fidelity measure is essential, and it depends on the nature of the images being registered. For example, in the case of multi-modal images, the intensities of the same object in different images may not be similar, making it challenging to use intensity-based measures. Therefore, geometric information such as edges, thin structures, gradients, and Hessian can be useful for defining a fidelity measure.
In addition to the fidelity measure, the choice of registration method is also important. Different registration methods, such as feature-based, intensity-based, and hybrid methods, have different strengths and weaknesses depending on the nature of the images being registered.
Overall, image registration is a complex process that requires careful consideration

of the information available in the images, the choice of fidelity measure, and the selection of an appropriate registration method.

There are two kinds of important features in the image: edges and thin structures, and it is generally more challenging to detect thin structures than edges. Every object in $(d-1)$-dimension can be linked to a structure that is assumed to be thin such as filaments in 3D or points in 2D. Generally, the derivation operator of first order detects edges and it is not efficient in detecting thin structures. There are some arguments to explain this:

- Thin structures are different from edges in terms of their intensity profiles. Edges have a Heaviside profile, which means that the intensity abruptly changes from one side of the edge to the other. In contrast, thin structures have a Dirac delta profile, which means that the intensity is concentrated at a single point or along a very narrow line.

- Thin structures are also more challenging to detect in the presence of noise. This is because noise can easily obscure the small and irregular features of a thin structure, making it difficult to distinguish from the background.

Overall, while edges and thin structures are both important features in images, they require different methods for detection and analysis due to their distinct characteristics.

Non-parametric image registration based on first-order derivatives can be a fast and efficient registration method. However, there are some difficulties associated with this method, such as non-clear edges. Indeed, one of the main challenges with using geometry-based measures that rely on gradient information, is that first-order derivatives, such as the gradient, fail to detect second-order discontinuities, such as those found by the Laplacian or Hessian. However, this information may be valuable in some applications, such as clinical diagnosis using medical images, and could provide important information for doctors. Second, gradient detection is also very sensible to noise that is always present in the images. This can result in false edges that mislead the alignment process. Therefore, it is important to use techniques to reduce the effects of noise, such as smoothing or filtering, to improve the accuracy of the registration process. Overall, while non-parametric image registration based on first-order derivatives can be a fast and efficient method, it is important to be aware of its limitations and to use appropriate techniques to overcome them. In this thesis, we addressed this type of problems related to image registration and proposed solutions to overcome them. The first problem is the inability of first-order derivative-based methods to detect second-order discontinuities such as Laplacian/Hessian discontinuities. We propose a new fidelity measure that uses both first- and second-order

discontinuities, inspired by the Blake-Zisserman energy. Experimental tests showed that our proposed measure performs well in multi-modality image registration. In the second problem, we propose to use a convolutional neural network to detect the geometric information and employ them to build a fidelity measure for unsupervised image registration. Indeed, we propose an efficient multilevel image registration approach based on unsupervised deep learning, leveraging the geometric information extracted by using the Blake-Zisserman energy. This energy enables the detection of geometric information from two images during training. This network is guided by the Blake-Zisserman energy, allowing us to achieve unsupervised detection of geometric information. Subsequently, we use this geometric information to define a second network dedicated to the image registration process. To achieve more accurate, precise and efficient image registration, we introduce a new architecture for a deep neural network that performs multilevel image registration. In the third problem, we use the topological gradient approach for a tomographic reconstruction and detection that uses the first- and second-order discontinuities. We show the advantage of that T-G which uses only the first-order discontinuities for the detection of geometric information. A new method for image registration with geometric information detection via the topological gradient method will be presented in the second work. The results obtained for the detection and the registration are very promising.

Overall, our proposed methods showed promising results for both detection and registration tasks.

3 Edge sketches for multi-modal image registration based on Blake-Zisserman type energy

The purpose of this chapter is to introduce a new similarity term for multi-modal image registration which is based on the geometric information (edges and thin structures) extracted from the images using the Blake–Zisserman's energy. It is based on the article [Laj+22b] which is summarized below.

Summary

In this chapter, using geometric information from the images we propose to build a robust and efficient similarity term for a deformable registration model for multi-modality images. Indeed, in most multi-modality image registration models, the intensities of the same object in different images are dissimilar, while the geometric information (edges, gradient, Hessian) is the same. Therefore, this information is useful for defining a fidelity measure. To extract this information, we employ the Blake-Zisserman's energy, which is described in publications such as [ZV13; BZ87; DR06]. This energy is well suited for detecting discontinuities at different scales i.e., of first and second order. This has an advantage, for example when the image contains high-order features, such as thin structures (points, filaments), that are not detectable by first-order derivatives, e.g., see [TB21].

Given two images $R, T : \Omega \subseteq \mathbb{R}^2 \longrightarrow \mathbb{R}$ to be registered, we define R_s and T_s their smoothed versions that are obtained by convolution with a Gaussian kernel. Then, we propose to register the two functions from different image modalities by solving the following minimization problem:

$$\min_{\mathbf{u}\in\mathcal{W}} \left\{ \mathcal{J}(\mathbf{u}) = \frac{1}{2}\|\mathcal{A}_T^{-1}(\beta) - \mathcal{A}_R^{-1}(\beta)\|_2^2 + \frac{\lambda}{2}\int_\Omega |\nabla \mathbf{u}|^2 d\mathbf{x} + \frac{\gamma}{2}\int_\Omega |\nabla^2 \mathbf{u}|^2 d\mathbf{x} \right\}, \quad (3.1)$$

where $\mathcal{A}_T$ and A_R are two operators defined on the space $\mathcal{V} = \left\{ Z \in H^1(\Omega); \frac{\partial Z}{\partial n} = 0 \right\}$ by

$$\begin{cases} \mathcal{A}_T = -4\varepsilon^2\beta\Delta + (4\varepsilon\alpha|\nabla^2 T_s(\mathbf{u})|^2 + 4\varepsilon\xi|\nabla T_s(\mathbf{u})|^2 + \beta), \\ \mathcal{A}_R = -4\varepsilon^2\beta\Delta + (4\varepsilon\alpha|\nabla^2 R_s|^2 + 4\varepsilon\xi|\nabla R_s|^2 + \beta). \end{cases} \tag{3.2}$$

λ and γ are regularization parameters, and

$$\mathcal{W} = (H_0^2(\Omega))^d := \left\{ \mathbf{u} \in (H^2(\Omega))^d \text{ such that } \mathbf{u} = \mathbf{0} \text{ and } \frac{\partial \mathbf{u}}{\partial n} = \mathbf{0} \text{ on } \partial\Omega \right\}.$$

In this chapter, we provide a theoretical analysis of the proposed model by proving the existence of a solution. Additionally, we present the discretization of the model which is based on the discretize-optimize approach. To solve this proposed model numerically, we use the Gauss-Newton algorithm and multilevel technique to accelerate the numerical computations for the solution of this model. Finally, we present numerical results carried out on different images that are obtained using the proposed approach. We also present numerical results which illustrate the benefit of our proposed model, which can solve the problem of weak edges and second-order discontinuities with acceptable registration result. To demonstrate the efficiency of the proposed method, we make a comparison with two existing multi-modality models: the normalized gradient field model (denoted by **NGF** below) and the mutual information (denoted by **MI** below). Furthermore, to evaluate the quality of the registration results given by these three models, we use two error measures: $MI_{\text{err}} = D^{MI}(T(\mathbf{u}), R)$ and $NGF_{\text{err}} = D^{NGF}(T(\mathbf{u}), R)$, as defined in equations (3.6) and (3.7), respectively. In addition to the above two measures, we use the dice score (**DSC**) for images which is defined by

$$\mathbf{DSC}(R, T) = 2\frac{|R \cap T|}{|R| + |T|} = 2\frac{\sum_i R^i T^i}{\sum_i (R^i + T^i)}. \tag{3.3}$$

Computational and Applied Mathematics (2022) 41: 315
https://doi.org/10.1007/s40314-022-02020-z

Received: 18 January 2022 / Revised: 15 July 2022 / Accepted: 27 August 2022 /
Published online: 18 September 2022

Abstract

In this paper, we are interested in deformable registration models for multi-modality images. We introduce a new similarity term for image registration which is based on the geometric information (edges and thin structures) extracted from the images using the Blake-Zisserman's energy. The later is well suited for detecting discontinuities at different scales, i.e., of first and second order. We start by giving a theoretical analysis of the proposed model. Then, we use the Gauss-Newton method and multilevel technique to speed up the numerical computations for the solution of this model. Finally, we present some numerical results of the new approach and we compare them with those obtained by some existing methods. The experiments illustrate the efficiency and effectiveness of the proposed model.

Keywords: Image registration· Inverse problems· Optimization· Variational models· High-order PDEs· Edge map.

MSC Classification: 94A08 · 65K10 · 35R25

3.1 Introduction

Image registration is a challenging image processing task which can be encountered in diverse fields such as astronomy [BCS20], optics [Qua+20], biology [AB20], chemistry [Zha+21], life sciences [Sch+15], remote sensing [Gos05] and medical imaging [Sch06]. It consists in constructing a geometric correspondence between two or more images of the same object which were taken at different times or were acquired using different devices (scanner, IRM, etc), see e.g., [FM02a; Gig+11; Mod09; SDP13; TC19; ZF03]. The image registration problem can be described as follows: Given a fixed image R, which is called the reference image, and a moving

image T, which is called the template image, both images are represented by scalar-valued functions $R, T : \Omega \subset \mathbb{R}^d \longrightarrow \mathbb{R}$, where d denotes the spatial dimension of the images. Then, the aim of the image registration problem is to align the template image with the reference one by applying a spatial transformation on the template image so that the transformed image is as similar to the reference one as possible.

This problem can be formulated mathematically as finding a geometric transformation of the form $\varphi(\mathbf{x}) = \mathbf{x} + \mathbf{u}(\mathbf{x})$, where $\mathbf{u} : \mathbb{R}^d \longrightarrow \mathbb{R}^d$ is a displacement field such that:

$$D\left(G_1\left[T(\varphi(\mathbf{x}))\right], G_2(R(\mathbf{x}))\right) \tag{3.4}$$

is small, where $D(\cdot,\cdot)$ is a chosen similarity measure, G_1 and G_2 are two functions which depend on the two imaging modalities. Generally, there are two types of image registration. The first one is called the parametric image registration in which the type of the geometric transformation $\varphi(\mathbf{x})$ is a simple homogeneous transformation, such as rotation, translation, homothety, etc [CC]. The second one is called non-parametric image registration [Ver+09] in which the type of the geometric transformation $\varphi(\mathbf{u})(\mathbf{x})$ is unknown and one has to determine the unknown displacement field $\mathbf{u}(\mathbf{x})$.

The reconstruction model (3.4) is known to be an ill-posed inverse problem. Therefore, it is necessary to use regularization techniques to overcome this ill-posedness. Generally, the regularization turns an ill-posed problem into a well-posed problem. For this purpose, problem (3.4) is reformulated as a minimization problem of an energy which is composed of two parts, see e.g., [BMR13; XQ11],

$$\min_{\mathbf{u}\in\mathcal{W}(\Omega,\mathbb{R}^d)} \left\{D\left(G_1(T(\mathbf{x}+\mathbf{u}(\mathbf{x})), G_2(R(\mathbf{x}))\right) + \lambda J(\mathbf{u})\right\}, \tag{3.5}$$

where $\mathcal{W}(\Omega,\mathbb{R}^d)$ is a properly chosen functional space. The first part of the energy (3.5) is a fidelity term that measures similarities between $G_1(T(\mathbf{x}+\mathbf{u}(\mathbf{x})))$ and $G_2(R(\mathbf{x}))$ and depends on the nature of images (mono-modality, multi-modality) to be registered. Indeed, the goal is to minimize (or to maximize) this term such that both images R and T become very similar according to some pre-defined metric. The second part of the energy (3.5) is the regularization term [HM04; Vog02] which controls the smoothness of the displacement field $\mathbf{u}$ and reflects our expectations by penalizing unlikely transformations. The challenge is how to choose the best regularization term which gives the most plausible transformation. Various regularizers have been proposed in the literature. For example, first-order derivatives that are based on total variation (see e.g., [Hu+14; PSS13]) and diffusion (see e.g., [FM02a]).

For monomodal images, i.e., when the images were acquired using the same modality (MRI T1, T2, X-ray laser, etc), both images R and $T(\mathbf{u})$ have the same contrast and similar features. Then, the preferred fidelity term of the energy (3.5) is often given by the "Sum of Squared Differences" (SSD) or the "correlation coefficient" (CC) between $T(\mathbf{u})$ and R.

In the case of multi-modality images, the reference and the moving images were acquired from different devices. Therefore, most likely, they have different contrasts and the relation between the intensities of two images is often much more complex. Hence, the mono-modality fidelity terms are not appropriate in this case. Various similarity measures have been used, such as the "Mutual Information" (MI) (see e.g., [Col+95b; Mae+97; PMV03; TC19]) and the "Normalized Gradient Field" (NGF) (see e.g., [Hod+14; KR14; Ruh+13; TC19]).

Mutual Information (MI): The underlying idea of the MI is to measure the mutual information between R and $T(\mathbf{u})$. It consists in comparing the histograms of both images instead of comparing their intensities. More precisely, the MI between two images R and $T(\mathbf{u})$ is defined as follows:

$$D^{MI}(T(\mathbf{u}), R) = -\int_{\mathbb{R}^2} p_{T,R}(t,r) \log \frac{p_{T,R}(t,r)}{p_T(t)p_R(r)} dtdr, \tag{3.6}$$

where $p_{T,R}$ is the joint probability of the gray values which can be derived from the joint histogram and p_T, p_R are the probability distributions of the gray values in T and R, respectively. The main challenge in mutual information is the non-trivial approximation of the joint density of the intensities distribution [HM06]. It has disadvantages when features of the same gray values in one image have different gray values in the second image [Loe+09].

Geometry-based measures: As alternative to MI, some approaches have considered the use of the first-order geometric information in the similarity term in different forms such as the gradients fields [TC19], the gradient magnitude [PMV00], the normalized gradient fields (NGF) [HM06], etc. The idea of the gradient based measures is to minimize the angle between the two gradient vectors that will yield aligned images. For example, The NGF measure is defined as follows:

$$D^{NGF}(T(\mathbf{u}), R) = \int_{\Omega} \left[1 - \left(\frac{\nabla T(\mathbf{u}) \cdot \nabla R}{\sqrt{|\nabla T(\mathbf{u})|^2}\sqrt{|\nabla R|^2}} \right)^2 \right] d\mathbf{x}, \tag{3.7}$$

which is exactly based on the cosine distance between the two vectors. Alternatively to using the images gradients, edges that are detected by the minimizing the Mumford-Shah energy (**MS**) were also used to deal with image registration coupled with segmentation as a variational joint free discontinuity problem [DR06].

In this paper, we consider a new geometry-based similarity measure for multi-modal image registration. Most of geometry-based measures use the gradient information and there are mainly two challenges related to this. First, being a first-order derivatives, the gradient fails in detecting discontinuities of second order, i.e., discontinuities of the Laplacian/Hessian. However, this information may be valuable in some cases and could be a very good indicative information for the alignment the two images. Second, gradient detection is also very sensible to noise that is always present in the images and false edges that are caused by noise mislead the alignment process. To overcome these two problems, we consider a similarity measure that uses the first- and second-order discontinuities to align the images. The computation of these discontinuities is less sensitive to noise since they are based on the regularized Black-Zisserman (**BZ**) energy, see e.g., [ZV13; BZ87; DR06], which is well suited for detecting discontinuities at different scales.

More precisely, for an input image T, the regularized **BZ** energy is defined in the Sobolev space $H^2(\Omega) \times H^1(\Omega)$ by

$$\begin{aligned} BZ_\epsilon(T_s, Z_T) = \tfrac{1}{2}\int_\Omega \lambda_0 (T_s - T)^2 d\mathbf{x} + \alpha \int_\Omega Z_T^2 |\nabla^2 T_s|^2 d\mathbf{x} \\ + \xi \int_\Omega (Z_T^2 + \sigma)|\nabla T_s|^2 d\mathbf{x} + \beta \int_\Omega \left(\epsilon |\nabla Z_T|^2 + \frac{(Z_T - 1)^2}{4\epsilon} \right) d\mathbf{x}. \end{aligned} \tag{3.8}$$

It is clear that when $\alpha = 0$, the above energy corresponds to the well-known Mumford-Shah energy which uses only first-order derivatives of T. This has a disadvantage for example when the image contains high-order features such as thin structures (points, filaments) and are not detectable by first-order derivatives, e.g., see [TB21]. Whereas, by incorporating high-order derivatives, these high-order features could be easily detected by the variable Z_T, e.g., Fig. 3.1. The outline of the paper is as follows. In Section 2, we introduce our new variational model for image registration which is based on the **BZ** energy. In section 3, we first give a theoretical analysis of the proposed model by proving the existence of a solution. Second, we give the discretization of the model which is based on the disctritize-optimize approach. Section 4 is concerned with the presentation of some numerical tests for the proposed approach. Finally, a summary and outlooks are given in Section 5.

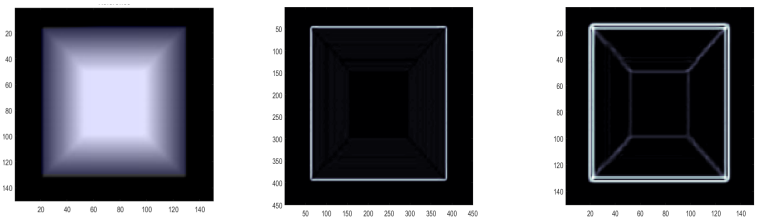

(a) A given image (b) Geometric information detected by the **MS**. (c) Geometric information detected by the **BZ**.

Fig. 3.1 Example of geometric information detected by **MFS** and **BZ**. The Blake-Zisserman's energy detects geometric information which cannot be detected by the Mumford-Shah energy.

3.2 The new multi-modality model

In this section, we introduce a new variational model for image registration based on the energy (3.8). Since our formulation consists of two building blocks: a similarity measure D and a regularization term J, we now discuss our choice of regularizers and the distance measure. Because our emphasis is on the latter, almost all regularizers suitable for variational registration models of mono-modal images may be used.

Similarity measure: Given two images $R, T : \Omega \subseteq \mathbb{R}^2 \longrightarrow \mathbb{R}$ to be registered, we define R_s and T_s their smoothed versions that are obtained by convolution with a Gaussian kernel. Then, we can compute two edge maps Z_T and Z_R by solving the following two optimization problems:

$$\min_{Z_T} \left\{ \alpha \int_\Omega Z_T^2 |\nabla^2 T_s|^2 d\mathbf{x} + \xi \int_\Omega (Z_T^2 + \sigma) |\nabla T_s|^2 d\mathbf{x} + \beta \int_\Omega \epsilon |\nabla Z_T|^2 + \frac{(Z_T - 1)^2}{4\epsilon} d\mathbf{x} \right\},$$

$$\min_{Z_R} \left\{ \alpha \int_\Omega Z_R^2 |\nabla^2 R_s|^2 d\mathbf{x} + \xi \int_\Omega (Z_R^2 + \sigma) |\nabla R_s|^2 d\mathbf{x} + \beta \int_\Omega \epsilon |\nabla Z_R|^2 + \frac{(Z_R - 1)^2}{4\epsilon} d\mathbf{x} \right\}.$$

It is clear that solving the above optimization problems is equivalent to solving the two boundary-value problems

$$\begin{cases} \mathcal{A}_T Z_T = \beta & \text{in } \Omega, \\ \frac{\partial Z_T}{\partial n} = 0 & \text{on } \partial\Omega, \end{cases} \tag{ET}$$

$$\begin{cases} \mathcal{A}_R Z_R = \beta & \text{in } \Omega, \\ \frac{\partial Z_R}{\partial n} = 0 & \text{on } \partial\Omega, \end{cases} \tag{ER}$$

where $\mathcal{A}_T$ and A_R are two operators defined on the space $\mathcal{V} = \left\{ Z \in H^1(\Omega); \frac{\partial Z}{\partial n} = 0 \right\}$ by

$$\begin{cases} \mathcal{A}_T = -4\varepsilon^2\beta\Delta + (4\varepsilon\alpha|\nabla^2 T_s(\mathbf{u})|^2 + 4\varepsilon\xi|\nabla T_s(\mathbf{u})|^2 + \beta), \\ \mathcal{A}_R = -4\varepsilon^2\beta\Delta + (4\varepsilon\alpha|\nabla^2 R_s|^2 + 4\varepsilon\xi|\nabla R_s|^2 + \beta). \end{cases} \tag{3.9}$$

Therefore, the new similarity measure is defined by

$$D^{BZ}(R,T) = \|Z_T - Z_R\|_2^2 = \|\mathcal{A}_T^{-1}(\beta) - \mathcal{A}_R^{-1}(\beta)\|_2^2. \tag{3.10}$$

The maps Z_T and Z_R contain richer information about the discontinuities and the edges of the images T and R than the maps obtained by using **MFS** ($\alpha = 0$). Moreover, compared to the NGF, the maps are less sensitive to noise since they are computed based on the regularized energies as shown in Fig. 3.2.

As expected, we can see in Figs. 3.2 and 3.3 that the measure D^{BZ} can solve the problem of weak edges and second-order discontinuities with acceptable registration compared to **MFS**-based models. *Choice of the regularizer*: For the choice of the

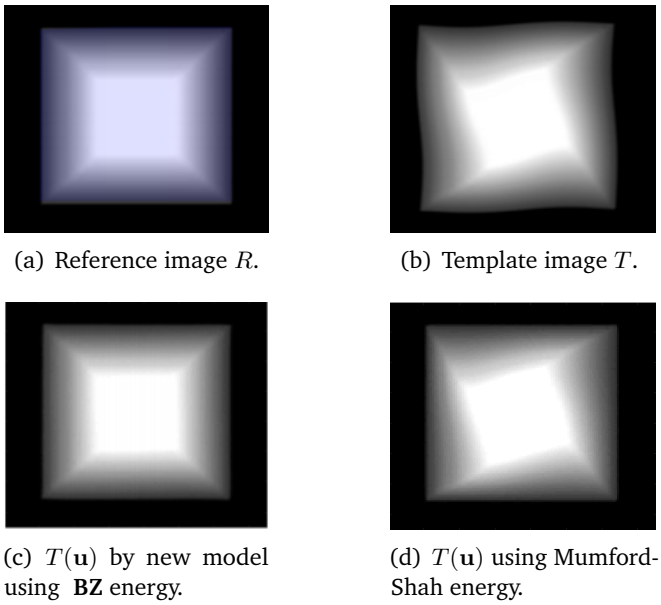

(a) Reference image R.

(b) Template image T.

(c) $T(\mathbf{u})$ by new model using **BZ** energy.

(d) $T(\mathbf{u})$ using Mumford-Shah energy.

Fig. 3.2 Example of registration of two images which are described by a very sensitive geometrical information. Similarity term which is based on the **BZ** energy can solve the problem of weak edges and second-order discontinuities with acceptable registration, **MFS**-based model fails completely.

regularization term, as mentioned in the introduction, there are lots of regularizers and hence the choice of a good one becomes delicate. Here we choose a robust regularizer that allows large and smooth deformation, which is comprised of the

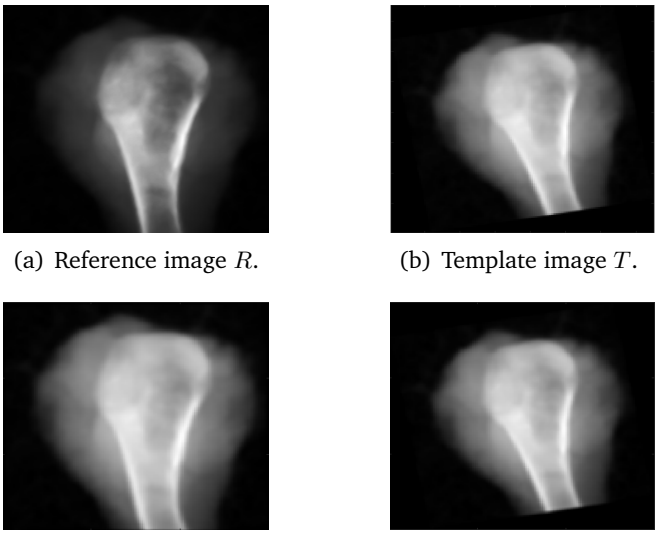

(a) Reference image R.

(b) Template image T.

(c) $T(\mathbf{u})$ by new model using **BZ** energy.

(d) $T(\mathbf{u})$ using Mumford-Shah energy.

Fig. 3.3 Example of registration of two medical images of a bone, which are described by a very sensitive geometrical information. The similarity term that is based on the **BZ** energy can solve the problem of weak edges and second-order discontinuities with acceptable registration. Whereas, the **MFS**-based model fails completely.

first- and the second-order derivatives (gradient and Hessian) of the deformation field $\mathbf{u}$ as follows:

$$J(\mathbf{u}) = \frac{\lambda}{2}\int_{\Omega}|\nabla\mathbf{u}|^2 d\mathbf{x} + \frac{\alpha}{2}\int_{\Omega}|\nabla^2\mathbf{u}|^2 d\mathbf{x}. \tag{3.11}$$

Based on these choices of the fidelity and regularization terms, we propose to register the two functions R, T from different image modalities by solving the following minimization problem:

$$\min_{\mathbf{u}\in\mathcal{W}}\left\{\mathcal{J}(\mathbf{u}) = \frac{1}{2}\|\mathcal{A}_T^{-1}(\beta) - \mathcal{A}_R^{-1}(\beta)\|_2^2 + \frac{\lambda}{2}\int_{\Omega}|\nabla\mathbf{u}|^2 d\mathbf{x} + \frac{\gamma}{2}\int_{\Omega}|\nabla^2\mathbf{u}|^2 d\mathbf{x}\right\}, \tag{3.12}$$

where λ and γ are regularization parameters, and

$$\mathcal{W} = (H_0^2(\Omega))^d := \left\{\mathbf{u}\in(H^2(\Omega))^d \text{ such that } \mathbf{u} = \mathbf{0} \text{ and } \frac{\partial\mathbf{u}}{\partial n} = \mathbf{0} \text{ on } \partial\Omega\right\}.$$

3.3 Mathematical analysis of the proposed model

The energy $\mathcal{J}(\mathbf{u})$ in (3.12) is non-convex with respect to $\mathbf{u}$ which makes the proof of the weak lower semi-continuity not straightforward. For that, we will use the concept of Carathéodory functions defined as follows:

Definition 5 *[TC19] Let $\Omega \subset \mathbb{R}^d$ be an open set and let $f : \Omega \times \mathbb{R}^n \times \mathbb{R}^{d\times n} \times \mathbb{R}^{d\times d\times n} \longrightarrow [0, +\infty]$ be a function satisfying the following assumptions:*

i) $f(\mathbf{x}, \cdot, \cdot, \cdot)$ is continuous for almost every $\mathbf{x} \in \Omega$,

ii) $f(\mathbf{x}, \mathbf{u}, \phi, \theta)$ is measurable in $\mathbf{x}$ for every $(\mathbf{u}, \phi, \theta) \in \mathbb{R}^n \times \mathbb{R}^{d\times n} \times \mathbb{R}^{d\times d\times n}$.

Then, f is called a Carathéodory function.

Now, we will start by giving some assumptions and lemmas, then we will apply some useful techniques about integrals of high-order operators which are needed to prove that our optimization problem admits a minimizer.

Definition 6 *Let $f : I \longrightarrow \mathbb{R}$, where I is a convex set. Then, f is a quasi-convex function if:*

$$\forall (x, y) \in I^2, \forall \sigma \in [0, 1], f(\sigma x + (1 - \sigma)y) \leq \max\{f(x), f(y)\}.$$

Lemma 3.3.1 *The operators $\mathcal{A}_T$ and $\mathcal{A}_R$ given in (3.9) are invertible in $\mathcal{V}$. Moreover, for Z_T and Z_R satisfying the problems (ET) and (ER), we have $\|Z_T\|_{L^2(\Omega)} = \|\mathcal{A}_T^{-1}(\beta)\|_{L^2(\Omega)}$ and $\|Z_R\|_{L^2(\Omega)} = \|\mathcal{A}_R^{-1}(\beta)\|_{L^2(\Omega)}$ are bounded by a constant c.*

PROOF 1 *In the proof, we use the notions $Z = Z_T$ or $Z = Z_R$, $\mathcal{A} = \mathcal{A}_T$ or $\mathcal{A} = \mathcal{A}_R$ and $S = T$ or $S = R$. In order to prove that $\mathcal{A}$ is invertible in $\mathcal{V}$, it is enough to prove that the problem*

$$\begin{cases} \mathcal{A}Z = \beta & \text{in } \Omega, \\ \frac{\partial Z}{\partial n} = 0 & \text{on } \partial\Omega, \end{cases} \tag{E}$$

admits a unique solution in $\mathcal{V}$. Indeed, the weak formulation associated with (E) consists in finding $Z \in \mathcal{V}$ such that

$$a(Z, \Psi) = \ell(\Psi), \ \forall \Psi \in \mathcal{V}, \tag{3.13}$$

where $\forall\, Z, \Psi \in \mathcal{V}$,

$$a(Z,\Psi) = 4\varepsilon^2\beta \int_\Omega \nabla Z \cdot \nabla \Psi d\mathbf{x} + \beta \int_\Omega Z\Psi d\mathbf{x} + 4\varepsilon \int_\Omega \left(\alpha|\nabla^2 S|^2 + \xi|\nabla S|^2\right) Z\Psi d\mathbf{x},$$
$$\ell(\Psi) = \int_\Omega \beta\Psi d\mathbf{x}.$$

Therefore, it is easy to check that the operator $a(\cdot,\cdot)$ *is coercive and continuous in* $\mathcal{V}\times\mathcal{V}$, *the linear operator* $\ell(\cdot)$ *is continuous in* $\mathcal{V}$. *Hence, the Lax-Milgram's theorem guarantees the existence and uniqueness of a solution of* (3.13). *Moreover, by substituting* Ψ *with* Z *in* (3.13), *we obtain*

$$4\varepsilon^2\beta \int_\Omega |\nabla Z|^2 d\mathbf{x} + \beta \int_\Omega |Z|^2 d\mathbf{x} + 4\varepsilon \int_\Omega \left(\alpha|\nabla^2 S|^2 + \xi|\nabla S|^2\right)|Z|^2 d\mathbf{x} = \beta \int_\Omega Z d\mathbf{x}.$$

The positivity of $4\varepsilon\int_\Omega(\alpha|\nabla^2 S|^2 + \xi|\nabla S|^2)|Z|^2 d\mathbf{x}$, *yields that*

$$4\varepsilon^2\beta \int_\Omega |\nabla Z|^2 d\mathbf{x} + \beta \int_\Omega |Z|^2 d\mathbf{x} \leq \beta \int_\Omega Z d\mathbf{x}.$$

From Cauchy-Schwarz's inequality, we obtain

$$\min(4\varepsilon^2, 1)\|Z\|_{\mathcal{V}}^2 \leq |\Omega|^{\frac{1}{2}}\|Z\|_{L^2(\Omega)},$$

which implies that

$$\min(4\varepsilon^2, 1)\|Z\|_{\mathcal{V}} \leq |\Omega|^{\frac{1}{2}}.$$

Consequently, we get

$$\|A_S^{-1}(\beta)\|_{L^2(\Omega)} \leq c \text{ where } c = \frac{|\Omega|^{\frac{1}{2}}}{\min(4\varepsilon^2, 1)}.$$

Lemma 3.3.2 ([Zho98]) *Let* $\Omega \subset \mathbb{R}^d$ *be an open set and* $f : \Omega \times \mathbb{R}^n \times \mathbb{R}^{d\times n} \times \mathbb{R}^{d\times d\times n} \longrightarrow [0, +\infty]$. *Then,* $\mathcal{J}(\mathbf{u}) = \int_\Omega f(\mathbf{x}, \mathbf{u}, \phi, \theta) d\mathbf{x}$ *is weakly lower semi-continuous in* $\mathcal{W}$ *if:*

i) f *is a Carathéodory function,*

ii) $f(\mathbf{x}, \mathbf{u}, \phi, \theta)$ *is quasi-convex with respect to* θ,

iii) $0 \leq f(\mathbf{x}, \mathbf{u}, \phi, \theta) \leq a(\mathbf{x}) + c(|\phi|^p + |\theta|^p)$ *where* $a(\mathbf{x}) \in L^1(\Omega), c > 0$.

Lemma 3.3.3 *Let the energy* $\mathcal{J}(\cdot)$ *be defined in* $\mathcal{W}$ *by:*

$$\mathcal{J}(\mathbf{u}) = \int_\Omega f(\mathbf{x}, \mathbf{u}, \nabla\mathbf{u}, \nabla^2\mathbf{u}) d\mathbf{x},$$

where

$$f(\mathbf{x},\mathbf{u},\nabla\mathbf{u},\nabla^2\mathbf{u}) = \frac{1}{2}|\mathcal{A}_T^{-1}(\beta) - \mathcal{A}_R^{-1}(\beta)|^2 + \frac{\lambda}{2}|\nabla\mathbf{u}|^2 + \frac{\gamma}{2}|\nabla^2\mathbf{u}|^2.$$

Then, the energy functional $\mathcal{J}(\mathbf{u})$ is coercive and weakly lower semi-continuous (wlsc) in $\mathcal{W}$.

PROOF 2 *We have:*

$$\mathcal{J}(\mathbf{u}) = \int_\Omega \left(\frac{1}{2}|\mathcal{A}_T^{-1}(\beta) - \mathcal{A}_R^{-1}(\beta)|^2 + \frac{\lambda}{2}|\nabla\mathbf{u}|^2 + \frac{\gamma}{2}|\nabla^2\mathbf{u}|^2\right) d\mathbf{x}.$$

From the positivity of $\int_\Omega \frac{1}{2}|\mathcal{A}_T^{-1}(\beta) - \mathcal{A}_R^{-1}(\beta)|^2 d\mathbf{x}$, we get:

$$\mathcal{J}(\mathbf{u}) \geq \int_\Omega \left(\frac{\lambda}{2}|\nabla\mathbf{u}|^2 + \frac{\gamma}{2}|\nabla^2\mathbf{u}|^2\right) d\mathbf{x} \geq \frac{\min(\lambda,\gamma)}{2}\int_\Omega \left(|\nabla\mathbf{u}|^2 + |\nabla^2\mathbf{u}|^2\right) d\mathbf{x}.$$

By using Poincaré's inequality, we have that $\|\mathbf{u}\|_{\mathcal{W}} = (\|\nabla\mathbf{u}\|_2^2 + \|\nabla^2\mathbf{u}\|_2^2)^{\frac{1}{2}}$ defines a norm in the space $\mathcal{W}$. So, we obtain

$$\mathcal{J}(\mathbf{u}) \geq \frac{\min(\lambda,\gamma)}{2}\|\mathbf{u}\|_{\mathcal{W}}^2,$$

which gives the coercivity of $\mathcal{J}(\cdot)$.

For the wlsc, we now verify that the function $f(\cdot)$ fulfills the assumptions in Lemma 3.3.2. Since the operators $\mathcal{A}_R^{-1}$ and A_T^{-1} are continuous almost every on their domains, the function $f(\cdot)$ is a Carathéodory. In addition, we have $f(\mathbf{x},\mathbf{u},\nabla\mathbf{u},\nabla^2\mathbf{u})$ is convex with respect to $\nabla^2\mathbf{u}$, which implies the quasi-convexity of $f(\cdot)$ with respect to $\nabla^2\mathbf{u}$. Moreover, we have

$$0 \leq f(\mathbf{x},\mathbf{u},\nabla\mathbf{u},\nabla^2\mathbf{u}) \leq a(\mathbf{x}) + c\left[|\nabla\mathbf{u}|^2 + |\nabla^2\mathbf{u}|^2\right],$$

where

$$c = \tfrac{1}{2}\max(\lambda,\gamma) \text{ and } a(\mathbf{x}) = \tfrac{1}{2}|\mathcal{A}_T^{-1}(\beta) - \mathcal{A}_R^{-1}(\beta)|^2.$$

Furthermore, since $\|\mathcal{A}_T^{-1}(\beta)\|_{L^2(\Omega)}$ and $\|\mathcal{A}_R^{-1}(\beta)\|_{L^2(\Omega)}$ are bounded (see Lemma 3.3.1). Then

$$a(\mathbf{x}) \leq \frac{1}{2}\left(|\mathcal{A}_T^{-1}(\beta)|^2 + |\mathcal{A}_R^{-1}(\beta)|^2\right) \in L^1(\Omega).$$

Consequently, the function $f(\cdot)$ fulfills the third condition of Lemma 3.3.2, which implies that the energy $\mathcal{J}(\mathbf{u})$ is weakly lower semi-continuous in $\mathcal{W}$.

Theorem 2 *The minimization problem (3.12) admits at least one solution in the space $\mathcal{W}$.*

PROOF 3 *Consider a minimizing sequence* $(\mathbf{u}_n)_{n\in\mathbb{N}} \subset \mathcal{W}$ *of* $\mathcal{J}(\cdot)$*, i.e.,*

$$\mathcal{J}(\mathbf{u}_n) \underset{n\to+\infty}{\longrightarrow} \min_{\mathbf{u}\in\mathcal{W}} \mathcal{J}(\mathbf{u}).$$

The coercivity of $\mathcal{J}(\cdot)$ *implies that* $(\mathbf{u}_n)_{n\in\mathbb{N}}$ *is uniformly bounded in* $\mathcal{W}$*. Thus, the boundedness of* $(\mathbf{u}_n)_{n\in\mathbb{N}}$ *guarantees that there exists a subsequence, still denoted* $(\mathbf{u}_n)_{n\in\mathbb{N}}$ *such that* $\mathbf{u}_n \underset{n\to+\infty}{\rightharpoonup} \mathbf{u}$ *in* $\mathcal{W}$*. By using the wlsc of* $\mathcal{J}(\cdot)$ *(Lemma 3.3.3), we get*

$$\mathcal{J}(\mathbf{u}) \leq \underset{n\longrightarrow+\infty}{lim} \mathcal{J}(\mathbf{u}_n) = \min_{\mathbf{u}\in\mathcal{W}} \mathcal{J}(\mathbf{u}),$$

Then, using the wlsc of $\mathcal{J}(\cdot)$*, we obtain that the limit* $\mathbf{u}$ *is a minimizer of* $\mathcal{J}(\cdot)$*.*

3.3.1 Discretization and algorithm

Let $\Omega =]0,1[^2$ be the unit square domain which we discretize by the uniform grid

$$\left\{\mathbf{x}^{i,j} = (x_1^i, x_2^j) = (ih, jh),\ 0 \leq i,j \leq n\right\},$$

where $h = \frac{1}{n}$. We discretize the displacement field $\mathbf{u}$ on the nodal grid $\mathbf{x}^{i,j}$ as $\mathbf{u}^{i,j} = (u_1^{i,j}, u_2^{i,j}) = (u_1(x_1^i, x_2^j), u_2(x_1^i, x_2^j))$. Using the lexicographical ordering, we reshape the matrices into two long vectors of dimension $\mathbb{R}^{2(n+1)^2\times 1}$

$$\begin{aligned} X &= (x_1^0,\dots,x_1^n,\dots,x_1^0,\dots,x_1^n,x_2^0,\dots,x_2^0,\dots,x_2^n,\dots,x_2^n)^T,\\ U &= (u_1^{0,0},\dots,u_1^{n,0},\dots,u_1^{0,n},\dots,u_1^{n,n},u_2^{0,0},\dots,u_2^{n,0},\dots,u_2^{0,n},\dots,u_2^{n,n})^T. \end{aligned}$$

Now, we discuss the discretization of the fidelity measure and regularization term.

Discretization of the fidelity measures

Let $\overrightarrow{R} = R(PX) \in \mathbb{R}^{n^2\times 1}$ be the discretized reference image and $\overrightarrow{T}(PX+PU) \in \mathbb{R}^{n^2\times 1}$ be the discretized template image, where $P \in \mathbb{R}^{2n^2\times 2(n+1)^2}$ is an averaging matrix for the transfer from the nodal grid representation of U to the cell-centered positions, see e.g., [CLM19; ZTC19a]. First, we introduce the two discrete operators: $D_1 = I_n \otimes \partial_h^1$ and $D_2 = \partial_h^1 \otimes I_n$, where $\otimes$ denotes the Kronecker product and ∂_h^1 is the 1-D first-order finite-difference operator

$$\partial_h^1 = \frac{1}{2h}\begin{bmatrix} -1 & 1 & & & \\ -1 & 0 & 1 & & \\ & \ddots & \ddots & \ddots & \\ & & -1 & 0 & 1 \\ & & & -1 & 1 \end{bmatrix} \in \mathbb{R}^{n\times n}.$$

The discretized ∇R and ∇T are defined by $\left[D_1\overrightarrow{R}, D_2\overrightarrow{R}\right]$ and $\left[D_1\overrightarrow{T}, D_2\overrightarrow{T}\right]$ respectively. Therefore, we have $|\nabla R|^2 = \sum_{i=1}^{2} D_i\overrightarrow{R} \odot D_i\overrightarrow{R}$ and $|\nabla T(\mathbf{u})|^2 = \sum_{i=1}^{2} D_i\overrightarrow{T} \odot D_i\overrightarrow{T}$ where $\odot$ indicates the component-wise product.

In order to discretize the Laplace operator, we introduce two discrete operators

$$\begin{aligned} D_{1,1} &= I_n \otimes \partial_h^2, \\ D_{2,2} &= \partial_h^2 \otimes I_n \end{aligned}$$

with

$$\partial_h^2 = \frac{1}{h^2}\begin{bmatrix} -2 & 1 & & \\ 1 & \ddots & \ddots & \\ & \ddots & \ddots & 1 \\ & & 1 & -2 \end{bmatrix} \in \mathbb{R}^{n\times n}.$$

Then, the discretized Laplace operator is $D_{1,1} + D_{2,2}$.

In order to discretize the Hessian, we introduce two discrete operators

$$D_{1,2} = D_{2,1} = B_h \otimes B_h,$$

where B_h is $n \times n$ matrix given by

$$B_h = \frac{1}{2h}\begin{bmatrix} 0 & 1 & & \\ -1 & \ddots & \ddots & \\ & \ddots & \ddots & 1 \\ & & -1 & 0 \end{bmatrix}$$

Thus, we have the discretized $|\nabla^2 R|^2 = \sum_{i=1}^{2}\sum_{j=1}^{2} D_{i,j}\overrightarrow{R} \odot D_{i,j}\overrightarrow{R}$ and $|\nabla^2 T(\mathbf{u})|^2 = \sum_{i=1}^{2}\sum_{j=1}^{2} D_{i,j}\overrightarrow{T} \odot D_{i,j}\overrightarrow{T}$.

Finally, the approximations of the operators A_T and A_R are expressed as follows

$$A_{\overrightarrow{T}} \approx -4\varepsilon^2\beta\left(D_{1,1} + D_{2,2}\right) + 4\varepsilon\left(\alpha\sum_{i=1}^{2}\sum_{j=1}^{2} D_{i,j}\overrightarrow{T} \odot D_{i,j}\overrightarrow{T} + \xi\sum_{i=1}^{2} D_i\overrightarrow{T} \odot D_i\overrightarrow{T}\right) + \beta$$

$$A_{\overrightarrow{R}} \approx -4\varepsilon^2\beta\left(D_{1,1} + D_{2,2}\right) + 4\varepsilon\left(\alpha\sum_{i=1}^{2}\sum_{j=1}^{2} D_{i,j}\overrightarrow{R} \odot D_{i,j}\overrightarrow{R} + \xi\sum_{i=1}^{2} D_i\overrightarrow{R} \odot D_i\overrightarrow{R}\right) + \beta$$

Hence, the approximations of $\mathcal{A}_T^{-1}(\beta)$ and $\mathcal{A}_R^{-1}(\beta)$ are given by

$$\mathcal{A}_{\overrightarrow{T}}^{-1}(\beta) \approx \mathcal{A}_{\overrightarrow{T}} \setminus \beta,$$
$$\mathcal{A}_{\overrightarrow{R}}^{-1}(\beta) \approx \mathcal{A}_{\overrightarrow{R}} \setminus \beta.$$

The discretized fidelity measure is given by

$$D_h^{BZ}(\overrightarrow{T}, \overrightarrow{R}) := \frac{h^2}{2} \left(\mathcal{A}_{\overrightarrow{T}}^{-1}(\beta) - \mathcal{A}_{\overrightarrow{R}}^{-1}(\beta)\right)^T \left(\mathcal{A}_{\overrightarrow{T}}^{-1}(\beta) - \mathcal{A}_{\overrightarrow{R}}^{-1}(\beta)\right). \tag{3.14}$$

Discretization of the regularization term

The goal is to discretize the functions u^1 and u^2 according to the forward difference, central difference, mid-point rule and Dirichlet boundary conditions. The approximation for the first-order and second-order regularization terms expressed as follows

$$\int_\Omega |\nabla \mathbf{u}|^2 d\mathbf{x} \approx \sum_{i=0}^{n-1}\sum_{j=0}^{n-1}\sum_{k=1}^{2} \left[\left(u_k^{i+1,j} - u_k^{i,j}\right)^2 + \left(u_k^{i,j+1} - u_k^{i,j}\right)^2\right],$$

and

$$\int_\Omega |\nabla^2 \mathbf{u}|^2 d\mathbf{x} \approx \frac{1}{h^2} \sum_{i=0}^{n-1}\sum_{j=0}^{n-1}\sum_{k=1}^{2} \left(u_k^{i,j} - u_k^{i+1,j} - u_k^{i,j+1} + u_k^{i+1,j+1}\right)^2$$
$$+ \frac{1}{h^2} \sum_{i=1}^{n-1}\sum_{j=1}^{n-1}\sum_{k=1}^{2} \left[\left(u_k^{i+1,j} - 2u_k^{i,j} + u_k^{i-1,j}\right)^2 + \left(u_k^{i,j+1} - 2u_k^{i,j} + u_k^{i,j-1}\right)^2\right].$$

In order to build the two matrices A_1 and A_2 and obtain a compact form, we introduce the discrete differential operator and use the Kronecker product that allows to find the following approximation:

$$\int_\Omega |\nabla \mathbf{u}|^2 d\mathbf{x} \approx h^2 U^T A_1 U, \quad \int_\Omega |\nabla^2 \mathbf{u}|^2 d\mathbf{x} \approx h^2 U^T A_2 U.$$

Then, we have the discrete regularization term which is given by

$$J_h(\mathbf{u}) := \frac{\lambda}{2} h^2 U^T A_1 U + \frac{\gamma}{2} h^2 U^T A_2 U. \tag{3.15}$$

Finally, combining the two terms (3.14) and (3.15), we get the discretized

formulation for the model (3.12)

$$\min_U \mathcal{J}_h(U) := \frac{h^2}{2}\left(\mathcal{A}_{\overrightarrow{T}}^{-1}(\beta) - \mathcal{A}_{\overrightarrow{R}}^{-1}(\beta)\right)^T\left(\mathcal{A}_{\overrightarrow{T}}^{-1}(\beta) - \mathcal{A}_{\overrightarrow{R}}^{-1}(\beta)\right) + \frac{\lambda}{2}h^2U^TA_1U + \frac{\gamma}{2}h^2U^TA_2U \tag{3.16}$$

3.3.2 Gradient and approximated Hessian

We set $r = \mathcal{A}_T^{-1}(\beta) - \mathcal{A}_R^{-1}(\beta)$. Then, the discretized fidelity measure (3.14) is $D_h^{BZ}(\overrightarrow{T}, \overrightarrow{R}) = \frac{h^2}{2}r^Tr$. Its gradient and approximated Hessian are given by, respectively,

$$\begin{cases} G_1 = h^2P^Tdr^Tr, \\ \mathcal{H}_1 = \frac{1}{2}h^2P^Tdr^TdrP. \end{cases}$$

The gradient and approximated Hessian of the discretized regularization term (3.15) are given by, respectively,

$$\begin{cases} G_2 = h^2(\lambda A_1 + \gamma A_2)U, \\ \mathcal{H}_2 = h^2(\lambda A_1 + \gamma A_2). \end{cases}$$

Therefore, by combining the above results for the two discretized terms, the gradient and the approximated Hessian of (3.16) are given by, respectively,

$$G_{\mathcal{J}} = G_1 + G_2, \tag{3.17}$$

$$\mathcal{H} = \mathcal{H}_1 + \mathcal{H}_2. \tag{3.18}$$

3.3.3 Gauss-Newton method

Since our discrete registration could be seen a non-linear least squares optimization problem, we use the Gauss–Newton algorithm which is well adapted for such problems, see [CC; Mod09; ZTC19a]. The algorithm is described below.

3.3.4 Multilevel technique

A major difficulty in the numerical approximation of the proposed model is the non-convexity of energy. Hence, the choice of the initial guess is very important for the convergence to the desired solution. Here, we get the initialization by a multiresolution technique, which avoids local minima and speeds up registration. We use a scale-space approach by resizing the original images to a sequence of

Algorithm 1 Gauss-Newton method by using Armijo line search for image registration: $U \leftarrow \text{GNIR}(U_0)$

Given U_0.
Starting with an initial guess $U \longleftarrow U_0$
For $k = 0, 1, 2, \cdots$ until convergence:

1. Evaluate $\mathcal{J}$ (3.16), $G_{\mathcal{J}}$ (3.17) and $\mathcal{H}$ (3.18) at U
2. Solve the descent direction from the linear equation $\mathcal{H}\delta U = -G_{\mathcal{J}}$
3. Find a positive scalar step-size s using line search scheme
4. Update $U \longleftarrow U + s\delta U$

coarser ones where computations are cheap and register these smaller images. Then, starting from the coarsest level, we interpolate the obtained transformation fields to get a starting guess on finer (next) levels until the original resolution on the finest level is reached.

3.4 Results and discussion

In the sequel, we present some numerical experiments for multi-modal images where we evaluate the performance and efficiency of the proposed model (which is denoted by **New model** below). We also compare it to two existing multi-modality models. The first one is the normalized gradient field model (denoted by **NGF** below) and the second one is the mutual information (denoted by **MI** below). To evaluate the quality of the registration results of the three models, we use the following error measures:

i) The mutual information: $MI_{\text{err}} = D^{MI}(T(\mathbf{u}), R)$,

ii) The normalized gradient fields: $NGF_{\text{err}} = D^{NGF}(T(\mathbf{u}), R)$,

which are given in (3.6) and (3.7). The good result means that it can lead to small NGF_{err} and large MI_{err}. In addition to the above two measures, we use the dice score (**DSC**) for images where segmentation are available. The **DSC** measures the overlap between two segmentations and is defined by

$$\textbf{DSC}(R, T) = 2\frac{|R \cap T|}{|R| + |T|} = 2\frac{\sum_i R^i T^i}{\sum_i (R^i + T^i)}. \tag{3.19}$$

For all the numerical experiments presented here, the comparison between the three models using the above measures is summarized in Tab. 3.1. The run time

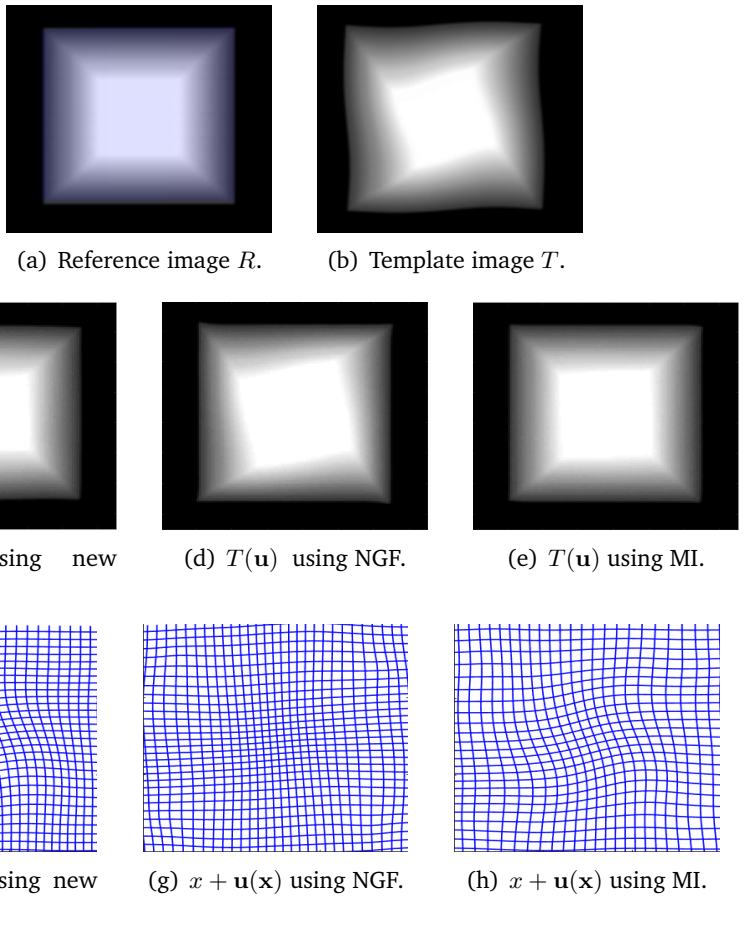

(a) Reference image R. (b) Template image T.

(c) $T(\mathbf{u})$ using new model. (d) $T(\mathbf{u})$ using NGF. (e) $T(\mathbf{u})$ using MI.

(f) $x + \mathbf{u}(\mathbf{x})$ using new model. (g) $x + \mathbf{u}(\mathbf{x})$ using NGF. (h) $x + \mathbf{u}(\mathbf{x})$ using MI.

Fig. 3.4 Example of registration of synthetic images of resolution 150×150 by three different models. **New model** is a very competitive to **MI**, and the advantage could be seen by checking the SSD error which is equal to 0.1 for **New model** and 0.15 for **MI**. However, the **NGF** fails completely in this case because the image is very smooth and the model will miss the edges.

comparison with the **MI** and **NGF** models is given in Tab. 3.2. All algorithms were implemented in MATLAB R2021b running on a Laptop with Intel (R) core(TM) i5 processor, CPU at 2.50 GHz and 8GB RAM memory at 2133 MHz. Since all three models are based on the Gauss-Newton method, a multilevel technique is used for the three models to accelerate the optimization process. The run-time comparison between **New model**, **MI** and **NGF** models shows the speed of each model and shows that there is a slight difference between them.

In Fig. 3.4, we consider a synthetic image of resolution 150×150 that contains sharp and smooth edges, i.e., first- and second-order discontinuities (see Figure 1). Here, we easily observe that the **NGF** registers well the outer boundaries of the large square and where the edges are sharp. However, for the inner square with smoothed edges and also on the diagonals of the large square, it fails completely. In contrast, the new model and the mutual information (MI) give accurate registration in almost

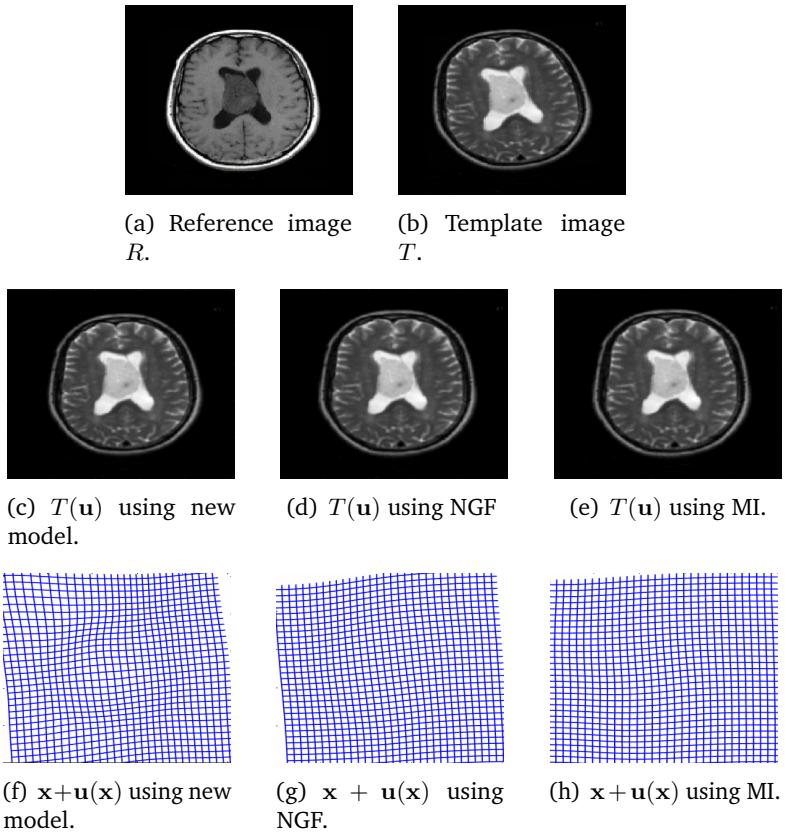

(a) Reference image R.

(b) Template image T.

(c) $T(\mathbf{u})$ using new model.

(d) $T(\mathbf{u})$ using NGF

(e) $T(\mathbf{u})$ using MI.

(f) $\mathbf{x}+\mathbf{u}(\mathbf{x})$ using new model.

(g) $\mathbf{x}+\mathbf{u}(\mathbf{x})$ using NGF.

(h) $\mathbf{x}+\mathbf{u}(\mathbf{x})$ using MI.

Fig. 3.5 Example of registration of two medical images (of 256×256) by three different models: **New**, **NGF** and **MI** models

all parts of the image. The difference can be seen only by checking the values of MI_{err} and NGF_{err}, which shows that our **New model** performs slightly better than **MI**.

In Fig. 3.5, the reference and the template image represent two different MRI cross sections of the brain of size 256×256. We compare with the different multi-modal registration models (**NGF** and **MI** models). For each model, we display the registered image $T(\mathbf{u})$ and the transformed grids which states the smoothness of the transformations. We quantify the quality of the registration by giving the mutual information and the normalized gradient fields between $T(\mathbf{u})$ and R, which are given in Table 3.1. The errors show that the proposed model gives better result compared to the two other models.

In Figs. 3.6 and 3.7, we test the competitive models in registering MRI inter-modal images, T1-weighted MRI to T2-weighted and T2-weighted MRI to FLAIR MRI. For each example, the segmentation label is given and which mainly gives the mask of the tumor region. For each model, we display the registered image, the registered tumor and the transformed grids.

Tab. 3.1 Comparisons between the three models.

Models	Errors	Our model	NGF model	MI model
Figure 3.4	NGF_{err}	0.19	0.23	0.2
	MI_{err}	0.85	0.75	0.82
Figure 3.5	NGF_{err}	0.37	0.36	0.37
	MI_{err}	1.77	1.71	1.74
figure 3.6	**DSC**	0.88	0.84	0.84
figure 3.7	**DSC**	0.94	0.84	0.87
figure 3.8	**DSC**	0.86	0.83	0.84

Tab. 3.2 Run time comparison for the three models of each figure i, i =3.4,3.5,3.6,3.7, 3.8.

model	Time (s) for our model	Time (s) for NGF model	Time (s) for MI
Figure 3.4	29.294	22.196	30.018
Figure 3.5	38.157	38.914	31.861
Figure 3.6	35.659	34.967	32.967
Figure 3.7	49.085	45.284	43.387
Figure 3.8	37.289	35.155	33.182

At the first step, we align the template image with the reference one by using the three models. Once the deformation for each case is computed, we use this deformation to deform the segmentation labels and compare the deformed mask and the reference mask using the **DSC** measure. The dice score for both examples shows clearly that the **new model** performs better than the other two models.

For the example in Fig. 3.6, the dice scores were **DSC**= 0.88 for **Mew model** and **DSC**= 0.84 for the other models. In fig.3.7, the Dice score for **New model** is equal to 0.94, but the **DSC**= 0.84 and the **DSC**= 0.87 for the **NGF** and **MI** models, respectively. In addition, the resulting transformation is smooth and has no folding.

To test the sensitivity of our model to noise, in Fig. 3.8, we add a white Gaussian noise, often abbreviated AWGN, in the reference and the template images with variance N=0.1 and the PSNR value is equal to 17.66. We show that our proposed model performs well in the presence of noise. Then, we compare it to the two multi-modality models (**NGF** and **MI** models). By checking the values which given in Tab. 3.1, the dice score **DSC** for the **New model** is equal to 0.86. However, **DSC**= 0.83 for the **NGF** model and **DSC**= 0.84 for the **MI** models. The **DSC** measure shows that the proposed model performs better then the two other models and that our model is stable at a certain high-level noise.

3.5 Conclusions

The non-parametric image registration for multi-modality images via a Normalized Gradient Field offers a fast and efficient registration method. However, in some cases, this model often has some difficulties such as non-clear edges. In this work, we have proposed a new similarity measure which is based on the Blake-Zisserman's energy. We addressed the benefit of using an energy of a second order to define the new fidelity measure. Experimental tests confirm that our proposed fidelity measure performs well in multi-modality image registration. In future work, we will consider possible generalizations of the model to three dimensions and also the use of the proposed energy in the context of unsupervised deep learning registration.

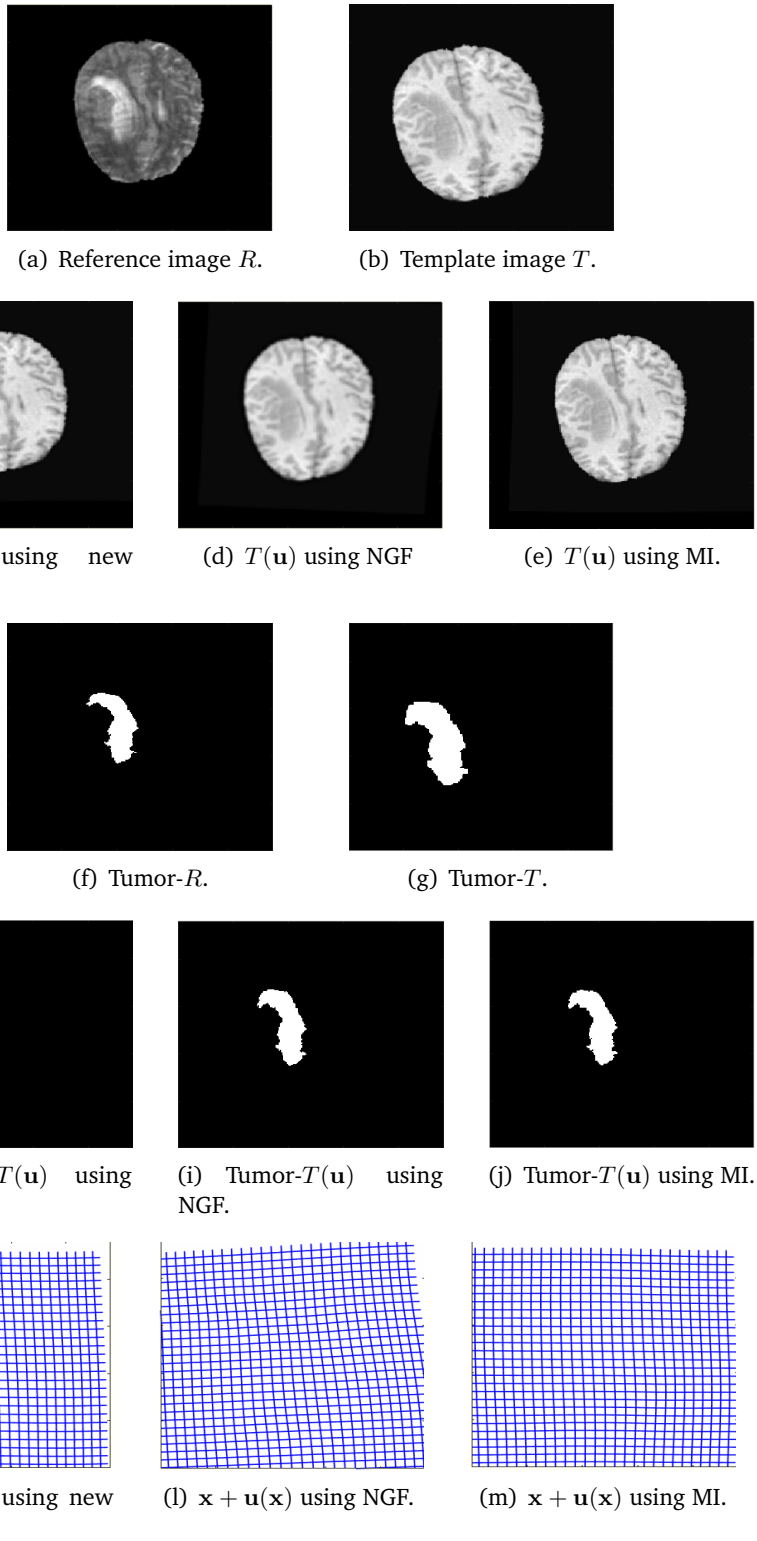

(a) Reference image R. (b) Template image T.

(c) $T(\mathbf{u})$ using new model. (d) $T(\mathbf{u})$ using NGF (e) $T(\mathbf{u})$ using MI.

(f) Tumor-R. (g) Tumor-T.

(h) Tumor-$T(\mathbf{u})$ using new model. (i) Tumor-$T(\mathbf{u})$ using NGF. (j) Tumor-$T(\mathbf{u})$ using MI.

(k) $\mathbf{x} + \mathbf{u}(\mathbf{x})$ using new model. (l) $\mathbf{x} + \mathbf{u}(\mathbf{x})$ using NGF. (m) $\mathbf{x} + \mathbf{u}(\mathbf{x})$ using MI.

Fig. 3.6 Example of registration of two MRI images by three different models. **New model** performs the best. **NGF** and **MI** perform identically.

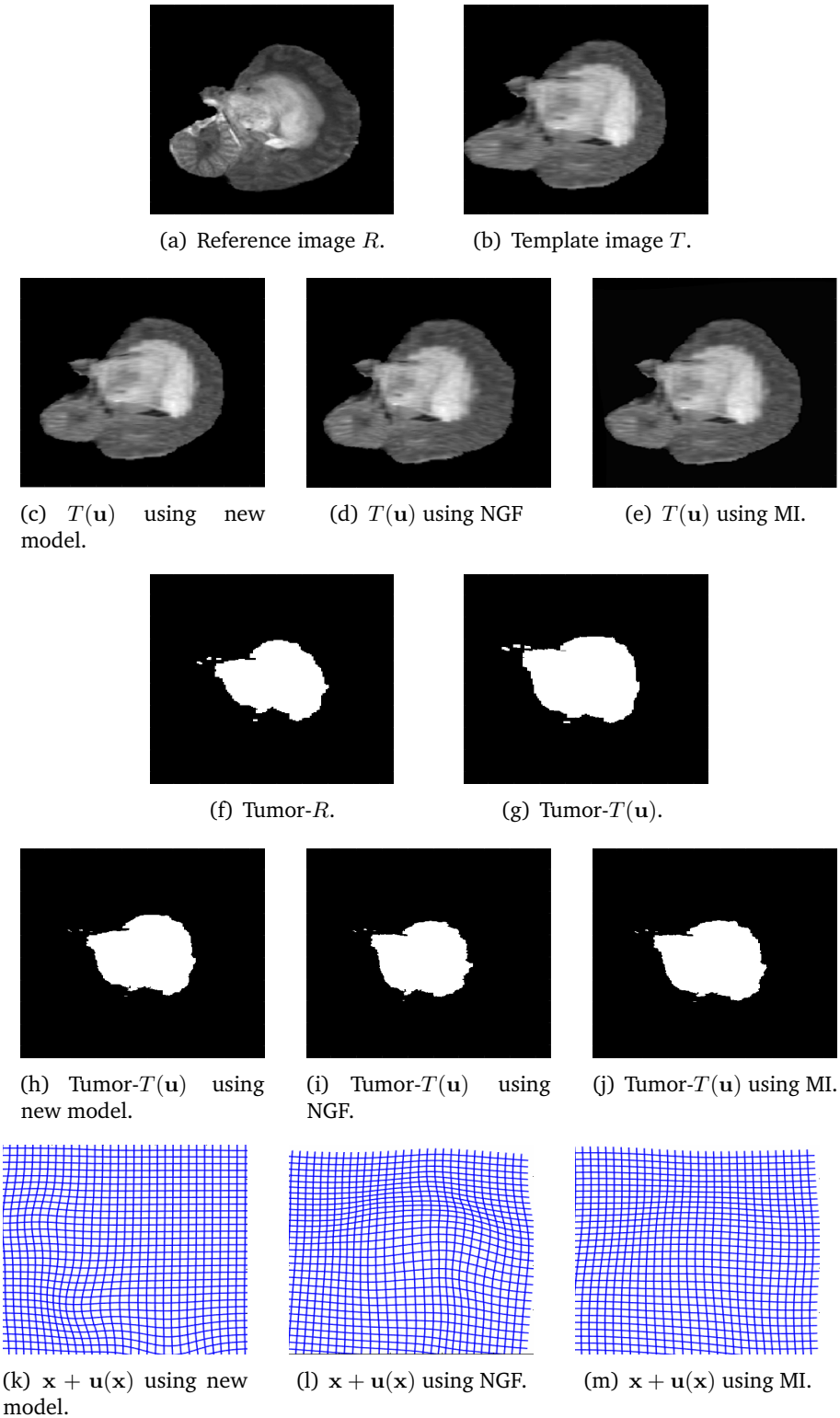

(a) Reference image R. (b) Template image T.

(c) $T(\mathbf{u})$ using new model. (d) $T(\mathbf{u})$ using NGF (e) $T(\mathbf{u})$ using MI.

(f) Tumor-R. (g) Tumor-$T(\mathbf{u})$.

(h) Tumor-$T(\mathbf{u})$ using new model. (i) Tumor-$T(\mathbf{u})$ using NGF. (j) Tumor-$T(\mathbf{u})$ using MI.

(k) $\mathbf{x} + \mathbf{u}(\mathbf{x})$ using new model. (l) $\mathbf{x} + \mathbf{u}(\mathbf{x})$ using NGF. (m) $\mathbf{x} + \mathbf{u}(\mathbf{x})$ using MI.

Fig. 3.7 Registration of a pair of MRI images (T2-weighted and FLAIR) of higher resolution 480×480 by three different models. The **New model** performs better than **NGF** and **MI**.

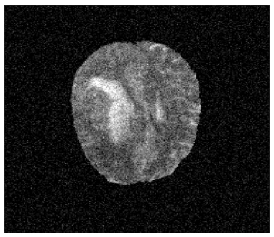

(a) Reference image R.

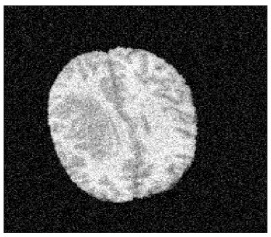

(b) Template image T.

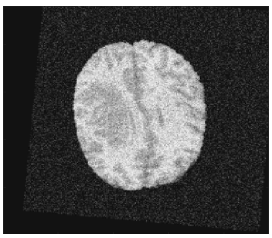

(c) $T(\mathbf{u})$ using new model.

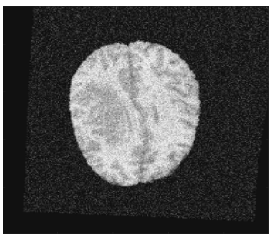

(d) $T(\mathbf{u})$ using NGF

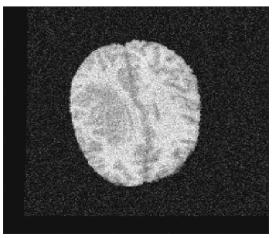

(e) $T(\mathbf{u})$ using MI.

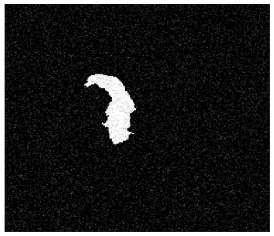

(f) Tumor-R.

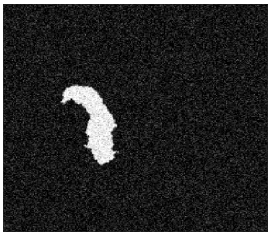

(g) Tumor-T.

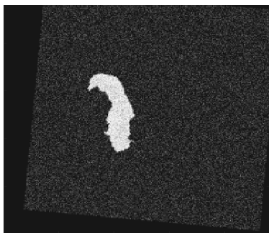

(h) Tumor-$T(\mathbf{u})$ using new model.

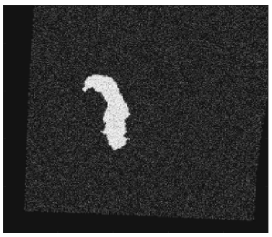

(i) Tumor-$T(\mathbf{u})$ using NGF.

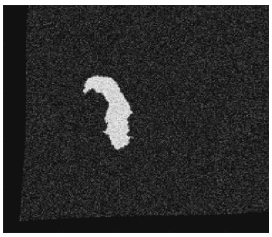

(j) Tumor-$T(\mathbf{u})$ using MI.

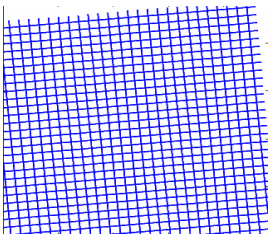

(k) $\mathbf{x} + \mathbf{u}(\mathbf{x})$ using new model.

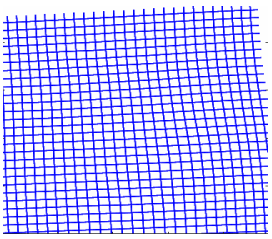

(l) $\mathbf{x} + \mathbf{u}(\mathbf{x})$ using NGF.

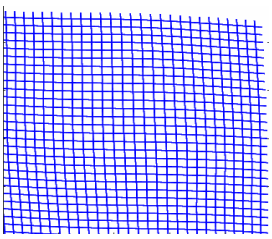

(m) $\mathbf{x} + \mathbf{u}(\mathbf{x})$ using MI.

Fig. 3.8 Example of registration of two MRI images by three different models in the case of the presence of noise. We consider noisy reference R and noisy template T with an additive white Gaussian noise, which have a variance N = 0.1 and the PSNR=17.66. **New model**, **NGF** and **MI** perform well

.

4 Unsupervised deep learning for geometric feature detection and multilevel multi-modal image registration

The aim of this chapter is to treat the previous idea presented in the last chapter with a deep learning technique. We introduce an effective approach for unsupervised multilevel image registration by leveraging geometric information extracted by using the Blake-Zisserman energy. Indeed, we propose to construct a neural network that predicts the geometric information of an image. Subsequently, we use this geometric information to define a second network dedicated to the process of multi-modal image registration. In order to achieve more efficient registration, we propose a novel deep neural network architecture that performs multilevel registration. This chapter is based on the article which is summarized bellow.

Summary

Deep learning approaches have been proposed in recent years to find spatial transformations that align two or more images [Bal+19; Qiu+21]. Generally, there are two main types of deep learning for image registration. The first one is called supervised learning approach [Cao+18; Hu+18a; Hu+18b] and the second one is called unsupervised learning approach[Hoo+21; Bal+18]. In the supervised case, the process requires training data that represent a ground-truth deformation field φ which may not be available at all. In the unsupervised case, we have a large set of data without ground-truth deformations. Subsequently, the self-trained of the deformations by image similarity metrics computed on the input data is proposed. The goal of this chapter is to develop an efficient unsupervised deep learning-based image registration method that can automatically establish geometric correspondences between two datasets. The proposed approach uses convolutional neural networks (CNNs) to detect geometric features and perform multilevel registration between the geometric information of two images. In order to detect the geometric

information, we propose using the Black-Zisserman's energy as a loss function to guide a CNN architecture. Subsequently, the objective is to minimize the expected loss:

$$Z_T^* = \arg\min_{Z_T} \left[\mathcal{L}_1(Z_T)\right] = \arg\min_{Z_T} \left[BZ_\varepsilon(T_s, Z_T)\right] \tag{4.1}$$

where,

$$\begin{aligned} BZ_\varepsilon(T_s, Z_T) = &\frac{\lambda}{2}\int_\Omega (T_s - T)^2 d\mathbf{x} + \alpha \int_\Omega Z_T^2 |\nabla^2 T_s|^2 d\mathbf{x} \\ &+ \xi \int_\Omega (Z_T^2 + \sigma)|\nabla T_s|^2 d\mathbf{x} + \beta \int_\Omega \left(\varepsilon |\nabla Z_T|^2 + \frac{(Z_T - 1)^2}{4\epsilon}\right) d\mathbf{x}, \end{aligned} \tag{4.2}$$

defined in the Sobolev space $H^2(\Omega) \times H^1(\Omega)$.

Then, using this geometric information, we propose to define a fidelity measure in the image registration process, i.e., we use the image edges, during the training for unsupervised learning image registration. Indeed, we propose the following loss function

$$\mathcal{L}_2 = \mathcal{L}_{32}(\varphi_{32}) + \mathcal{L}_{64}(\varphi_{64}) + \mathcal{L}_{128}(\varphi_{128}) \tag{4.3}$$

to train a convolutional neural network (CNN) that performs image registration between two images of 128×128 using the multilevel technique with three levels. Where

$$\begin{aligned} \mathcal{L}_s(\varphi_s) = &\lambda_1^s \left[1 - \mathbf{CC}(Z_{T_s}(\varphi_s), Z_{R_s})\right] \\ &+ \lambda_2^s \left[\|\nabla \varphi_s\|_2^2 + \|\nabla^2 \varphi_s\|_2^2 + \frac{1}{2}\|\psi\left[\det(\nabla(\mathbf{I}_2 + \varphi_s))\right]\|_2^2\right], \end{aligned} \tag{4.4}$$

Z_{T_s} (respectively Z_{R_s}) is the set of edges and thin structures of size $s \times s$, φ_s^i represents the deformation field of size $s \times s$ and $\psi(x) = \frac{(x-1)^4}{x^2}$.

In the following, we display the generic architecture of our neural network approach for unsupervised geometric information and image registration. In addition, in order to demonstrate the effectiveness of the two proposed loss functions in guiding the Deep Unsupervised Learning Segmentation and Image Registration process (denoted by **DULSIR** below), we evaluate the performance of the two loss functions on a dataset of 75 pairs of 2D MRI-CT images when the volumetric images are cropped to the size of 128×128. Numerical results demonstrate the efficiency and effectiveness of the proposed model. A comparison to the proposed method presented in the last chapter and that appeared in [Laj+22b] are given. Furthermore, to evaluate the quality of the registration results given by both models, two relatives errors are used which are given below.

Submitted: International Journal of Computer Vision

Received: 18-09-2023 / Revised: XXX / Accepted: XXX /

Abstract

We consider in this article an efficient unsupervised deep learning-based multilevel image registration approach benefiting from geometric features, namely edges and thin structures, extracted from the images. The extraction of such geometric information is based on a loss function derived from a variant of Mumford-Shah functional, that is the Blake-Zisserman's energy, in the training step. This energy, is well suited for detecting discontinuities at different scales, i.e., of first- and second-order kind. The new loss function that we propose allows us to achieve the detection of qualitative features with a deep learning approach and without labeled data. In a second step, we use this geometric information extracted from the input images, to define a second loss function and to perform our multi-modal image registration process. In addition, to achieve more accurate and efficient image registration, we propose a novel deep neural network architecture that performs multilevel image registration. By leveraging the power of deep learning, our approach enables us to obtain more precise image alignment than traditional methods. We perform some numerical simulations to show the accuracy and the relevance of our approach for multimodal registration and its multilevel implementation

keywords: Unsupervised image registration - Optimization - Variational models - High-order PDEs - Unsupervised edge detection.

4.1 Introduction

Deformable image registration is a well-known concept and it is a challenging image processing task that has applications in various fields like astronomy [BCS20], optics [Qua+20], remote sensing [Gos05], in which researchers generate a global picture from different partial views as in security [AD04] and compare current images with a data base and to tracking of objects as in robotics [Liu+19]. In addition, image registration is an important inverse problem in the domain of medical imaging which is summarized in Refs. [Hil+01; LA99; MV98], where

radiation therapy, computational anatomy, intervention and treatment planning, computer-aided diagnosis, fusion of different modalities, monitoring of diseases, or motion correction.

Indeed, usually a geometric deformation can occur during the steps of recording, reconstruction and transmission of images of the same object. Therefore, the images need to be geometrically aligned for better interpretation, especially in clinical diagnosis using medical images. The task of image registration is the process of transforming a moving image to be in anatomical correspondence with the fixed one. It consists in determining a geometrical transformation that aligns points in a given image of an object with corresponding points of that objectin another image. The two images could be different because they were taken with the same imaging device but at different times (mono-modality images) or were acquired using different devices like scanner, positron emission tomography (PET), magnetic resonance imaging (MRI), computer tomography (CT), etc (multi-modality images). In traditional image registration methods, the deformation is obtained by solving an optimization problem over a space of deformations based on similarity measure. This optimization problem is considered as a minimization of an energy which is composed of two parts

$$\min_{\mathbf{u}\in\mathcal{W}} \left\{\lambda_1 D\left[G_1(T(\varphi(\mathbf{x})), G_2(R(\mathbf{x}))\right] + \lambda_2 J(\mathbf{u})\right\}, \tag{4.5}$$

where the deformation field is defined via the displacement field, with $\varphi(\mathbf{x}) = \mathbf{x}+\mathbf{u}(\mathbf{x})$, $\mathcal{W}$ is a properly chosen functional space, G_1 and G_2 are two functions which depend on the two imaging modalities, R represents the fixed image which is called the reference image, and T represents the moving image which is called the template image, both images are represented by scalar-valued functions $R, T : \Omega \subset \mathbb{R}^d \longrightarrow \mathbb{R}$, where d denotes the spatial dimension of the images.

The first part of (4.5) is a fidelity term that measures similarities between $G_1(T(\varphi(\mathbf{x})))$ and $G_2(R(\mathbf{x}))$, and aims to minimize the misalignment between both images R and T so that they become very similar according to some pre-defined metric. The second part of (4.5) is a regularisation term which controls the smoothness of $\mathbf{u}$ and reflects our expectations by penalising unlikely transformations.

In the last few years, when mentioning deformable registration model of challenging images, we would automatically recommend deep learning based approaches such as U-Nets [RFB15b] and Fully Convolutional Networks (FCNs) [LSD15]. On the other hand, deep learning approaches have been proposed in recent years by exploring data-driven approaches and the incorporation of deep learning to learn these spatial transformations without some success [Bal+19; Qiu+21]. Generally, there are two

main types of deep learning image registration. The first one is called supervised learning approach [Cao+18; Hu+18a; Hu+18b] and the second one is called unsupervised learning approach [Hoo+21; Bal+18]. In the supervised case, the process requires training data which represents a ground-truth deformation field φ which may not be available at all. In order to overcome the lack of sufficient training data, recent works focus on training networks in an unsupervised case, i.e., larger set of data without ground-truth deformations. In order to obtain the deformation field, most of these works proposed the self-trained and driven of the deformations by image similarity metrics computed on the input data. Indeed, to train a convolutional neural network (CNN, or ConvNet), we minimize a loss function that has the following form

$$\varphi^* = \arg\min_{\varphi} [\mathcal{L}(\varphi)] = \arg\min_{\varphi} \{\lambda_1 D [G_1(T(\varphi(\mathbf{x})), G_2(R(\mathbf{x}))] + \lambda_2 J(\varphi)\}. \quad (4.6)$$

Most of the used CNN-based methods consider the intensity-based similarity metrics such as the normalized cross correlation(CC) or the mean squared error (MSE) as a fidelity measure [Ava+08; Bal+19]. Since these two terms make the registration between the pixels, then it is clear that such a measure only makes sense for mono-modal images, i.e., identity or linear relationship between the pixels. However, in the case of multi-modality images, the reference and the moving images were acquired from different devices. Hence they most likely have different contrasts and the relationship between the intensities of two images is often much more complex. For that, the two previous terms are normally not suitable for the challenging problem of multi-modal image registration. To overcome these limitations, the authors proposed the use of information-theoretic measures such as mutual information (MI) (see e.g., [Mae+97; PMV03; TC19]).

The term 'unsupervised' means that a suitable registration model is required. In this work, we aim at developing such a model. We propose to combine closely related tasks, i.e., using image segmentation to learn geometrical information for unsupervised deformable registration. The benefit of this proposal is independent of the types of images to be registered (i.e., mono-model or multi-model images). This idea could lead us from the multi-modal registration problem to a mono-modal one. Indeed, we propose an efficient unsupervised deep learning-based image registration approach that benefits from geometric information (edges and thin structures) extracted from the images using the Blake-Zisserman's energy, i.e., the image edges, during the training. This energy is well suited for detecting discontinuities at different scales, i.e., of first- and second- order. Indeed, we propose a new loss function defined by the Blake-Zisserman's function that can be used to achieve good detection quality of geometric information based on deep learning without labeled

data. Then, we use this geometric information in order to define a second loss function for the image registration process. Furthermore, we introduce a novel deep neural network architecture that enables multilevel image registration, leveraging the power of deep learning to achieve more accurate and efficient image alignment across multiple scales.
Believing in the elegance of the deformable registration model using neural networks, we aim to improve the unsupervised model for this case. Our main contributions can be summarized as follows:

- We have developed a CNN neural network that uses the Blake-Zisserman's energy as a loss function to predict the geometric information of a given image.
- We have built a CNN neural network that registers images by using the geometric information provided by the first neural network, allowing for the prediction of the geometric transformation and a registered image.
- To improve the accuracy and convergence of the model, we have integrated a multilevel technique in the second CNN network, enabling registration at different levels of image resolution. This technique enhances the quality of the registered image obtained and accelerates the training process.

This paper is organized as follows: in Section 2, we briefly discuss the benefits of the proposed loss functions and we introduce our new unsupervised deep learning-based image registration approach that benefits from geometric information (edges and thin structures) which is extracted from the images using a loss function defined by the Blake-Zisserman's energy, i.e., the image edges, during the training. Section 3 presents the data that were used to guide the unsupervised segmentation and registration process. In addition, this section displays numerical experiments. Finally, brief conclusions are drawn in Section 4.

4.2 Deep learning model

In this section, we propose a new unsupervised learning registration model for multi-modality images. This approach is based on geometric information which is furnished by a loss function defined by Blake-Zisserman's energy. We extend the idea from the work of Lajili *et al.* [Laj+22b]. Indeed, the authors address the problem of multi-modality image registration. Since the registration map cannot be guided by intensity matching, this type of registration is a challenging imaging problem. For that, the similarity term that measures the mis-matching between two images plays an important role. In [Laj+22b], a new similarity term based on

Blake-Zisserman's energy is proposed. This energy gives the geometric information, more specifically the edges and thin structures, to guide the registration process. The numerical method is based on the Gauss-Newton method and a multilevel technique to speed up the optimisation process. Experimental results seem to suggest that our method outperforms other registration approaches. In addition, a major difficulty in numerical optimization for image registration is the non-convexity of the model. Constructing a numerical optimization algorithm that avoids being trapped in a local minimum is very important for solving a non-convex model. In this work, we introduce a novel unsupervised deep neural network architecture that enables multilevel image registration which avoids the trapping into local minima and achieves more accurate and efficient image registration.

Moreover, the choice of the regularization parameter in the energy (4.5) has a key role to obtain a diffeomorphic registration. To the best of our knowledge, there is no theoretical result that can be used to choose the best values of these regularization parameters. We think that it very much depends on the given images. For this reason, in various works, the authors make several tests with different values of this parameter and then choose the one that gives the best result. However, when we train a network by minimizing the loss function which takes the form (4.6), the choice of the parameter λ is easier. Subsequently, the network learning process can adapt with this value and can estimate a dense deformation field to establish image-to-image correspondence.

4.2.1 Related work

The aim of this paper is to develop an efficient unsupervised deep learning-based image registration method that can automatically establish the geometrical correspondences between two datasets. The proposed approach uses a Convolutional Neural Network (CNN) to detect geometric features and perform multilevel registration between the geometric information of the two images. In the sequel, we suggest to use unsupervised deep learning-based image registration approach. To align the template image with the reference one, the proposed method involves the following steps. First, the CNN is trained on a large set of images to learn the feature representations that can effectively detect the geometric information. Second, the learned CNN is used to extract the corresponding geometric information from both images i.e., the template and the reference images. Then, a multilevel registration strategy is employed to align the geometric information of the two images.

Step one: Edge detection process

Often the geometric information (edges, gradient, Hessian) of the same object in different images is the same. Therefore, this information is useful for guiding the image registration process. In order to extract this information, there are various methods, e.g., the topological gradient method [ANV14; Laj+22a] that calculates the central differences between adjacent pixels, and the Mumford-Shah model [DR06] that consists of minimizing the following energy:

$$F_{MS}(g,\Gamma) = \frac{\lambda}{2}\int_{\Omega}(f-g)^2dx + \int_{\Omega\setminus\Gamma}|\nabla g|^2dx + \nu\mathcal{H}^1(\Gamma), \tag{4.7}$$

where $f : \Omega \subset \mathbb{R}^2 \longmapsto \mathbb{R}$ is the observed image that has to be segmented and that can be noisy, $g : \Omega \longmapsto \mathbb{R}$ is a piecewise smooth approximation of f to be determined and $\mathcal{H}^1(\Gamma)$ the Hausdorff measure that represents length of the edge set Γ.

In optimization problems of this kind, one of the major challenges is to develop efficient algorithms to compute a minima for this energy due to the non-regularity of the edge term and the non-convexity of the functional. Various algorithms have been proposed in the literature and a successful results have been obtained. We can cite the examples of algorithms that are based on the level-set method [TYW01; VC02]. In [Poc+09], the authors proposed a convex relaxation approach which allows the computation of high quality solutions of the piecewise-smooth Mumford-Shah segmentation problem and presented a convergent primal-dual algorithm to compute the solution of the convex representation of the Mumford-Shah functional. Moreover, Chambolle investigated a non-local approximation of the Mumford-Shah functional in [Cha99].

However, since the functional (4.7) is described by first-order derivatives, it cannot detect some features of the data, such as creases (gradient discontinuities) or 'discontinuity of second order', i.e., discontinuity of the Laplacian/Hessian (see e.g., [TB21; Laj+22b; Laj+22a]). However, this information may be valuable in clinical diagnosis using medical images which can be useful indicative information for doctors. Moreover, the weakness of the gradient detection is that it is very sensitive to noise and blur that are always present in the images. To overcome these limitations, Blake and Zisserman have proposed in [BZ87] to minimize an energy that uses first- and second-order discontinuities which takes the following form:

$$F_{BZ}(g,\Gamma,\Gamma_\nabla) = \frac{\lambda}{2}\int_{\Omega}(f-g)^2dx + \int_{\Omega\setminus(\Gamma\cup\Gamma_\nabla)}|\nabla^2 g|^2dx + \nu_1\mathcal{H}^1(\Gamma) + \nu_2\mathcal{H}^1(\Gamma_\nabla\setminus\Gamma), \tag{4.8}$$

where $g; \nabla g \in BV(\Omega)$. In order to compute the minima, Ambrosio et al. (2001) proposed the energy below by adapting the techniques of Γ-convergence. This energy is defined in the Sobolev space $H^2(\Omega) \times H^1(\Omega)$ by [AFM01; ZV13]:

$$BZ_\varepsilon(T_s, Z_T) = \frac{\lambda}{2}\int_\Omega (T_s - T)^2 d\mathbf{x} + \alpha \int_\Omega Z_T^2 |\nabla^2 T_s|^2 d\mathbf{x} + \xi \int_\Omega (Z_T^2 + \sigma)|\nabla T_s|^2 d\mathbf{x} + \beta \int_\Omega \left(\varepsilon |\nabla Z_T|^2 + \frac{(Z_T - 1)^2}{4\epsilon}\right) d\mathbf{x}. \tag{4.9}$$

By incorporating high-order derivatives terms, these high-order features could be easily detected by the variable Z_T. For example, in the works [Laj+22b; TB21], the authors display the benefit of using the B-Z energy for the denoising and the registration of images. In conclusion, results-driven in the latter works highlight the importance of the high-order terms in detecting and preserving thin structures.

In recent years, deep learning approaches have shown significant improvements in this area, especially with the use of convolutional neural networks (CNNs). In the present work, we propose a CNN architecture for geometric information detection that uses a loss function based on the Black Zisserman energy to enhance the detection accuracy. Subsequently, the objective is to minimize the expected loss:

$$Z_T^* = \arg\min_{Z_T} \left[\mathcal{L}_1(Z_T)\right] = \arg\min_{Z_T} \left[BZ_\varepsilon(T_s, Z_T)\right] \tag{4.10}$$

To better explain the CNN architecture, the neural network is a multi-layer convolutional network with layers of convolution, batch normalization, parametric rectified linear unit (PReLU), pooling, and upsampling.

The network begins with a 2D convolutional layer with learned filters defined by a parameter. This layer uses a convolution window of size 3×3 and a “same" padding, meaning that the output of the layer will have the same size as the input. The output of this layer is then normalized by batch (BatchNormalization) and activated by a PReLU. A pooling layer (MaxPooling2D) with a window of 2×2 is then applied to the output of the first convolutional layer to reduce the size of the representation. This process of convolution, normalization, and activation is repeated several times with deeper learned filters and smaller spatial resolution, until the size of the representation is small enough to allow for accurate edge detection.

The output of the last convolutional layer is then resized using an upsampling layer (UpSampling2D) to produce a geometric information map of the same size as the original input. This information map is then merged with the output of the first convolutional layer using a concatenation operation.

The network also includes a parallel branch that processes the original image with several layers of convolution and batch normalization to extract useful features for geometric information detection. This branch also produces a feature map that is merged with the edges map using a concatenation operation.

4.2.2 Step two: image registration process

In this sequel, we discuss our choice for the loss function $\mathcal{L}_2$ for the multi-modality image registration.

Let R, T: $\Omega \subseteq \mathbb{R}^2 \longrightarrow \mathbb{R}$ be two given observed images, where the first is considered as the reference image and the second is considered as the template image. In order to align the template image with the reference one, we propose the following steps:

First, we detect the edges and thin structures for both images R and T by minimizing the expected loss $\mathcal{L}_1$. Then, we use this geometric information in order to define a fidelity measure in the image registration process, i.e., we use the image edges, during the training for unsupervised learning image registration.

Choice of the geometrical measure $D(Z_T(\varphi), Z_R)$: In this work, we use an optimal measure of the similarity which is known as the normalized cross correlation (**CC**) and which must be maximized when there is a linear relation between the intensities of two images, e.g., the case of mono-modal images. The **CC** is defined as follows:

$$\mathbf{CC}(X, Y) = \frac{\mathbf{Cov}(X, Y)}{\sqrt{\mathbf{Var}(X)\mathbf{Var}(Y)}}, \tag{4.11}$$

where $\mathbf{Cov}(X, Y)$ is the covariance between X and Y, $\mathbf{Var}(X)$ and $\mathbf{Var}(Y)$ are the variance of X and Y, respectively.

Based on this choice, in order to minimize a similarity measure, we use the following geometrical measure

$$D(Z_T(\varphi), Z_R) = 1 - \mathbf{CC}(Z_T(\varphi), Z_R), \tag{4.12}$$

where Z_T (respectively Z_R) is the set of edges and thin structures that are detected from image T (respectively R) by minimizing the expected loss $\mathcal{L}_1$.

Choice of the regularizer $J(\cdot)$: In this work, we choose a robust regularizer that allows a smoothness outside the discontinuities of the displacement field $\mathbf{u}$ (we use first- and second-order derivatives, i.e., gradient and Hessian) and consists in a

smoothing constraints on the determinant. Accurately, this regularization term is given by:

$$J(\varphi) = \|\nabla\varphi\|_2^2 + \|\nabla^2\varphi\|_2^2 + \frac{1}{2}\|\psi\left[\ \det(\mathbf{I}_2 + \nabla\varphi)\right]\|_2^2, \tag{4.13}$$

where $\mathbf{I}_2$ is the 2×2 identity matrix, φ is a 2D vector field and $\psi(x) = \frac{(x-1)^4}{x^2}$. To explain the choice of this regularizer: the first regularization term is called "L2 gradient regularization". This regularization is often used in the context of optimizing vector fields for image segmentation or deformation regularization. The goal of this regularization is to promote smooth and continuous vector fields, by penalizing abrupt variations and discontinuities. By adding this regularization term to the cost function, the model is encouraged to produce a vector field whose gradient magnitude is small, which avoids sharp jumps and discontinuities[FM02b]. The second regularization term is called "curvature regularization" or "L2 Hessian norm regularization" [ZCY16]. In this expression, φ is a 2D vector field and $\nabla^2\varphi$ is the Hessian matrix of this vector field, which describes the curvature of the surface defined by the vector field. The goal of this regularization is to promote vector fields that have minimal curvature, by penalizing regions where the curvature is large. By adding this regularization term to the cost function, the model is encouraged to produce a vector field that has a smooth surface, with moderate curvature. By using this regularization, the model can performs better by avoiding the production of results that have regions with extreme curvature or singularities. This can improve the performance of the model by reducing overfitting. The third term in (4.13) is a form of regularization called "determinant regularization." This regularization is often used in the context of optimizing vector fields for image segmentation or deformation regularization. The regularization term is based on $\nabla\varphi = (\partial_j\varphi_i)_{i,j=1}^2$ in various works. The determinant of the matrix $(\mathbf{I}_2 + \nabla\varphi)$ is computed and then transformed by the function $\psi(x)$, which applies a stronger penalty for values of x near 1. The goal of this regularization is to promote smooth and continuous vector fields, by penalizing abrupt variations and discontinuities. Therefore, the volume is related to the determinant of the deformation. Subsequently, the addition of this term guarantees a sufficient growth of the penalty for small and large deformations respectively and ensures that the map is locally invertible [BMR13; DR04].

Using the regularizer $J(\mathbf{u})$ defined in (4.13), the model can better performs by avoiding producing results that are too “twisted" or “chaotic." This can improve the performance of the model by reducing overfitting.

Based on these two choices, we propose to train a convolutional neural network (CNN) by minimizing the following loss function

$$\varphi^* = \arg\min_{\varphi} \{\mathcal{L}_2(\varphi)\} = \arg\min_{\varphi} \{\lambda_1 [1 - \mathbf{CC}(Z_T(\varphi), Z_R)] + \lambda_2 \left[\|\nabla\varphi\|_2^2 + \|\nabla^2\varphi\|_2^2 + \frac{1}{2}\|\psi\left[\det(\nabla(\mathbf{I}_2 + \varphi))\right]\|_2^2 \right] \Big\}. \tag{4.14}$$

Deep neural network architecture that enables multilevel image registration

We propose a multilevel approach for image registration, which involves three levels of processing. The first and second levels are performed at resolutions of 1/4 and 1/2, respectively, while the third level operates at full resolution. Multilevel image registration offers several advantages over single-level registration methods. By processing images at different resolutions, the multilevel approach can handle large deformations in the image while maintaining high accuracy. This is because, at low resolutions, the network can detect more global features and large-scale deformations, while at high resolutions, it can detect fine details and small-scale deformations. Additionally, multilevel image registration can reduce the computational complexity of the registration process, as lower resolution images require less processing time and memory. Furthermore, the use of multiple levels can also help to avoid getting stuck in local optima during the registration process, as it provides multiple starting points for optimization. Overall, the multilevel approach can produce more robust and accurate image registration results in a more efficient manner than single-level methods.

In this work, we use a neural network to perform image registration between two images of size 128×128 using the multilevel technique with three levels. The network takes two images of size 128×128 as input and uses multiple convolution layers, maxpooling, upsampling, and concatenation to produce three registered images and three displacement maps of sizes 32×32, 64×64, and 128×128.

Specifically, the network starts with convolution layers to extract features from the two input images. Then, it uses a technique called maxpooling to reduce the size of the images while preserving important features. After that, the network uses a combination of convolution and upsampling layers to increase the size of the images and scale them to the next size.

The registration process is performed in three different levels using images of different sizes at each level.

- At the first level, the network uses images of size 32×32 resized using a pooling layer (MaxPooling2D) and produces a registered image and a displacement map of size 32×32.
- At the second level, it takes the registered image produced at the first level as a moving image and resizes it using an upsampling layer (Up-Sampling2D) to be of size 64×64, producing another registered image and displacement map of size 64×64.
- Finally, at the third level, it uses the registered image produced at the second level by applying an upsampling layer (Up-Sampling2D) to make it of size 128×128, producing a registered image and displacement map of size 128×128.

In conclusion, the neural network that we used employs multiple image processing techniques, such as convolution, maxpooling, upsampling, and concatenation, to produce registered images and displacement maps. This enables accurate and robust image registration results. Indeed, we propose to train a convolutional neural network (CNN) that performs image registration between two images of 128×128 using the multilevel technique with three levels. This will be achieved by minimizing the following loss function:

$$\mathcal{L}_2 = \mathcal{L}_{32}(\varphi_{32}) + \mathcal{L}_{64}(\varphi_{64}) + \mathcal{L}_{128}(\varphi_{128}) \tag{4.15}$$

where for $s = 32, 64, 128$:

$$\begin{aligned} \mathcal{L}_s(\varphi_s) =& \lambda_1^s \left[1 - \mathbf{CC}(Z_{T_s}(\varphi_s), Z_{R_s})\right] \\ &+ \lambda_2^s \left[\|\nabla \varphi_s\|_2^2 + \|\nabla^2 \varphi_s\|_2^2 + \frac{1}{2}\|\psi\left[\det(\nabla(\mathbf{I}_2 + \varphi_s))\right]\|_2^2\right], \end{aligned} \tag{4.16}$$

such as Z_{T_s} (respectively Z_{R_s}) is the set of edges and thin structures of size $s \times s$ and φ_s^i represents the deformation field of size $s \times s$.

4.2.3 Learning to detect geometric information and registration

In this section, we present our approach for unsupervised image registration using two trained convolutional neural networks. We begin by defining our input data set as $\mathbf{X} = \{X^i\}_{i=1}^N$, which consists of N pairs of images, where each pair $\mathbf{X}^i = [T^i, R^i]$ consists of a template image T^i and a reference image R^i. Our goal is to obtain two outputs: the first one is the geometric information $Z = Z_T$ or $Z = Z_R$ and the second one is the deformations field φ_s, $s \in \{32, 64, 128\}$, and registered images with different sizes.

To achieve this, we use two convolutional neural networks $\mathbf{CNN}_1$ and $\mathbf{CNN}_2$, which are trained to perform two different tasks. The first network $\mathbf{CNN}_1$ takes each pair $\mathbf{X}^i$ as input and outputs $\mathbf{Z}^i = [Z_{T^i}, Z_{R^i}]$, which contains the geometric information of each image. The second network $\mathbf{CNN}_2$ takes $\mathbf{Z} = \{Z^i\}_{i=1}^N$ as input and outputs the deformation field φ_s^i and registered images for each image pair.

We train $\mathbf{CNN}_1$ by minimizing the loss function $\mathcal{L}_1$ defined in (4.10). The purpose of this loss function is to ensure that the network produces accurate geometric information for each image. To train $\mathbf{CNN}_2$, we minimize the loss function $\mathcal{L}_2$ defined in (4.15). This loss function encourages the network to produce accurate deformation field that can align the template image with the reference one at each level. Fig. 4.1 shows the generic architecture of our neural network approach for unsupervised image registration.

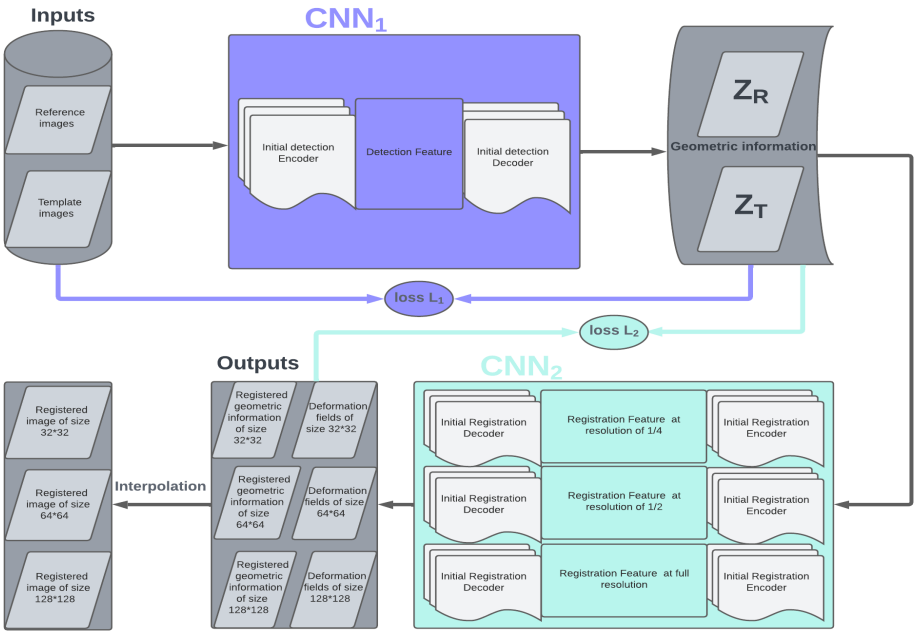

Fig. 4.1 Architecture of the proposed segmentation and registration model: Given two observed images R and T. First, in order to obtain the geometric information, the network $\mathbf{CNN}_1$ is trained by minimizing the loss function $\mathcal{L}_1$. Then, the network $\mathbf{CNN}_2$ is trained by minimizing the loss $\mathcal{L}_2$ that produces the deformations φ_s and registered images at different levels.

4.3 Data and numerical results

The objective of this section is to demonstrate the effectiveness of the two proposed loss functions in guiding the Deep Unsupervised Learning Segmentation and Image

Registration process which will be denoted by **DULSIR** below. To this end, we evaluate the performance of the two loss functions on a dataset of 75 pairs of 2D MRI-CT multi-modal images. The dataset consists of 75 different pairs of 2D MRI-CT images when the volumetric images are cropped to the size of 128×128.

4.3.1 A computational algorithm

For training the neural networks $\mathbf{CNN}_1$ and $\mathbf{CNN}_2$, the Adam optimization algorithm [Ado84] is used. Adam is a commonly employed algorithm that dynamically adjusts the weights of neural networks based on gradients computed from training data. The parameters: $\lambda_1^{32} = \lambda_1^{64} = \lambda_1^{128} = 0.5$, $\lambda_2^{32} = 0.02$, $\lambda_2^{64} = 0.04$ and $\lambda_2^{128} = 0.01$ are employed to regulate the relative relevance of regularization during network optimization.

Algorithm 2

Data: An initial guess Z_T.
Repeat until convergence

1. Solve the detection problem

$$Z_T^* = \arg\min_{Z_T} \left[\mathcal{L}_1(Z_T)\right] = \arg\min_{Z_T} \left[BZ_\varepsilon(T_s, Z_T)\right].$$

2. Solve the image registration problem

$$\varphi^* = \arg\min_{\varphi} \left\{\mathcal{L}_2\right\}.$$

4.3.2 Results and discussion

In the sequel, we present some examples to evaluate the efficiency of the proposed **DULSIR** model. To assess the performance of **DULSIR** model, we selected different reference images and employed the network to predict the registered images. The results clearly demonstrate the effectiveness and accuracy of our model. We also compare it to the proposed method presented in [Laj+22b] (which will be denoted by **ESM** below) that uses a method for image registration based on Blake-Zisserman type energy without learning, also known as traditional or classical methods. To evaluate the quality of the registration results of both models, we use the following error measures:

i) The relative mutual information error:

$$MI_{\text{err}} = \frac{D^{MI}(T_{\varphi_{128}}, R)}{D^{MI}(T(\mathbf{u}), R)},$$

where,

$$D^{MI}(T(\mathbf{u}), R) = -\int_{\mathbb{R}^2} p_{T,R}(t,r) \log \frac{p_{T,R}(t,r)}{p_T(t)p_R(r)} dtdr, \tag{4.17}$$

where $p_{T,R}$ is the joint probability of the gray values which can be derived from the joint histogram and p_T, p_R are the probability distributions of the gray values in T and R, respectively.

ii) The relative normalized gradient field error:

$$NGF_{\text{err}} = \frac{D^{NGF}(T_{\varphi_{128}}, R)}{D^{NGF}(T(\mathbf{u}), R)},$$

where

$$D^{NGF}(T(\mathbf{u}), R) = \int_{\Omega} \left[1 - \left(\frac{\nabla T(\mathbf{u}) \cdot \nabla R}{\sqrt{|\nabla T(\mathbf{u})|^2}\sqrt{|\nabla R|^2}} \right)^2 \right] d\mathbf{x}. \tag{4.18}$$

A good result is indicated by a small NGF_{err} and a large MI_{err}. The values of the above errors are summarized in Table 4.1. In addition to the above two measures, to evaluate the quality visually, we use the curves of evaluation metrics (4.10) and (4.15), that illustrate their values during the training iterations for the detection and registration model, and the fused image before and after registration.

In Fig. 4.2, the curves of evaluation metrics (4.10) and (4.15) are presented, illustrating their values during the training iterations for the detection and registration model. It can be observed that both (4.10) and (4.15) curves consistently converge towards zero. This indicates the excellent performance of the proposed model.

In Figs. 4.3 and 4.4, we present a collection of medical image registration examples in which we test the detection of geometric information and the registration of a MRI image to a CT. In each case, we have a reference image and a template image of size 128×128 and depicting the same object. For each example, we display the fused image before registration, the geometric deformation for the R and T (denoted by Z_R and Z_T, respectively) that are obtained by the first convolutional neural network, and the fused Z_R and Z_T before registration. The second convolutional neural network takes Z_T; Z_R as input and produces the registered image Z_{T_φ} and the transformed grids φ which states the smoothness of the transformations at different

Tab. 4.1 Comparisons between two models.

	Errors	**DULSIR** learning model	Traditional **ESM** model
Figure 4.3	NGF_{err}	1.22	–
	MI_{err}	1.31	–
Figure 4.4	NGF_{err}	1.05	–
	MI_{err}	1.30	–
Figure 4.5	NGF_{err}	1.2	1.27
	MI_{err}	1.38	1.37
Figure 4.6	NGF_{err}	1.07	1.15
	MI_{err}	1.27	1.27

three levels (see (g), (h), (i), (o), (p), and (q) in Figs. 4.3 and 4.4). To evaluate the quality of geometric image registration visually, we show the fused image between the geometric information after registration. Clearly the image Z_T is well aligned with the image Z_R. After that, we interpolate the obtained deformations in the template image that gives the registered images at different three levels displayed in (k), (l) and (m). Finally, we display the fused R and T after registration and we can easily see that the image T is well aligned with the image R. By checking the errors in Table 4.1, we could show that our proposed model performs well, where in the example in Fig. 4.3, the NGF_{err} and the MI_{err} are equal to 1.22 and 1.31, respectively. In addition, we have $NGF_{\text{err}} = 1.05$ and the $MI_{\text{err}} = 1.3$ in the second example displays in Fig. 4.4.

In Figs. 4.5 and 4.6, we compare the **DULSIR** model with the traditional multi-modal image registration model which is denoted by the **ESM** model. For each model, we display the reference and the template images, the fusion image before registration, the registered image for each model. We quantify the quality of registration by fusion R and T_φ (i.e., after registration) and by giving the relative normalized gradient field error and the relative mutual information error between R and $T\varphi$, which are given in Table 4.1. We can see that both models perform well for both examples and give satisfactory results.

In the example of Fig. 4.5, $NGF_{\text{err}} = 1.2$ and $MI_{\text{err}} = 1.38$ for new proposed **DULSIR** model. On the other hand, the NGF_{err} is equal to 1.27 and the MI_{err} is equal to 1.37 for the other model. The errors show that our proposed model performs slightly better than the **ESM** model. In Fig. 4.6, by checking the errors in Table 4.1, we could show that the relative mutual information error $MI_{\text{err}} = 1.27$ for both models, but the relative normalized gradient field error is equal to 1.07 for our proposed **DULSIR** model and $NGF_{\text{err}} = 1.15$ for the other model. The errors show that the proposed model gives a better result compared to the other model.

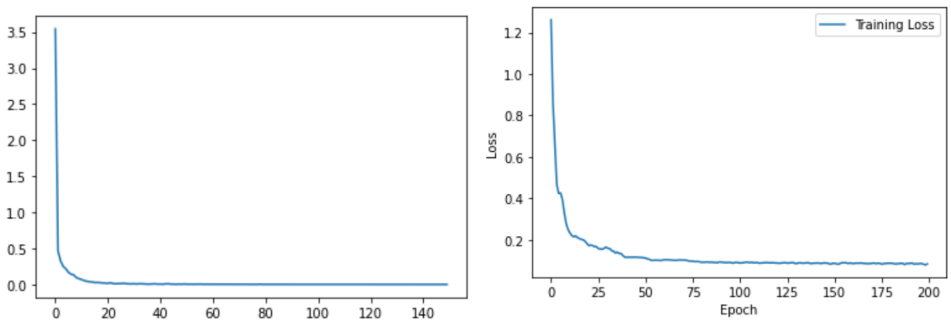

(a) $\mathcal{L}_1$ (b) $\mathcal{L}_2$

Fig. 4.2 The two loss functions: the curves of the evaluation metrics (4.10) and (4.15). Clearly, the curves of the two proposed model converge to zero in both networks.

4.4 Conclusion

The non-parametric image registration for multi-modality images is a challenging image processing task. In this work, we have proposed an approach to address and solve this problem using neural networks in the unsupervised case. We have developed and presented two unsupervised deep learning approaches for detecting the geometric information and multilevel image registration. Experimental tests have confirmed that our proposed architecture for detecting geometric information and multilevel multi-modality image registration perform well. In future work, we will consider generalizations of the model to three dimensional images.

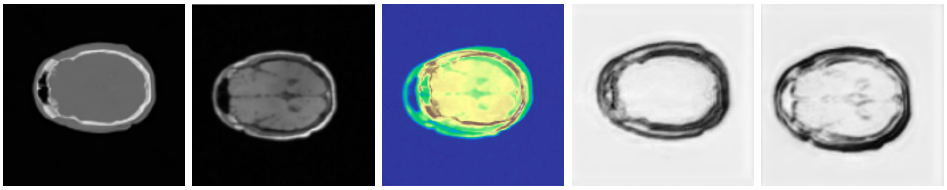

(a) R: Reference image (b) T: Template image (c) Fused R and T before registration (d) Z_R: Geometric information for R (e) Z_T: Geometric information for T

(f) Fused Z_R and Z_T before registration (g) $Z_{T_{\varphi_{32}}}$: Registered geometric information (h) $Z_{T_{\varphi_{64}}}$: Registered geometric information (i) $Z_{T_{\varphi_{128}}}$: Registered geometric information (j) Fused Z_R and $Z_{T_{\varphi_{128}}}$ after registration

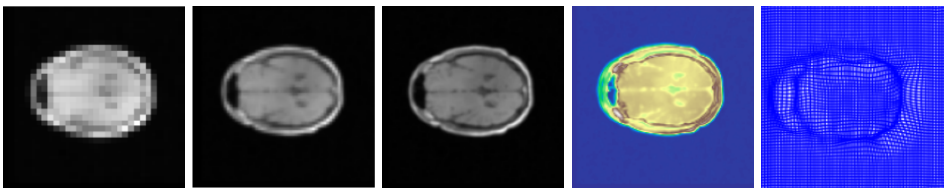

(k) $T_{\varphi_{32}}$: Registered image (l) $T_{\varphi_{64}}$: Registered image (m) $T_{\varphi_{128}}$: Registered image (n) Fused R and $T_{\varphi_{128}}$ after registration (o) The deformation φ_{32}

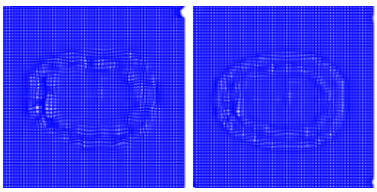

(p) The deformation φ_{64} (q) The deformation φ_{128}

Fig. 4.3 Example of prediction result for a pair of MRI-CT images by **DULSIR** learning model.

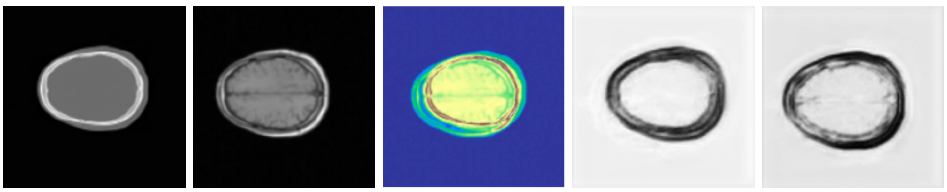

(a) R: Reference image (b) T: Template image (c) Fused R and T before registration (d) Z_R: Geometric information for R (e) Z_T: Geometric information for T

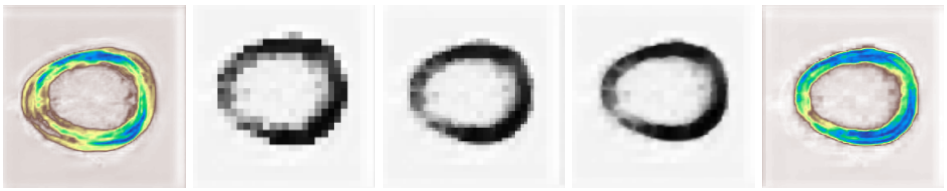

(f) Fused Z_R and Z_T before registration (g) $Z_{T_{\varphi_{32}}}$: Registered geometric information (h) $Z_{T_{\varphi_{64}}}$: Registered geometric information (i) $Z_{T_{\varphi_{128}}}$: Registered geometric information (j) Fused Z_R and $Z_{T_{\varphi_{128}}}$ after registration

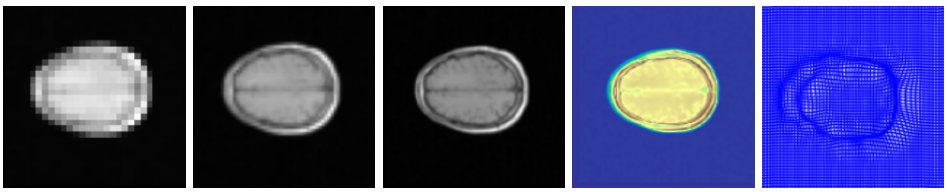

(k) $T_{\varphi_{32}}$: Registered image (l) $T_{\varphi_{64}}$: Registered image (m) $T_{\varphi_{128}}$: Registered image (n) Fused R and $T_{\varphi_{128}}$ after registration (o) The deformation φ_{32}

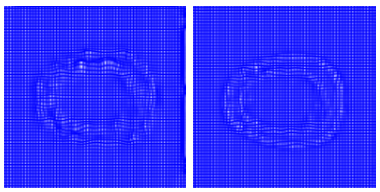

(p) The deformation φ_{64} (q) The deformation φ_{128}

Fig. 4.4 Example of prediction result for a pair of MRI-CT images by minimizing $\mathcal{L}_1$ and $\mathcal{L}_2$.

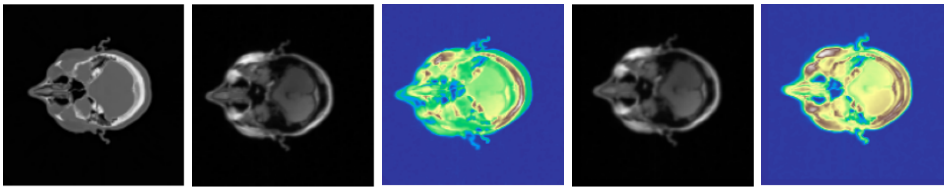

(a) R: Reference image (b) T: Template image (c) Fused R and T before registration (d) T_φ: Registered image with PROPO (e) Fused R and T_φ after registration

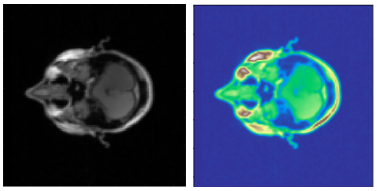

(f) T_φ: Registered image with Matlab (g) Fused R and T_φ after registration

Fig. 4.5 Example of visualization of the results after registering a pair of MRI-CT images. (d) represents the registered image obtained by minimizing $\mathcal{L}_1$ and $\mathcal{L}_2$. (f) represents the registered image using **ESM** model.

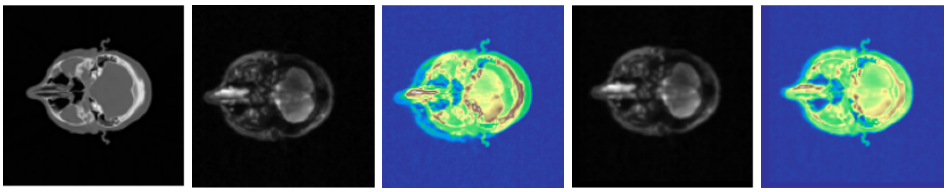

(a) R: Reference image (b) T: Template image (c) Fused R and T before registration (d) T_φ: Registered image with PROPO (e) Fused R and T_φ after registration

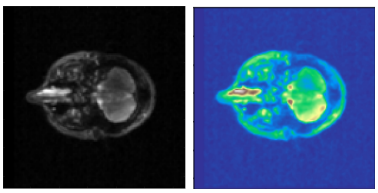

(f) T_φ: Registered image with Matlab (g) Fused R and T_φ after registration

Fig. 4.6 Example of visualization of the results after registering a pair of two pair MRI-CT images. (d) and (f) represent the registered image obtained by minimizing $\mathcal{L}_1$ and $\mathcal{L}_2$. (f) represents the registered image using **ESM** model.

5 Edge detection from X-ray tomographic data for geometric image registration

The aim of this chapter is the computation of the topological gradient associated to a second-order derivative in the cost function in a first step and use this result in a second step to build a robust and efficient similarity measure for deformable registration models from tomographic data. It is based on the article [Laj+22a] which is summarized below.

Summary

The concept of topological gradient method which has been formalized in [Mas02a; SZ99] for shape optimisation problems that has applications in various fields like inverse analysis and image processing [Aur09]. Essentially, the topological gradient approach works in the following way: let Ω be an open bounded domain of $\mathbb{R}^2$, $\Omega_\varepsilon = \Omega \backslash \overline{\omega_\varepsilon}$, $\overline{\omega_\varepsilon} = x_0 + \rho\omega$, $x_0 \in \Omega$, where ω is a fixed cavity domain centered at the origin, and $J_\varepsilon(u_\varepsilon)$ be a given cost function that defines the geometric structures of the image with respect to a small positive parameter ε where u_ε is a solution of the given PDE on the perforated domain Ω_ε. The main idea of the topological gradient approach is to provide the following asymptotic expansion of $J_\varepsilon(u_\varepsilon)$ as $\varepsilon \longrightarrow 0$:

$$J_\varepsilon(u_\varepsilon) = J_0(u_0) + f(\varepsilon)G(x_0) + o(f(\varepsilon)), \tag{5.1}$$

where $f(\varepsilon)$ is a positive function tending to zero when ε goes to 0 and $G(x_0)$ is the topological gradient expression at x_0.

The goal of this chapter is to extract a geometric information (edges and thin structures) from tomographic data in a first step and use this information in a second step to build a robust and efficient similarity measure. Indeed, in [AJR10] the authors have proposed to minimize the tomographic energy outside the edges:

$$\int_{\Omega_\varepsilon} |R(u_\varepsilon) - g|^2 dx + \lambda \int_{\Omega_\varepsilon} |\nabla u_\varepsilon|^2 dx. \tag{5.2}$$

The Euler-Lagrange equation associated to this problem is given by

$$\begin{cases} -\operatorname{div}(\lambda \nabla u_\varepsilon) + R^* R u_\varepsilon = R^* g, & \text{in } \Omega_\varepsilon, \\ \dfrac{\partial u_\varepsilon}{\partial n} = 0, & \text{on } \partial\Omega_\varepsilon, \end{cases} \tag{5.3}$$

where $\overrightarrow{n}$ denotes the outside unit normal vector to $\partial\Omega_\varepsilon$.

They have obtained the following asymptotic expansion in the case where ω is a thin crack and $j(\varepsilon) = J_\varepsilon(u_\varepsilon) = \displaystyle\int_{\Omega_\varepsilon} |\nabla u_\varepsilon|^2 dx$:

$$j(\varepsilon) - j(0) = \varepsilon^2 G(x_0) + o(\varepsilon^2),$$

with

$$G(x_0) = -\pi\lambda(\nabla u_0(x_0)\cdot n)(\nabla v_0(x_0)\cdot n) - \pi|\nabla u_0(x_0)\cdot n|^2, \tag{5.4}$$

where v_0 is the solution of the adjoint problem

$$\begin{cases} -\operatorname{div}(\lambda \nabla v_0) + R^* R v_0 = 2\Delta u_0, & \text{in } \Omega, \\ \dfrac{\partial v_0}{\partial n} = 0, & \text{on } \partial\Omega. \end{cases} \tag{5.5}$$

In the first part of this chapter, we propose to compute the topological gradient associated to a first and a second order derivative in the cost function and demonstrate the benefit of using the topological gradient of a high-order operator. In fact, the second-order derivative in the cost function is efficient to detect thin structures like points and filaments which represent an important information especially for the diagnostic of medical images. Moreover, in order to compute the topological gradient, we propose to perturb the domain Ω by inserting an ellipse centered at x_0 whose parametric equations are as follows:

$$\begin{cases} x_1 = a\cos(\theta), \\ x_2 = b\sin(\theta), \end{cases}$$

for all $\theta \in [0, 2\pi[$. Then, by taking $a = 1$ and by sending b to zero, we deduce the expression of the topological gradient in the case of a crack.

So we take the corresponding tomographic variational approach:

$$\min_{u_\varepsilon} \int_\Omega |R(u_\varepsilon) - g|^2 dx + \int_\Omega \alpha_\varepsilon |\Delta u_\varepsilon|^2 dx + \int_\Omega \beta_\varepsilon |\nabla u_\varepsilon|^2 dx. \tag{5.6}$$

- $\alpha_\varepsilon = \begin{cases} \alpha_0, & \text{on } \Omega \setminus \overline{\omega_\varepsilon}, \\ \alpha_1, & \text{on } \omega_\varepsilon. \end{cases}$ and $\beta\varepsilon = \begin{cases} \beta_0, & \text{on } \Omega \setminus \overline{\omega_\varepsilon}, \\ \beta_1, & \text{on } \omega_\varepsilon. \end{cases}$

- $\omega_\varepsilon = x_0 + \varepsilon E$ and E is an ellipse whose boundary ∂E is defined by

$$\partial E = \{X(\theta) = (a\cos(\theta), b\sin(\theta)), 0 \leq \theta \leq 2\pi \text{ and } a, b > 0\}.$$

In order to guarantee the existence and uniqueness of the solution u_ε, we propose to consider the following PDE:

$$\begin{cases} \Delta(\alpha_\varepsilon \Delta u_\varepsilon) - \operatorname{div}(\beta_\varepsilon \nabla u_\varepsilon) + R^* R u_\varepsilon + \mu u_\varepsilon = R^* g, & \text{in } \Omega, \\ \dfrac{\partial(\alpha_\varepsilon \Delta u_\varepsilon)}{\partial n} - \beta_\varepsilon \dfrac{\partial u_\varepsilon}{\partial n} = 0, & \text{on } \partial\Omega, \\ \Delta u_\varepsilon = 0, & \text{on } \partial\Omega. \end{cases} \tag{5.7}$$

where μ is a small positive parameter.

Then, we obtain the following expression of the topological gradient in the case of a crack:

$$g(x_0) = 4(\alpha_0 - \alpha_1)\left(\frac{\pi + 2}{2 - \pi}\right)\Delta v_0(x_0)\frac{\partial^2 u_0(x_0)}{\partial x^2}. \tag{5.8}$$

In the second part of this chapter, we propose a new variational model for mono/multi-modality images registration. This approach is based on geometric information which is detected by the topological gradient method (T-G). Let S_R, S_T: $\Omega \subseteq \mathbb{R}^2 \longrightarrow \mathbb{R}$ be two given observed X-ray tomographic data (sinograms), where the first is called sinogram of the reference image and the second is called sinogram of the template image. In order to align the template image with the reference one, we propose the following minimization problem:

$$\min_{\mathbf{u}\in\mathcal{W}} \left\{ \mathcal{J}(\mathbf{u}) = \frac{1}{2}\|TG(\mathbf{u}) - RG\|_2^2 + \frac{\lambda}{2}\int_\Omega |\nabla \mathbf{u}|^2 dx + \frac{\alpha}{2}\int_\Omega |\nabla^2 \mathbf{u}|^2 dx \right\}, \tag{5.9}$$

where TG (respectively RG) is the set of geometric informations that are detected from X-ray tomographic data S_T (respectively S_R) by the T-G method, λ and α are regularization parameters, and

$$\mathcal{W} = \left\{ \mathbf{u} \in \mathcal{W}_0^{1,2}(\Omega) \cap \mathcal{W}^{2,2}(\Omega) \text{ such that } \frac{\partial \mathbf{u}}{\partial n} = 0 \text{ on } \partial\Omega \right\}.$$

In the following, we provide a theoretical analysis of the proposed model by proving the existence of a solution. To numerically solve this proposed model, we use the Gauss-Newton algorithm and multilevel technique to accelerate the numerical computations for the solution of this model. Finally, we present numerical results carried out on different images and that are obtained using the proposed approach.

We also present numerical results which illustrate the sensitivity of our model to additive white Gaussian noise, often abbreviated AWGN, in sinogram with different variance. Furthermore, to evaluate the quality of the registration results given by the proposed model, we use the following error measure:

$$\mathcal{E}_r = \frac{\|RG - TG(\varphi)\|_2^2}{\|RG - TG\|_2^2}, \tag{5.10}$$

where $TG(\varphi)$ represents the registered geometric information.

Mathematical Methods in the Applied Sciences 46.6 (2023): 6324-6358.
https://doi.org/10.1002/mma.8905

Received: 17 March 2022/ Revised: 17 September 2022/ Accepted: 11 November 2022/ First published: 11 December 2022

Abstract

In this paper we propose new variational model for image registration from tomographic data. First, we employ the topological gradient approach for a tomographic reconstruction that uses the first- and the second-order discontinuities in order to detect important objects of a given observed X-ray tomographic data (sinograms). Second, we use this geometric information furnished by a high-order operator in order to define an appropriate fidelity measure for the image registration process. A theoretical study of the proposed model is provided, Gauss-Newton method and multilevel technique are used for its numerical implementation. The performed numerical experiments show the efficiency and effectiveness of our model.

keywords: Inverse problems, fidelity measures, image registration, X-ray tomography, topological gradient, edge maps.

5.1 Introduction

Image registration is a challenging image processing task that has applications in various fields like life sciences [Sch+15], astronomy [BCS20], optics [Qua+20], biology [AB20], chemistry [Zha+21], remote sensing [Gos05]. For instance, image registration is an important inverse problem in the domain of medical imaging. Indeed, usually a geometric deformation can occur during the steps of recording, reconstruction and transmission of images of the same object. Therefore, the images need to be geometrically aligned for better observation, especially in clinical diagnosis using medical images. The task of image registration is the determination of a geometrical transformation that aligns points in given image of an object with corresponding points in another image of that object. The two images could be different because they were taken at different times or were acquired using different devices like scanner, MRI, CT, etc. For details on image registration, the reader is

referred to [Gig+11; Mod09; SDP13; TC19]. The image registration modeling can be illustrated by considering a pair of images: a given fixed image R called the reference and a moving image T called the template, both represented by scalar functions R, T: $\Omega \subset \mathbb{R}^2 \longrightarrow \mathbb{R}$. The aim of image registration is to find a geometric transformation of the form $\boldsymbol{\varphi(x) = x + u(x)}$, where $\mathbf{u} : \mathbb{R}^2 \longrightarrow \mathbb{R}^2$ is a displacement field such that: aligns the two images, i.e.,

$$T\left[\varphi(\mathbf{x})\right] = T(\mathbf{x} + \mathbf{u}(\mathbf{x})) = R(\mathbf{x}). \tag{5.11}$$

In practice, the objective of image registration is to approximatively align the image T with the reference R by finding a reasonable deformation, in a way that the distance between R and a deformed version of T (registered image) is as small as possible. In parametric image registration, the type of the geometric transformation between these images is known a prism and expressed by a finite number of parameters (for example translation, rotation, etc). On the other hand, in the case of non-parametric image registration, the type of geometric transformation is unknown.

The reconstruction model (5.11) is an equation of the unknown displacement field $\mathbf{u}$, which is supposed to be sought in a properly chosen functional space. The model (5.11) is an ill-posed inverse problem and subsequently it is necessary to use regularization techniques. Generally, the regularization techniques turn an ill-posed problem into a well-posed problem. For this purpose, the problem (5.11) is reformulated as a minimization of an energy which is composed of two parts

$$\min_{\mathbf{u}\in(\mathcal{W}(\Omega,\mathbb{R}^2))} \left\{\phi\left(T(\mathbf{x} + \mathbf{u}(\mathbf{x}), R(\mathbf{x})\right) + \lambda J(\mathbf{u})\right\}, \tag{5.12}$$

where $\mathcal{W}(\Omega, \mathbb{R}^2)$ is a properly chosen functional space. The first part of the energy is a fidelity measure that quantifies similarity of the deformed version of $T(\mathbf{u})$ and the reference R. Indeed, the goal is to minimize (or to maximize) the term in which both images R and T are very similar. Generally, the choice of this term depends on the nature of images (mono-modality, multi-modality) to be registered. In the case of mono-modal images, i.e., the images are from the same modality (MRI T1, T2, X-ray laser), have same contrasts and similar features. Then, the preferred fidelity term of the energy (5.12) is often given by the SSD 'Sum of Squared Differences' or the CC 'correlation coefficient' between $T(\mathbf{u})$ and R. Since these two terms make the registration between the pixels, then it is clear that such a measure only makes sense for mono-modal images. For a pair of multi-modal images, both images have different contrasts and the relation between the intensities of the two images is often much more complex. Various similarity measures have been used, such as

'Normalized Gradient Field' (see e.g., [Hod+14; KR14; Ruh+13; TC19]), and 'the Mutual Information' (see e.g., [Mae+97; PMV03; TC19]).

The second part of the energy (5.12) is a regularization term which controls the smoothness of the displacement field $\mathbf{u}$ and reflects our expectations by penalizing unlikely transformations. From a mathematical point of view, the regularization term should turn the problem into a well-posed one, i.e., leads to a unique minimizer and also if it is possible to a convex objective function. There are several regularizers that have been proposed until now, for example first-order derivatives which are based on total variation (see [Hu+14]) and diffusion (see [FM02a]) and higher-order derivatives which are based on linear curvature.
In this paper, we are interested in deformable registration models from tomographic data. We suppose that the reference and the template images are given only by their tomographic measurements and should be simultaneously reconstructed and aligned. The idea, in this work, is to extract a geometric information (edges and thin structures) from tomographic data in a first step and use this information in a second step to build a robust and efficient similarity term. Indeed, in most registration models for multi-modality images, the intensities of the same object in different images are not similar, but it is very often that the geometry (edges, gradient, Hessian) is the same. Therefore, this geometric information is useful for defining a fidelity measure. As the gradient is described by first-order derivatives, it cannot detect discontinuity of second order, i.e., discontinuity of the Laplacian/Hessian. However this information may be valuable in clinical diagnosis using medical images and could be a very good indicative information for doctors. Moreover, the weakness of the gradient detection is also very sensitive to the noise that is always present in the images. To overcome these limitations, we use the topological gradient [ZF05; ROF92b; Nat01; Lew83; Hou+19] of a high-order operator which is well suited for detecting discontinuities at different scales i.e., of first and second order. Believing in the elegance of deformable registration model from tomographic data, we aim to improve the image registration model for this case. This paper is organized as follows. In Section 2, we briefly discuss the modeling of the X-ray tomography problem. In section 3, we give the formula of the topological gradient for the fourth-order model and display some examples which show the benefit of processing a fourth-th order model. Section 4 is devoted to introducing our new variational model for image registration which is based on topological gradient, and a theoretical analysis of the proposed model where we prove the existence of a solution. In Section 5 we present our numerical algorithm for topological gradient and image registration and Section 6 displays numerical experiments. Brief conclusions are drawn in Section 7.

5.2 The X-ray tomography problem

The X-ray tomography problem might be considered as the restoration of an image inside the human body from a set of projections called sinogram which are X-ray line integrals of the processed image at some disposed direction. In our work, for the sake of simplicity, we focus on the case of parallel beam tomography when the directions of the X-ray are assumed to be parallel. Mathematically, we can model the X-ray line integrals by the Radon transform operator [Nat01] which is defined as follows

$$R(f)(\theta, r) = \int_{\Omega} f(x, y)\delta(r - x\cos(\theta) - y\sin(\theta))dxdy,$$

where

- f is the processed image,
- Ω is an open bounded convex domain of $\mathbb{R}^2$,
- θ and r are the polar coordinates of the X-ray direction,
- $\delta(\cdot)$ is the Dirac punctual delta distribution.

For more information on the tomographic development and reconstruction approach, the reader is referred to [BB00; Dea07; Lew83; Nat01; ZF05]. In order to restore the image f, we must invert the Radon transform operator R. There are two ways to calculate the inversion formula for this problem.

- The first one is the analytic way based on the Fourier transform. The best one and the most used in this kind of inversion is the filtered back projection (FBP), it has a fast resolution algorithm and it is efficient in the absence of high noise level. The idea of this algorithm is to filter the Fourier transforms of the projections in the variable r and then to apply the explicit inverted Radon transform at the filtered Fourier mode projections. To be precise we give the steps of this algorithm referred to on the famous Fourier slice theorem [Nat01] as follows:
  1- Calculate the uni-dimensional Fourier transform $\widehat{F_r}$ of the projections with respect to the variable r:
  $$\widehat{F_r}R(f)(r, \theta).$$
  2- Filter the projections using a ramp filter:
  $$\widetilde{f}(\rho, \theta) = \widehat{F_r}^{-1}|r|\widehat{F_r}R(f)(r, \theta),$$
  where $\widehat{F_r}^{-1}$ is the inverse Fourier transform with respect to the variable r.

3- Restore the image f by applying the continuous back-projection transform R^* to $\widetilde{f}$:

$$f(x,y) = R^*\widetilde{f}(\rho,\theta) = \int_0^\pi \widetilde{f}(x\cos(\theta) + y\sin(\theta))d\theta.$$

- The algebraic formula is the second inversion way. It is based on the minimization over f of the following functional

$$\|R(f) - g\|^2 + \lambda\phi(f), \tag{5.13}$$

where g is the sinogram data, λ is a regularization parameter and ϕ is a regularization term. There are many ways to choose $\phi(f)$ (for more details see [Blo+97; CMM00; ROF92b]). In order to obtain a piecewise homogeneous image by preserving the majority of edges, the authors in [AJR10; Blo+97; CMM00] have shown that it is possible to consider $\phi(f) = \int_\Omega |\nabla f|^\alpha dxdy$ with $\alpha = 2$ in homogeneous parts and $\alpha = 1$ on the edges. The idea of this approach is to find edges with a fast and efficient optimization method, such as the topological gradient method [AM09], and then to solve the following problem

$$\begin{cases} -\operatorname{div}(\lambda(x)\nabla f) + R^*Rf = R^*g, & \text{in } \Omega, \\ \dfrac{\partial f}{\partial n} = 0, & \text{on } \partial\Omega, \end{cases} \tag{5.14}$$

with

$$\lambda(x) = \begin{cases} \dfrac{\lambda}{|\nabla f(x)|}, & \text{if } x \text{ belongs to the set of edges,} \\ \lambda, & \text{otherwise.} \end{cases} \tag{5.15}$$

and

$$R^*Rf = f * h, \text{ where } h(x,y) = \frac{1}{\sqrt{x^2+y^2}}. \tag{5.16}$$

This approach is not fast as the FBP algorithm, but is very efficient in the presence of high level of noise in the sinogram and there is a large choice to define an *a priori* regularization parameter λ that will produce a good image restoration result. Even though on the set of edges $|\nabla f|$ is not small, it is safer in the numerical implementation to replace the term $\frac{\lambda}{|\nabla f(x)|}$ in (5.15) by $\frac{\lambda}{\sqrt{|\nabla f(x)|^2+\varepsilon}}$, where ε is a small threshold parameter.

5.3 Topological optimization techniques for detecting geometric information from image

In this section, we study the problem of the detection of important features via the topological gradient method. In fact, there are two kinds of important features in the image: edges and thin structures. Every object in $(d-1)$-dimension can be linked to a structure that is assumed to be thin such as filaments in 3D or points in 2D. Generally, the derivation operator of first order detects edges and it is not efficient to detect thin structures. There are some arguments to explain this:

- The intensity of the image is modified across the edges, which is not the case for thin structures.
- The two geometric structures do not have the same profile: Dirac delta form for thin structures and Heaviside form for edges.
- A thin structure is a very small and irregular object. In the presence of noise, it is very difficult to see it by a derivation operator of first order.

For the above reasons, some previous works [ANV14; AD15; Dro14] have proposed to use the operators of second order to identify thin structures. Fortunately, the topological gradient method provides an efficient optimization topological tool to detect this kind of geometric structures [Dro14; Hou+19].

The main idea of the topological gradient approach is to derive the following asymptotic expansion:

$$J_\varepsilon(u_\varepsilon) - J_0(u_0) = f(\varepsilon)G(x_0) + o(f(\varepsilon)), \tag{5.17}$$

where,

- ε is a small positive parameter,
- J_ε (respectively J_0) is a given cost function that defines the geometric structures of the image with respect to the parameter ε (respectively with respect to the initial domain Ω),
- u_ε (respectively u_0) is a solution of the given PDE associated to tomographic problem on the perforated domain Ω_ε (respectively on the initial domain Ω),
- Ω is an open bounded convex domain of $\mathbb{R}^2$,
- $\Omega_\varepsilon = \Omega \backslash \overline{\omega_\varepsilon}$, $\overline{\omega_\varepsilon} = x_0 + \rho\omega$, $x_0 \in \Omega$, ω is a fixed cavity domain centered at the origin,

- $f(\varepsilon)$ is a positive function tending to zero when ε goes to 0,

- $G(x_0)$ is the topological gradient expression at x_0.

Generally, the choice of the cost function J_ε for the image restoration problem is based on the features of the geometric structures such as edges and thin structures. In order to preserve edges in the process of restoration the authors in [AF15; AHM05; Aur09; Bel+06] have used $J_\varepsilon(u_\varepsilon) = \int_{\Omega_\varepsilon} |\nabla u_\varepsilon|^2 dx$, where $|\cdot|$ denotes the Frobenius norm in $\mathbb{R}^2$. In some other works, such as [ANV14; AD15; Dro14], it has been shown that using the second-order derivative in the cost function is efficient to detect thin structures like points and filaments which are important information especially for the diagnostic of medical images. Recently, the authors in [Hou+19] have used the following cost function

$$J_\varepsilon(u_\varepsilon) = \alpha \int_{\Omega_\varepsilon} |\Delta u_\varepsilon|^2 dx + \beta \int_{\Omega_\varepsilon} |\nabla u_\varepsilon|^2 dx,$$

where α and β are two positive parameters chosen by respecting the priority of the detection of edges or thin structures.

In [AJR10] the authors have proposed to minimize the tomographic energy (5.13) outside the edges:

$$\int_{\Omega_\varepsilon} |R(u_\varepsilon) - g|^2 dx + \lambda \int_{\Omega_\varepsilon} |\nabla u_\varepsilon|^2 dx. \tag{5.18}$$

The Euler-Lagrange equation associated to this problem is

$$\begin{cases} -\operatorname{div}(\lambda \nabla u_\varepsilon) + R^* R u_\varepsilon = R^* g, & \text{in } \Omega_\varepsilon, \\ \dfrac{\partial u_\varepsilon}{\partial n} = 0, & \text{on } \partial\Omega_\varepsilon, \end{cases} \tag{5.19}$$

where $\overrightarrow{n}$ denotes the outside unit normal vector to $\partial\Omega_\varepsilon$.

They have obtained the following asymptotic expansion in the case where ω is a thin crack and $j(\varepsilon) = J_\varepsilon(u_\varepsilon) = \int_{\Omega_\varepsilon} |\nabla u_\varepsilon|^2 dx$:

$$j(\varepsilon) - j(0) = \varepsilon^2 G(x_0) + o(\varepsilon^2),$$

with

$$G(x_0) = -\pi\lambda(\nabla u_0(x_0) \cdot n)(\nabla v_0(x_0) \cdot n) - \pi |\nabla u_0(x_0) \cdot n|^2, \tag{5.20}$$

where v_0 is the solution of the adjoint problem

$$\begin{cases} -\operatorname{div}(\lambda \nabla v_0) + R^* R v_0 = 2\Delta u_0, & \text{in } \Omega, \\ \dfrac{\partial v_0}{\partial n} = 0, & \text{on } \partial\Omega. \end{cases} \tag{5.21}$$

In the present work, we propose to derive the asymptotic expansion defined in (5.17), by taking the following cost function

$$J_\varepsilon(u_\varepsilon) = \int_\Omega \alpha_\varepsilon |\Delta u_\varepsilon|^2 dx + \int_\Omega \beta_\varepsilon |\nabla u_\varepsilon|^2 dx, \tag{5.22}$$

where

- $\alpha_\varepsilon = \begin{cases} \alpha_0, & \text{on } \Omega \setminus \overline{\omega_\varepsilon}, \\ \alpha_1, & \text{on } \omega_\varepsilon. \end{cases}$ and $\beta\varepsilon = \begin{cases} \beta_0, & \text{on } \Omega \setminus \overline{\omega_\varepsilon}, \\ \beta_1, & \text{on } \omega_\varepsilon. \end{cases}$

- $\omega_\varepsilon = x_0 + \varepsilon E$ and E is an ellipse whose boundary ∂E is defined by

$$\partial E = \{X(\theta) = (a\cos(\theta), b\sin(\theta)), 0 \le \theta \le 2\pi \text{ and } a, b > 0\}.$$

So the corresponding tomographic variational approach becomes

$$\min_{u_\varepsilon} \int_\Omega |R(u_\varepsilon) - g|^2 dx + \int_\Omega \alpha_\varepsilon |\Delta u_\varepsilon|^2 dx + \int_\Omega \beta_\varepsilon |\nabla u_\varepsilon|^2 dx. \tag{5.23}$$

The Euler-Lagrange equation associated to this problem is

$$\begin{cases} \Delta(\alpha_\varepsilon \Delta u_\varepsilon) - \operatorname{div}(\beta_\varepsilon \nabla u_\varepsilon) + R^* R u_\varepsilon = R^* g, & \text{in } \Omega, \\ \dfrac{\partial(\alpha_\varepsilon \Delta u_\varepsilon)}{\partial n} - \beta_\varepsilon \dfrac{\partial u_\varepsilon}{\partial n} = 0, & \text{on } \partial\Omega, \\ \Delta u_\varepsilon = 0, & \text{on } \partial\Omega. \end{cases} \tag{5.24}$$

In order to guarantee the existence and uniqueness of the solution u_ε, we propose to relax the problem (5.24) as follows:

$$\begin{cases} \Delta(\alpha_\varepsilon \Delta u_\varepsilon) - \operatorname{div}(\beta_\varepsilon \nabla u_\varepsilon) + R^* R u_\varepsilon + \mu u_\varepsilon = R^* g, & \text{in } \Omega, \\ \dfrac{\partial(\alpha_\varepsilon \Delta u_\varepsilon)}{\partial n} - \beta_\varepsilon \dfrac{\partial u_\varepsilon}{\partial n} = 0, & \text{on } \partial\Omega, \\ \Delta u_\varepsilon = 0, & \text{on } \partial\Omega. \end{cases} \tag{5.25}$$

where μ is a small positive parameter.

Lemma 5.3.1 *The corresponding variational formulation of problem (5.25) is given by*

$$\begin{cases} \text{Find } u_\varepsilon \in \mathcal{V} \text{ such that:} \\ a_\varepsilon(u_\varepsilon, v) = l_\varepsilon(v), \ \forall\ v \in \mathcal{V}, \end{cases} \tag{5.26}$$

where

- $a_\varepsilon(u_\varepsilon, v) = \int_\Omega \alpha_\varepsilon \Delta u_\varepsilon \Delta v dx + \int_\Omega \beta_\varepsilon \nabla u_\varepsilon \nabla v dx + \int_\Omega R^* R u_\varepsilon v dx + \int_\Omega \mu u_\varepsilon v dx,$
- $l_\varepsilon(v) = \int_\Omega R^* g v dx,$
- $\mathcal{V}$ *is the Hilbert space defined by*

$$\mathcal{V} = \{u_\varepsilon \in H^2(\Omega) \text{ such that } \Delta u_\varepsilon = 0 \text{ on } \partial\Omega\}.$$

Lemma 5.3.2 *For each $\varepsilon \geq 0$, the cost function J_ε is differentiable on $\mathcal{V}$ and its derivative is given by*

$$DJ_\varepsilon(u_0)(u_\varepsilon - u_0) = \int_\Omega 2\alpha_\varepsilon \Delta u_0 \Delta(u_\varepsilon - u_0) dx + 2\int_\Omega \beta_\varepsilon \nabla u_0 \nabla(u_\varepsilon - u_0) dx. \tag{5.27}$$

Theorem 3 *There exist three real numbers δ_a, δ_l and δ_J that satisfy the following conditions:*

- $(a_\varepsilon - a_0)(u_0, v_\varepsilon) = \varepsilon^2 \delta_a + o(\varepsilon^2),$
- $(l_\varepsilon - l_0)(v_\varepsilon) = \varepsilon^2 \delta_l + o(\varepsilon^2),$
- $J_\varepsilon(u_\varepsilon) - J_0(u_0) = DJ_\varepsilon(u_0)(u_\varepsilon - u_0) + \varepsilon^2 \delta_J + o(\varepsilon^2),$

where v_ε is a solution of the adjoint problem

$$\begin{cases} \text{Find } v_\varepsilon \in \mathcal{V} \text{ such that:} \\ a_\varepsilon(w, v_\varepsilon) = -DJ_\varepsilon(u_0)w, \ \forall\ w \in \mathcal{V}. \end{cases} \tag{5.28}$$

In addition, we have:

$$
\begin{aligned}
\delta_l &= 0,\\
\delta_J &= ab\pi\left[(\alpha_1-\alpha_0)|\Delta u_0(x_0)|^2+(\beta_1-\beta_0)|\nabla u_0(x_0)|^2\right].\\
\delta_a &= ab\pi\left[(\alpha_1-\alpha_0)\Delta u_0(x_0)\Delta v_0(x_0)+(\beta_1-\beta_0)\nabla u_0(x_0)\nabla v_0(x_0)\right]\\
&\quad+(\alpha_0-\alpha_1)(k_0^{a,b}+1)\Delta v_0(x_0)\left(k_1^{a,b}\frac{\partial^2 u_0(x_0)}{\partial x^2}+k_2^{a,b}\frac{\partial^2 u_0(x_0)}{\partial y^2}\right.\\
&\qquad\left.+k_3^{a,b}\left(\frac{\partial^2 u_0(x_0)}{\partial x\partial y}+\frac{\partial^2 u_0(x_0)}{\partial y\partial x}\right)\right),
\end{aligned}
$$

where

$$
\begin{aligned}
k_0^{a,b} &= \frac{2\pi}{2\int_0^{\frac{\pi}{2}}\sqrt{a^2\cos^2(\theta)+b^2\sin^2(\theta)}d\theta-\pi},\\
k_1^{a,b} &= \int_0^{2\pi}\frac{a^2\cos^2(\theta)}{\sqrt{a^2\cos^2(\theta)+b^2\sin^2(\theta)}}\,d\theta,\\
k_2^{a,b} &= \int_0^{2\pi}\frac{b^2\sin^2(\theta)}{\sqrt{a^2\cos^2(\theta)+b^2\sin^2(\theta)}}\,d\theta,\\
k_3^{a,b} &= \int_0^{2\pi}\frac{ab\ \cos(\theta)\sin(\theta)}{\sqrt{a^2\cos^2(\theta)+b^2\sin^2(\theta)}}\,d\theta.
\end{aligned}
$$

The proof of existence of the three numbers δ_a, δ_l and δ_J is given in Appendix A 7.1.

Theorem 4 *The topological gradient expression associated to the cost function defined by* (5.22) *where* u_ε *is the solution of the problem* (5.23) *is given by:*

$$
\begin{aligned}
g(x_0) &= \delta_a-\delta_l+\delta_J,\\
&= ab\pi\left[(\alpha_1-\alpha_0)|\Delta u_0(x_0)|^2+(\beta_1-\beta_0)|\nabla u_0(x_0)|^2\right]\\
&\quad+ab\pi\left[(\alpha_1-\alpha_0)\Delta u_0(x_0)\Delta v_0(x_0)+(\beta_1-\beta_0)\nabla u_0(x_0)\nabla v_0(x_0)\right]\\
&\quad+(\alpha_0-\alpha_1)(k_0^{a,b}+1)\Delta v_0(x_0)\left(k_1^{a,b}\frac{\partial^2 u_0(x_0)}{\partial x^2}+k_2^{a,b}\frac{\partial^2 u_0(x_0)}{\partial y^2}\right.\\
&\qquad\left.+k_3^{a,b}\left(\frac{\partial^2 u_0(x_0)}{\partial x\partial y}+\frac{\partial^2 u_0(x_0)}{\partial y\partial x}\right)\right),
\end{aligned}
\tag{5.29}
$$

where u_0 *(respectively* v_0*) is the solution of problem* (5.23) *with* $\varepsilon=0$ *(respectively problem* (7.1)*).*

PROOF 4 *From the third assertion of Theorem 3 we have*

$$J_\varepsilon(u_\varepsilon) - J_0(u_0) = DJ_\varepsilon(u_0)(u_\varepsilon - u_0) + \varepsilon^2\delta_J + o(\varepsilon^2).$$

According to equation (5.28), we get

$$\begin{aligned} J_\varepsilon(u_\varepsilon) - J_0(u_0) &= -a_\varepsilon(u_\varepsilon - u_0, v_\varepsilon) + \varepsilon^2\delta_J + o(\varepsilon^2), \\ &= -a_\varepsilon(u_\varepsilon, v_\varepsilon) + a_\varepsilon(u_0, v_\varepsilon) + \varepsilon^2\delta_J + o(\varepsilon^2), \\ &= -a_\varepsilon(u_\varepsilon, v_\varepsilon) + a_0(u_0, v_\varepsilon) - a_0(u_0, v_\varepsilon) + a_\varepsilon(u_0, v_\varepsilon) + \varepsilon^2\delta_J + o(\varepsilon^2), \\ &= (a_\varepsilon - a_0)(u_0, v_\varepsilon) + (l_0 - l_\varepsilon)(v_\varepsilon) + \varepsilon^2\delta_J + o(\varepsilon^2). \end{aligned}$$

Then, according to the first and second assertions of Theorem 3, we deduce that

$$J_\varepsilon(u_\varepsilon) - J_0(u_0) = (\delta_a - \delta_l + \delta_J)\varepsilon^2 + o(\varepsilon^2).$$

The result of the previous theorem is proved for a particular case of an ellipse centered at x_0 whose parametric equations are as follows:

$$\begin{cases} x_1 = a\cos(\theta), \\ x_2 = b\sin(\theta), \end{cases}$$

for all $\theta \in [0, 2\pi[$. When we take $a = 1$ and send b to zero, we deduce the expression of the topological gradient in the case of a crack:

$$g(x_0) = 4(\alpha_0 - \alpha_1)\left(\frac{\pi + 2}{2 - \pi}\right)\Delta v_0(x_0)\frac{\partial^2 u_0(x_0)}{\partial x^2}. \tag{5.30}$$

The benefit of using the topological gradient of a high-order operator

It is clear that when $\alpha_\varepsilon = 0$, the above tomographic variational approach (5.23) corresponds to the well-known minimization problem (5.18) which uses only first order derivatives of an input image. In this case, the high-order topological gradient (5.30), that we have found, becomes an operator which is expressed by only first order derivative given by (5.20). This has disadvantage when, for example, the image contains a very sensitive geometrical information such as thin structures (points, filaments) which are not detectable by first-order derivatives. In order to show the efficiency of the proposed topological gradient approach in detecting thin-structures, we tested the proposed model for $\alpha_\varepsilon = 0$ and $\alpha_\varepsilon \neq 0$ for edge detection. In Fig. 5.1, we have three examples of images that contain thin structures; In Fig. 5.1(a), we assess the performance of the second-order T-G in detecting thin structures such as blood vessels and veins. In Fig. 5.1(b), we have a synthetic

image described by a very sensitive geometrical information. In Fig. 5.1(c), we show the efficiency of the second-order derivative for medical images. It is clear the map α_ε is unable to detect the gradient discontinuities. Then, the second-order topological gradient is more efficient than the first-order topological gradient in detecting thin structures. These results highlight the importance of the high-order terms in detecting and preserving thin structures.

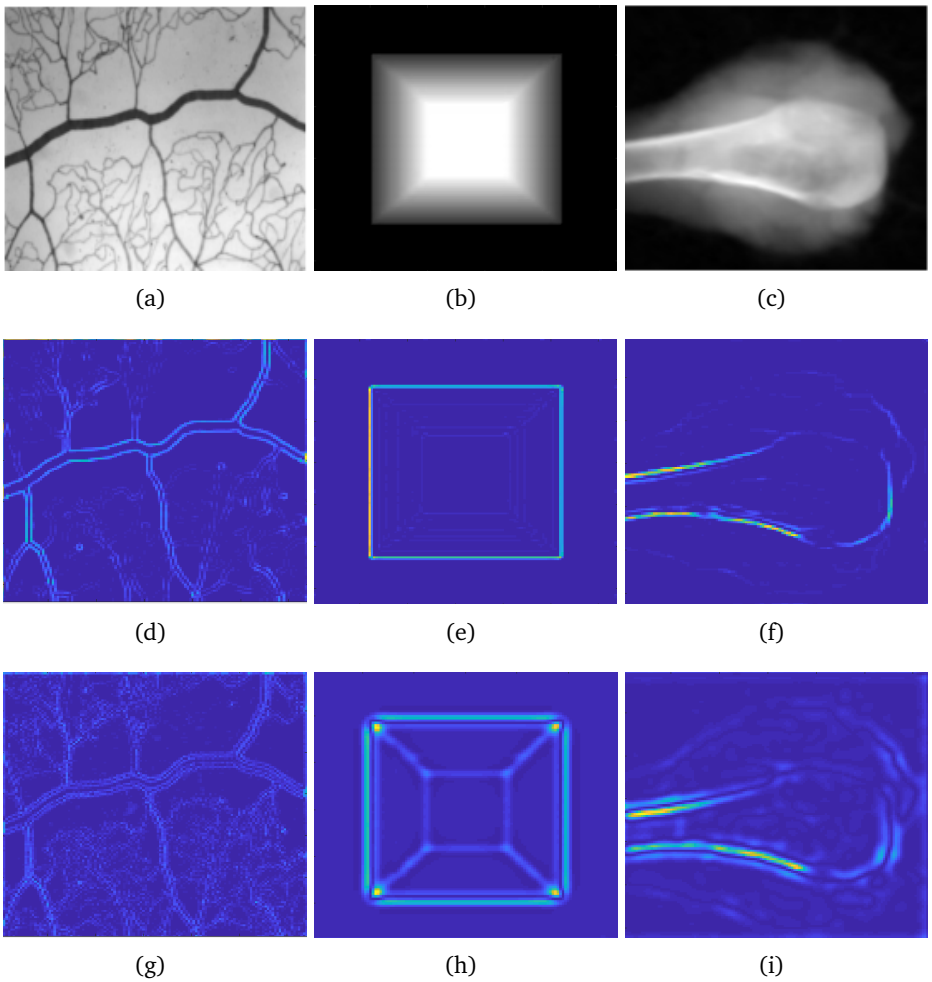

Fig. 5.1 Example of geometric information which are detected by the T-G of first and second order. (a), (b) and (c) original images. (d), (e) and (f) the map of β_ε: topological gradient for the second-order model ($\alpha_\varepsilon = 0$). (g), (h) and (i) the map of α_ε: topological gradient for the fourth-order model.

5.4 The proposed mono/multi-modality model

In this section, we propose a new registration model for mono/multi-modality images. This approach is based on geometric information which is detected by one

of the best topological optimization tools: the topological gradient method (T-G). Let S_R, S_T: $\Omega \subseteq \mathbb{R}^2 \longrightarrow \mathbb{R}$ be two given observed X-ray tomographic data (sinograms), where the first is called sinogram of the reference image and the second is called sinogram of the template image. In order to align the template image with the reference one, we propose the following steps:

First, we detect the edges and thin structures for both images from X-ray tomographic data using the topological gradient method. then, we use this geometric information which is obtained by the topological gradient in order to define a fidelity measure in the image registration process.

Second, we choose the fidelity measure which is based on the geometric structures that are detected from both images S_R and S_T, as follows:

$$\phi\left(T(\mathbf{x}+\mathbf{u(x)}, R(\mathbf{x})\right) = \frac{1}{2}\|TG(\mathbf{u}) - RG\|_2^2,$$

where RG (respectively TG) is the set of edges and thin structures that are detected from X-ray tomographic data S_R (respectively S_T) by the T-G method.

However, for the choice of the regularizer term, there is a large set of regularizer terms that have been used in previous works. This lead us to ask how to choose the best regularization term that gives the more possible plausible transformation. In this work, we choose a robust regularizer that allows a large smoothness outside the discontinuities, which is composed of both first- and second-order derivatives (gradient and Hessian) of the deformation field $\mathbf{u}$ as follows

$$J(\mathbf{u}) = \frac{\lambda}{2}\int_\Omega |\nabla \mathbf{u}|^2 dx + \frac{\alpha}{2}\int_\Omega |\nabla^2 \mathbf{u}|^2 dx.$$

Based on these two choices, we propose to register the two functions S_R, S_T by solving the following minimization problem:

$$\min_{\mathbf{u}\in\mathcal{W}} \left\{ \mathcal{J}(\mathbf{u}) = \frac{1}{2}\|TG(\mathbf{u}) - RG\|_2^2 + \frac{\lambda}{2}\int_\Omega |\nabla \mathbf{u}|^2 dx + \frac{\alpha}{2}\int_\Omega |\nabla^2 \mathbf{u}|^2 dx \right\}, \tag{5.31}$$

where λ and α are regularization parameters, and

$$\mathcal{W} = \left\{ \mathbf{u} \in \mathcal{W}_0^{1,2}(\Omega) \cap \mathcal{W}^{2,2}(\Omega) \text{ such that } \frac{\partial \mathbf{u}}{\partial n} = 0 \text{ on } \partial\Omega \right\}.$$

For the choice of two successive regularization parameters, the challenge is how to choose the good parameters which give the best diffeomorphic registration and hence the choice of a good one becomes delicate. In Fig. 5.2, we show the key role played by the choice of the parameters on the efficiency of regularization. In Fig. 5.2 (g), (h) (i) and (j), it is clear that the energy (5.31) is unable to minimize

the dissimilarity between R and T. In Fig. 5.2 (k) and (l), we assess that the variational method (5.31) is efficient in ensuring that the obtained transformation corresponds to a plausible deformation. These results highlight the importance of the regularization parameters in controlling the characteristics of the deformation (Fig. 5.2(h), (j) and (l)).

In the remainder of this section, we focus on the mathematical study of the proposed model. Our goal is to prove that problem (5.31) has at least one solution in the space $\mathcal{W}$. The energy $\mathcal{J}(\mathbf{u})$ is non-convex with respect to $\mathbf{u}$ and consequently, the proof of the weak lower semi-continuity is not straightforward. For that, we will use the concept of Carathéodory functions defined in [TC19] as follows:

Definition 7 *Let $\Omega \subset \mathbb{R}^d$ be an open set and let $f : \Omega \times \mathbb{R}^n \times \mathbb{R}^{d\times n} \times \mathbb{R}^{d\times d\times n} \longrightarrow [0, +\infty]$ satisfies the following assumptions:*

- *$f(x, \cdot, \cdot, \cdot)$ is continuous for almost every $x \in \Omega$,*
- *$f(x, \mathbf{u}, \phi, \theta)$ is measurable in x for every $(\mathbf{u}, \phi, \theta) \in \mathbb{R}^n \times \mathbb{R}^{d\times n} \times \mathbb{R}^{d\times d\times n}$.*

Then f is a Carathéodory function.

Definition 8 *Let $f : I \longrightarrow \mathbb{R}$, where I is a convex set. Then, f is a quasi-convex function if*

$$\forall (x, y) \in I^2, \forall \lambda \in [0, 1], f(\lambda x + (1 - \lambda)y) \leq \max \{f(x), f(y)\} .$$

Now, we will start by giving some assumption and Lemmas which are needed to prove that our optimization problem admits a minimizer.

We will assume that:

- The fixed image RG and the moving image TG are continuous.
- $|TG(\mathbf{u})|$ and $|RG|$ are bounded almost everywhere by a constant $c > 0$.

Lemma 5.4.1 *[TC19]*
Let $\Omega \subset \mathbb{R}^d$ be an open set and $f : \Omega \times \mathbb{R}^n \times \mathbb{R}^{d\times n} \times \mathbb{R}^{d\times d\times n} \longrightarrow [0, +\infty]$. Then, $\mathcal{J}(\mathbf{u}) = \int_\Omega f(x, \mathbf{u}, \phi, \theta)dx$ is weakly lower semi-continuous in $\mathcal{W}$ if:

- *f is a Carathéodory function,*
- *$f(x, \mathbf{u}, \phi, \theta)$is quasi-convex with respect to θ,*
- *$0 \leq f(x, \mathbf{u}, \phi, \theta) \leq a(x) + C(|\phi|^p + |\theta|^p)$ where $a(x) \in L^1(\Omega)$ and $C > 0$.*

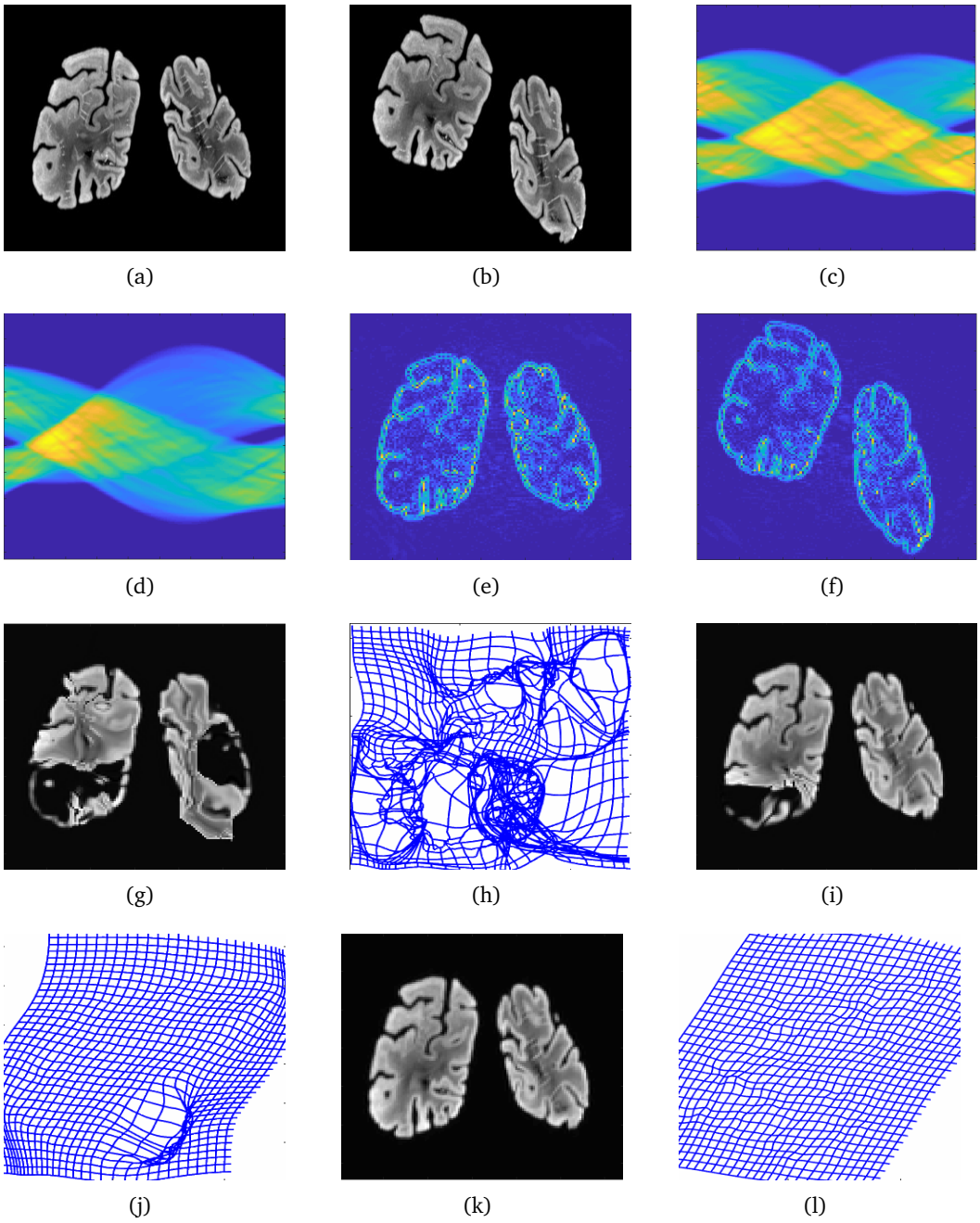

Fig. 5.2 Example of image registration results for mono-modal image registration by using our model. This figure illustrates the key role of the choice of the regularization parameters. (a) R: Corresponding image for S_R. (b) T: Corresponding image for S_T. (c) reference sinogram S_R. (d) template sinogram S_T. (e) RG : geometric information for S_R. (f) TG : geometric information for S_T. We tested the minimization problem (5.31) with $\lambda = 10$ and $\alpha = 20$ ((g) and (h)) or $\lambda = 150$ and $\alpha = 100$ ((i) and (j)) or $\lambda = 1000$ and $\alpha = 1000$ ((k) and (l)). The deformation is recovered by image registration, resulting in the images (g), (i) and (k).

Lemma 5.4.2 *Let $\mathcal{J}(\cdot)$ be the energy functional defined in $\mathcal{W}$ by*

$$\mathcal{J}(\boldsymbol{u}) = \int_{\Omega} f(x, \boldsymbol{u}, \nabla \boldsymbol{u}, \nabla^2 \boldsymbol{u}) dx, \tag{5.32}$$

where

$$f(x, \boldsymbol{u}, \nabla \boldsymbol{u}, \nabla^2 \boldsymbol{u}) = \tfrac{1}{2}|TG(\boldsymbol{u}) - RG|^2 + \frac{\lambda}{2}|\nabla \boldsymbol{u}|^2 + \frac{\alpha}{2}|\nabla^2 \boldsymbol{u}|^2. \tag{5.33}$$

Then, $\mathcal{J}(\cdot)$ is coercive and weakly lower semi-continuous (wlsc) in $\mathcal{W}$.

PROOF 5 *We have*

$$\mathcal{J}(\boldsymbol{u}) = \int_\Omega \left(\tfrac{1}{2}|TG(\boldsymbol{u}) - RG|^2 + \frac{\lambda}{2}|\nabla \boldsymbol{u}|^2 + \frac{\alpha}{2}|\nabla^2 \boldsymbol{u}|^2 \right) dx.$$

Using the positivity of $\int_\Omega \frac{1}{2}|TG(\boldsymbol{u}) - RG|^2 dx$, we obtain

$$\mathcal{J}(\boldsymbol{u}) \geq \frac{\min(\lambda, \alpha)}{2} \int_\Omega |\nabla \boldsymbol{u}|^2 + |\nabla^2 \boldsymbol{u}|^2 dx.$$

By using Poincaré's inequality, we show that

$$\|\boldsymbol{u}\|_{\mathcal{W}} = \left(\|\nabla \boldsymbol{u}\|_2^2 + \|\nabla^2 \boldsymbol{u}\|_2^2 \right)^{\frac{1}{2}},$$

is a norm on the space $\mathcal{W}$. Thus, we obtain

$$\mathcal{J}(\boldsymbol{u}) \geq \tfrac{1}{2} \min(\lambda, \alpha) \|\boldsymbol{u}\|_{\mathcal{W}}^2.$$

which directly gives the coercivity of $\mathcal{J}(\cdot)$.

For the wlsc of $\mathcal{J}(\cdot)$, we now check that the function $f(\cdot)$ fulfils the assumptions in Lemma 5.4.1. Since the images RG and TG are assumed continuous almost everywhere on their domain then $f(\cdot)$ is Carathéodory function. In addition, it is easy to check that $f(x, \boldsymbol{u}, \nabla \boldsymbol{u}, \nabla^2 \boldsymbol{u})$ is convex with respect to $\nabla^2 \boldsymbol{u}$, clearly implying that it is quasi-convex. Moreover, as we have assumed earlier that $|TG(\boldsymbol{u})|$ and $|RG|$ are bounded almost everywhere by a constant $c > 0$, we deduce that

$$\tfrac{1}{2}|TG(\boldsymbol{u}) - RG|^2 \leq \tfrac{1}{2} \left(|TG(\boldsymbol{u})| + |RG| \right)^2 \leq 2c^2.$$

Then, we get

$$0 \leq f(x, \boldsymbol{u}, \nabla \boldsymbol{u}, \nabla^2 \boldsymbol{u}) = \tfrac{1}{2}|TG(\boldsymbol{u}) - RG|^2 + \frac{\lambda}{2}|\nabla \boldsymbol{u}|^2 + \frac{\alpha}{2}|\nabla^2 \boldsymbol{u}|^2,$$

which implies

$$0 \leq f(x, \boldsymbol{u}, \nabla \boldsymbol{u}, \nabla^2 \boldsymbol{u}) \leq 2c^2 + \frac{\lambda}{2}|\nabla \boldsymbol{u}|^2 + \frac{\alpha}{2}|\nabla^2 \boldsymbol{u}|^2.$$

Consequently, the function $f(\cdot)$ fulfills the third condition of Lemma 5.4.1 with $a(x) = 2c^2 \in L^1(\Omega)$ and $C = \frac{1}{2}\max(\lambda, \alpha)$. Finally, we deduce that the energy $\mathcal{J}(\cdot)$ is weakly lower semi-continuous in $\mathcal{W}$.

Theorem 5 *The minimization problem (5.31) admits at least one solution in the space $\mathcal{W}$.*

PROOF 6 *Let $(\boldsymbol{u}_n)_{n\in\mathbb{N}} \subset \mathcal{W}$ of $\mathcal{J}(\cdot)$ be a minimizing sequence, i.e.,*

$$\mathcal{J}(\boldsymbol{u}_n) \underset{n\to+\infty}{\longrightarrow} \min_{\boldsymbol{u}\in\mathcal{W}} \mathcal{J}(\boldsymbol{u}).$$

The coercivity of $\mathcal{J}(\cdot)$ implies that $(\boldsymbol{u}_n)_{n\in\mathbb{N}}$ is uniformly bounded in $\mathcal{W}$. Thus, the boundedness of $(\boldsymbol{u}_n)_{n\in\mathbb{N}}$ guarantees the existence of a subsequence, still denoted $(\boldsymbol{u}_n)_{n\in\mathbb{N}}$ such that $\boldsymbol{u}_n \underset{n\to+\infty}{\rightharpoonup} \boldsymbol{u}$ in $\mathcal{W}$. By using the wlsc of $\mathcal{J}(\cdot)$ proved in Lemma 5.4.1, i.e., $\mathcal{J}(\boldsymbol{u}) \leq \underset{n\longrightarrow+\infty}{lim}\, \mathcal{J}(\boldsymbol{u}_n) = \min_{\boldsymbol{u}\in\mathcal{W}} \mathcal{J}(\boldsymbol{u})$, we show that the limit $\boldsymbol{u}$ is a minimizer of $\mathcal{J}(\cdot)$.

5.5 Numerical experiments

The goal of this section is to prove that topological gradient approach of a high-order operator is able to define a fidelity measure for image registration. First, we give an algorithm that consists of inserting small cracks in regions where the topological gradient $g(x_0)$ is smaller than a given threshold $\xi < 0$. These regions represent the geometric information (edges, thin structures) of the image. Then, we give the Gauss-Newton algorithm which is well adapted for a non-linear least squares optimization problem. Finally, we give the multilevel image registration algorithm.

5.5.1 Step one: Geometric information from the tomographic data

Before going to the numerical study of problem (7.2), let us remind the algorithm of the topological gradient for detecting geometric information from image (i.e., how to obtain TG and RG).

In this algorithm, we have to solve one direct and one adjoint PDE problem in order to calculate the topological gradient expression. These problems are linear which leads to obtain a linear system: $Ax = B$ based on the finite element method. This

provided the operator R^*R is assembled. Where R is the system matrix defining the discrete Radon operator, defined by:

$$R(i,j) = \begin{cases} 1 & \text{if the projection i crosses the position j of the object,} \\ 0 & \text{otherwise,} \end{cases}$$

and R^* is the dual discrete operator of R ($R^* = R$). According to the properties of the operators defined in the direct and adjoint PDE problem, we show that A is a positive definite symmetric matrix. For the computational cost of the topological gradient method, we solve this linear system with a preconditioned conjugate gradient method which requires $O(n^2 log(n))$ operations for an object with $n \times n$ pixels.

Algorithm 3 T-G's approach to the reconstruction of the image and detection of its geometric information.

- Initalization: $\lambda = \lambda_0$, $\alpha_\varepsilon = \alpha_0$ and $\beta_\varepsilon = \beta_0$.

A) Edges detection:

- Calculation of u_0 and v_0 by solving the direct (5.19) and the adjoint (5.21) problems.
- Determination of the edges set I_1 defined by

$$I_1 = \{x_0 \in \Omega \text{ such that } G(x_0) < \xi_1 < 0\},$$

where ξ_1 is a given negative threshold and $G(x_0)$ is the topological gradient defined in (5.20) .

B) thin structures detection:

- Calculation of u_0 and v_0 by solving the direct (5.25) and the adjoint (5.28) problems.
- Calculation of the topological gradient (5.20) for detecting edges.
- Determination of the thin structures set I_2 defined by

$$I_2 = \{x_0 \in \Omega \text{ such that } g(x_0) < \xi_2 < 0\},$$

where ξ_2 is a given negative threshold and $g(x_0)$ is the topological gradient defined in (5.30).

C) Geometric structures information:

- The geometric structures information is defined by the following set:

$$\omega = I_1 \cup I_2$$

5.5.2 Step Two: Image registration process

Gauss-Newton method

Our model is a highly non-linear least squares problem, and its numerical solution is a non-trivial task. For this purpose, we propose a Gauss-Newton method for solving the minimization problem by replacing the original non-linear system with a linear one. Indeed, the Gauss-Newton scheme is as follows: Starting from an initial guess δU, we compute the gradient $G_{\mathcal{J}}$ at each step. Then, we improve this guess by an update δU which is solution of the linear system:

$$\mathcal{H}\delta U = -G_{\mathcal{J}}. \tag{5.34}$$

The process is repeated until convergence, i.e., $\|\delta U - \delta U_{old}\| \leq \varepsilon$, where ε is a given threshold. We note that $\mathcal{H}$ is an approximated Hessian which is symmetric and positive definite.

In order to obtain the descretization formulation for the model (5.31), we use finite differences on a unit square domain $\Omega =]0,1[^2$. In implementation, we employ a nodal grid and define a discretized square domain by the uniform grid

$$\left\{\mathbf{x}^{i,j} = (x_1^i, x_2^j) = (ih, jh),\ 0 \leq i,j \leq n\right\},$$

where $h = \frac{1}{n}$. We discretize the uniform displacement field $\mathbf{u}$ on the nodal grid $\mathbf{x}^{i,j}$ and $\mathbf{u}^{i,j}$, namely $\mathbf{u}^{i,j} = (u_1^{i,j}, u_2^{i,j}) = (u_1(x_1^i, x_2^j), u_2(x_1^i, x_2^j))$. According to the lexicographical ordering, we reshape the matrices into two long vectors of dimension $\mathbb{R}^{2(n+1)^2 \times 1}$. Then, we approximate the first-order and second-order regularization terms by using the forward difference, central difference, mid-point rule and Dirichlet boundary conditions. For more information and details, the reader is referred to [Laj+22b; ZTC19b]

Algorithm 4 Gauss-Newton method by using Armijo line search for image registration: $U \leftarrow \text{GNIR}(U_0)$.

Start with an initial guess $U \longleftarrow U_0$;
While not converged **do**

1. Evaluate $\mathcal{J}$, $G_{\mathcal{J}}$ and $\mathcal{H}$ at U
2. Solve the descent direction from the linear equation $\mathcal{H}\delta U = -G_{\mathcal{J}}$
3. Find a positive scalar step-size s using line search scheme
4. Update $U \longleftarrow U + s\delta U$

Multilevel technique

A major difficulty in numerical optimization is the non-convexity of the model. Constructing a numerical optimization algorithm that avoids being trapped in a local minimum is very important for solving a non-convex model. Here, we overcome these limitations by a multilevel technique, which assures the numerical solution serves as a perfect starting point and speeds up the registration process. Indeed, starting with the initial guess $U = 0$, the idea is to improve this guess by resizing the original images to a sequence of coarser ones where computations are cheap and register these smaller images (see Fig. 5.3). Then, starting from the coarsest level, we interpolate the update U to get a starting guess on next levels until the original resolution on the finest level is reached.

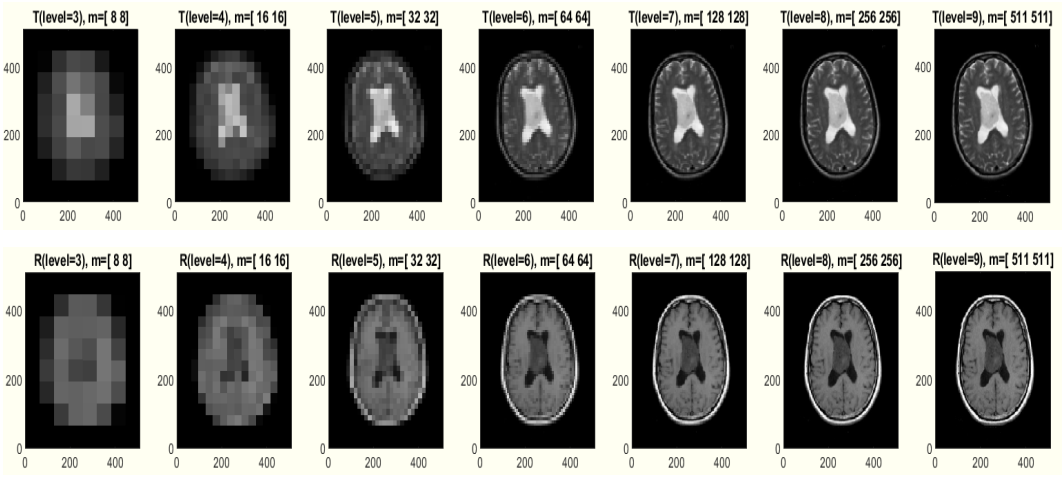

Fig. 5.3 Example of a multilevel representation of both images R and T of size 511×511.

Algorithm 5 Multilevel image registration: $U \leftarrow$ MLIR

Data: An initial guess U, minLevel and maxLevel from ML by computing a multilevel representation of both images.
Level = minLevel
while Level $\leq$ maxLevel **do**

1. $U_0 = U$
2. Solve the registration problem $U \leftarrow$ GNIR(U_0)
3. Level = next Level
4. Prolongate U to the finer grid: $U \longleftarrow$ prolongate(U)

5.6 Results and discussion

In the sequel, we present some examples of the performance of our model, the sensitivity to the noise in the sinogram, and assess the quality of the registration results of the model by using the following error measure:

$$\mathcal{E}_r = \frac{\|RG - TG(\varphi)\|_2^2}{\|RG - TG\|_2^2}, \tag{5.35}$$

where $TG(\varphi)$ represents the registered geometric information. The run time for the image registration process is given in Tab. 5.1. In the presented examples, all the images are of size 128×128. The algorithms were implemented in MATLAB R2021b running on a Laptop with Intel (R) core(TM) i5 processor, CPU at 2.50 GHz and 8GB RAM memory at 2133 MHz. Since our model is based on the Gauss-Newton method, a multilevel technique is used to accelerate the optimization process. The required run times show the speed of our model.

For each test, we present both images S_R and S_T which represent respectively the reference and the template sinogram, the correspondence images for S_R and S_T which are denoted respectively by R and T, the edges RG and TG which are used for defining our proposed image registration model, the registered image $T(\varphi)$ and the deformation $\varphi(\mathbf{u})(\mathbf{x}) = \mathbf{x} + \mathbf{u}(\mathbf{x})$.

Figure	5.4	5.5	5.6	5.7	5.9	5.10
Time (s)	13.617	12.173	10.384	11.907	13.094	12.957

Tab. 5.1 Run times for the image registration process.

In Fig. 5.4, we have a multi-modal images, the reference and the template images represent a cross section of the brain. Fig. 5.5 is an example of a mono-modal image registration with a non-parametric transformation. Clearly, we see that we have a perfect registered image with a relative error $\mathcal{E}_r = 0.08$.

In Figs. 5.6, 5.7 and 5.8 we display some examples of synthetic images for a mono-modal images registration. In all cases, we have the same object in reference and template images but each template has different deformation. To evaluate our model, we took different rotation's degrees. Then, we can show that our model performs well for the degrees that are less than 70°. In Fig. 5.9 and Fig. 5.10, to test the sensitivity of our model to the noise, we add white Gaussian noise, often abbreviated AWGN, in sinogram with variance $N = 0.001$ and $N = 0.6$, respectively. We show that our model performs well. Moreover, we tested our model with different noise

level for the figure 5.10 and by cheking the errors in table 5.2, we could show that our proposed model performs well in the presence of noise.

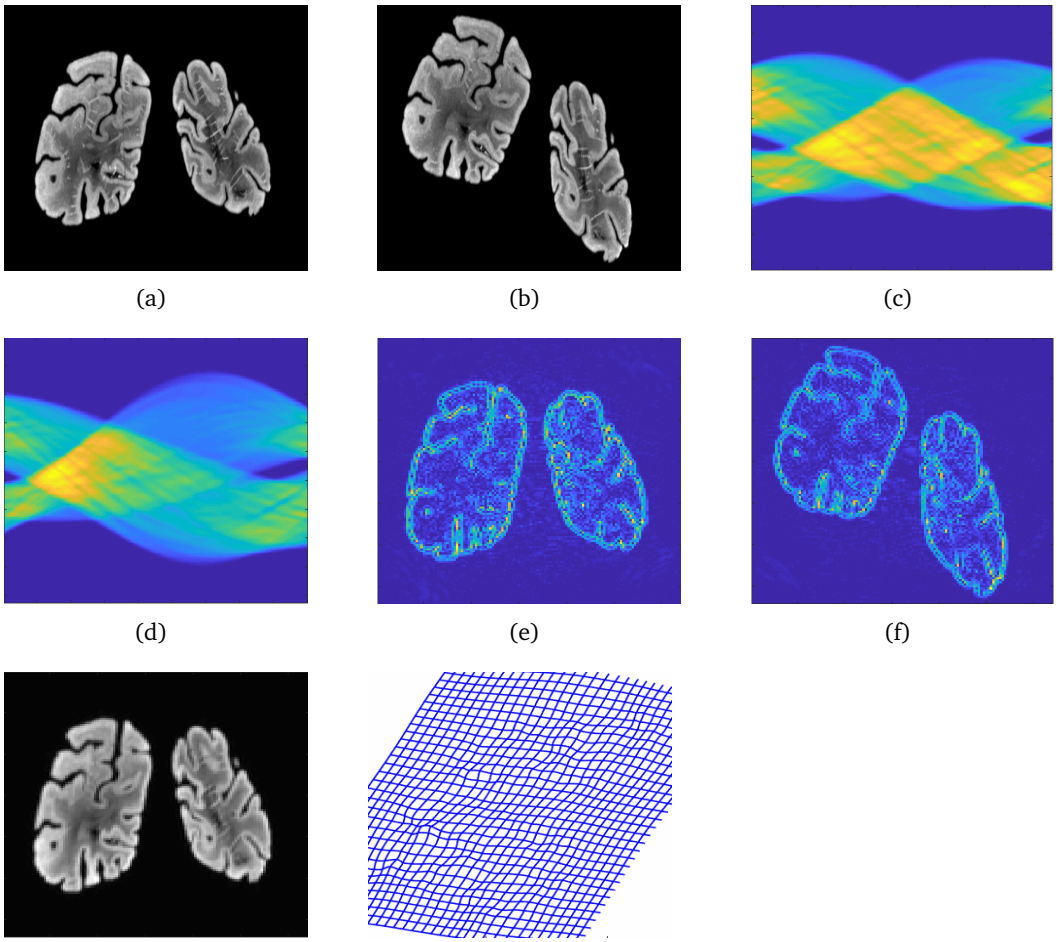

(a) (b) (c)

(d) (e) (f)

(g) (h)

Fig. 5.5 Example of a mono-modal image registration by using our model. (a) R: Corresponding image for S_R. (b) T: Corresponding image for S_T. (c) reference sinogram S_R. (d) template sinogram S_T. (e) RG : geometric information for S_R. (f) TG : geometric information for S_T. (g) registered image $T(\varphi)$, $\mathcal{E}_r = 0.08$. (h) The deformation $\varphi(x) = x + \mathbf{u}(x)$.

5.7 Conclusion

We have used the topological gradient approach for a tomographic reconstruction that uses the first- and second-order discontinuities. We have shown the advantage of that T-G which uses only the first-order discontinuities for the detection of geometric information. A new method for image registration with information geometric detection via the topological gradient method has been presented in this work. The results obtained for the detection and the registration are very promising.

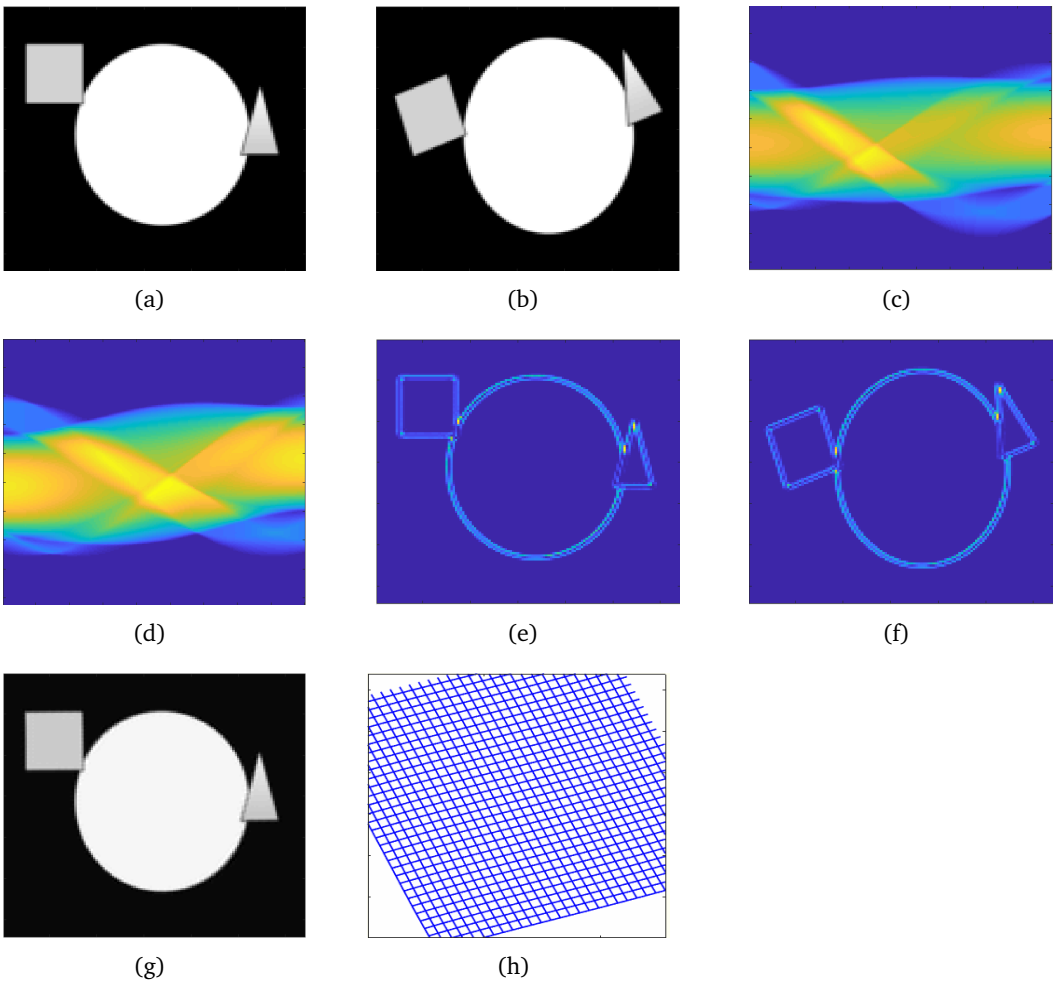

Fig. 5.6 Example of a parametric mono-modal image registration by using our model. The geometric transformation between the reference and the template images is in the form of a 30 degree rotation. (a) R: Corresponding image for S_R. (b) T: Corresponding image for S_T. (c) reference sinogram S_R. (d) template sinogram S_T. (e) RG : geometric information for S_R. (f) TG : geometric information for S_T. (g) registered image $T(\varphi)$, $\mathcal{E}_r = 0.04$. (h) The deformation $\varphi(x) = x + \mathbf{u}(x)$.

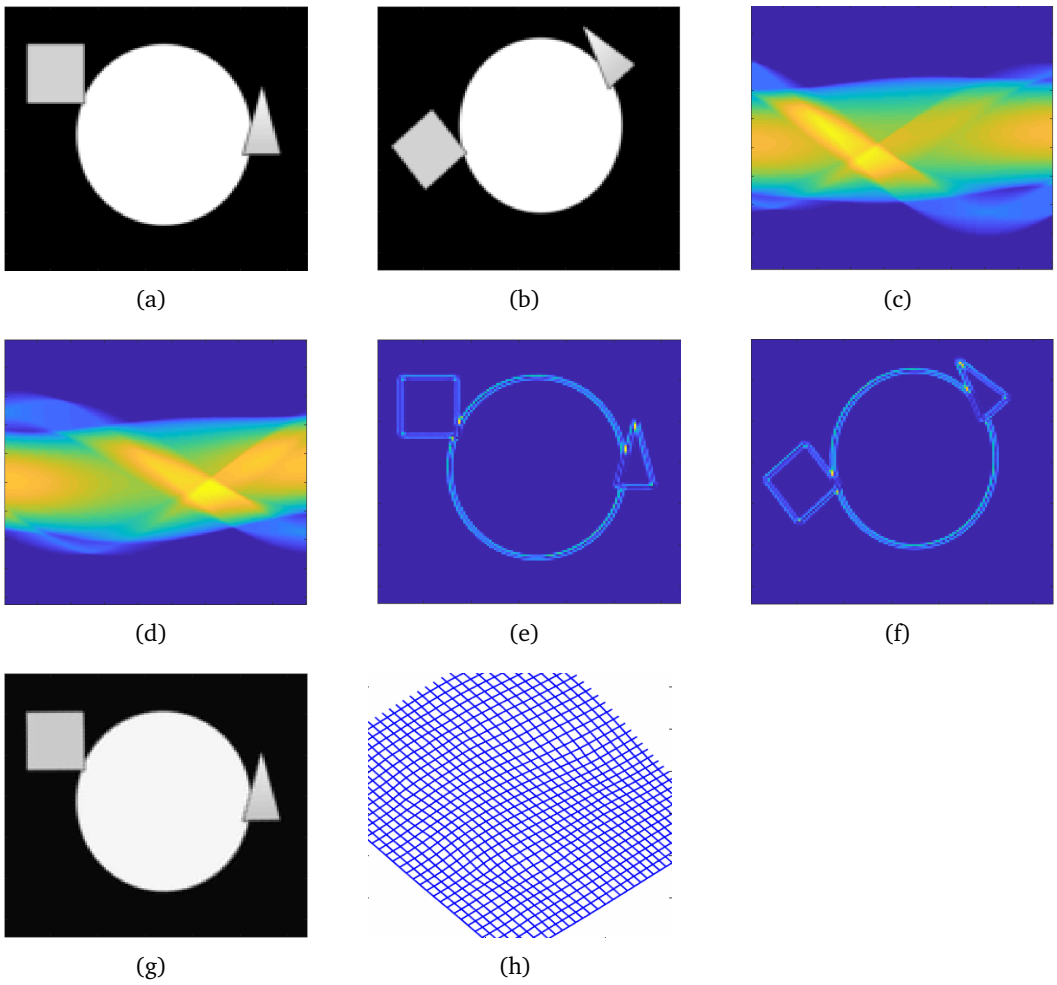

Fig. 5.7 Example of a parametric mono-modal image registration by using our model. The geometric transformation between the reference and the template images is in the form of a 45 degree rotation. (a) R: Corresponding image for S_R. (b) T: Corresponding image for S_T. (c) reference sinogram S_R. (d) template sinogram S_T. (e) RG : geometric information for S_R. (f) TG : geometric information for S_T. (g) registered image $T(\varphi)$, $\mathcal{E}_r = 0.09$. (h) The deformation $\varphi(x) = x + \mathbf{u}(x)$.

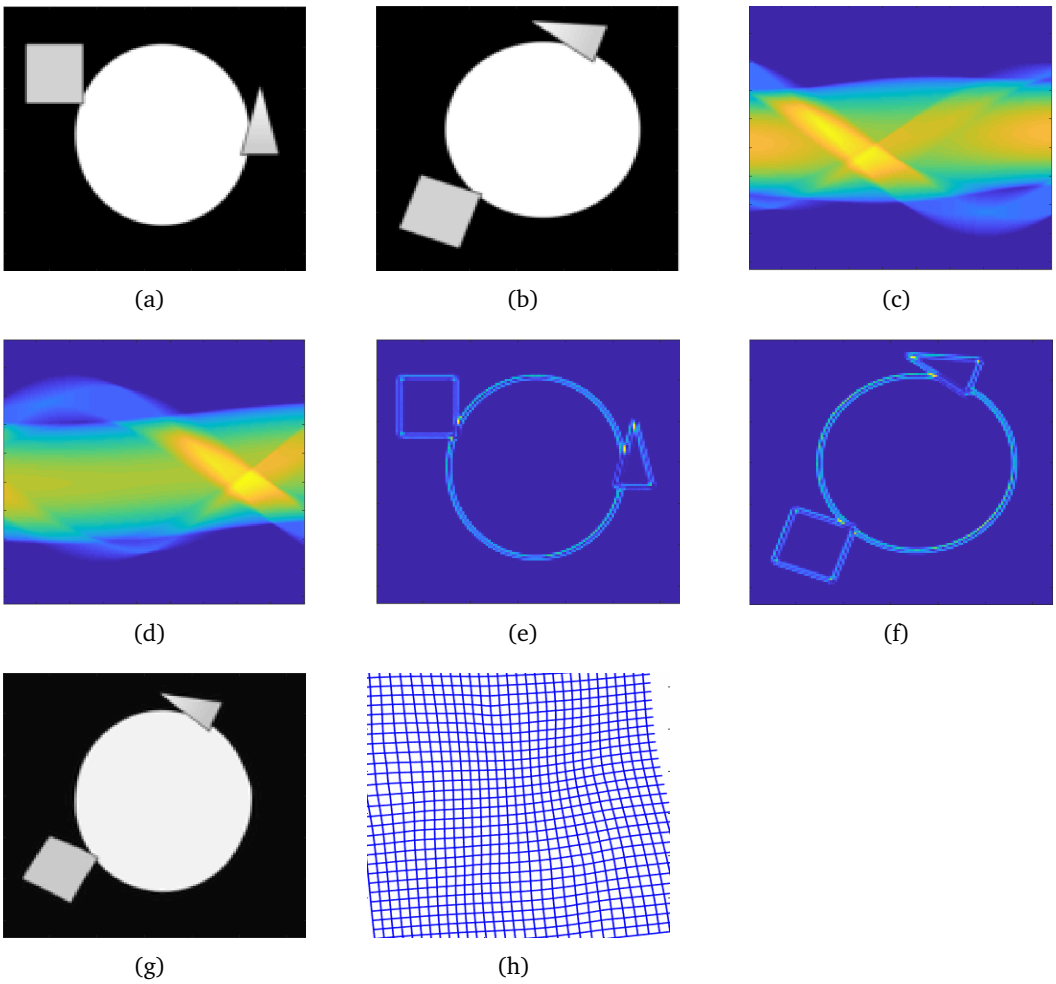

Fig. 5.8 Example of a parametric mono-modal image registration by using our model. The geometric transformation between the reference and the template images is in the form of a 70 degree rotation. (a) R: Corresponding image for S_R. (b) T: Corresponding image for S_T. (c) reference sinogram S_R. (d) template sinogram S_T. (e) RG : geometric information for S_R. (f) TG : geometric information for S_T. (g) registered image $T(\varphi)$. (h) The deformation $\varphi(x) = x + \mathbf{u}(x)$.

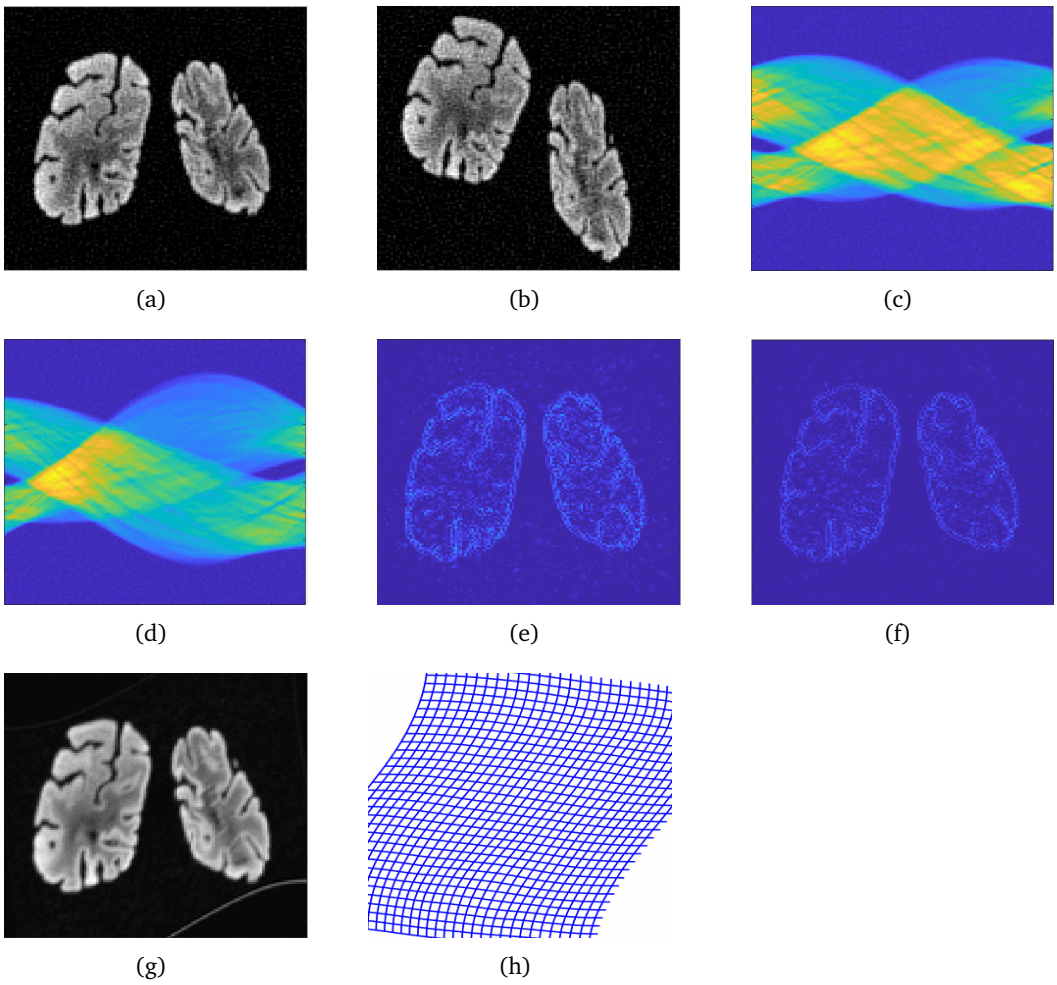

Fig. 5.9 Example of a mono-modal image registration by using our model in the case where we have noise in sinograms. We consider noisy sinograms S_R and S_T whith an additive white Gaussian noise, with variance $N = 0.001$ and PSNR=10.56. (a) R: Corresponding image for S_R. (b) T: Corresponding image for S_T. (c) reference sinogram S_R. (d) template sinogram S_T. (e) RG : geometric information for S_R. (f) TG : geometric information for S_T. (g) registered image $T(\varphi)$, $\mathcal{E}_r = 0.22$. (h) The deformation $\varphi(x) = x + \mathbf{u}(x)$.

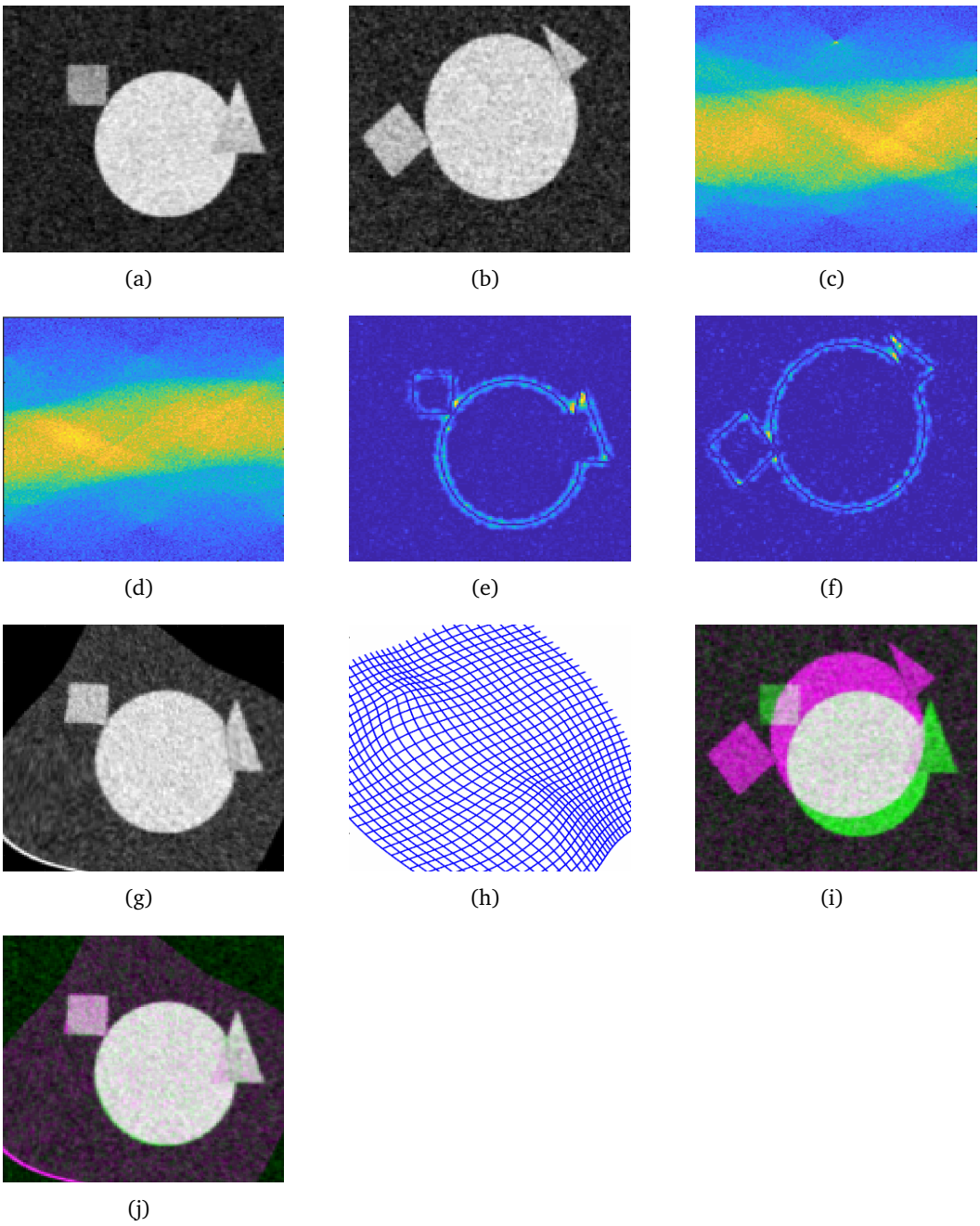

Fig. 5.10 Example of mono-modal images registration by using our model in the case where we have noise in sinograms. We consider noisy sinograms S_R and S_T whith an additive white Gaussian noise, with variance N = 0.6. (a) R: Corresponding image for S_R. (b) T:Correspondence image for S_T. (c) reference sinogram S_R. (d) template sinogram S_T. (e) RG : geometric information for S_R. (f) TG : geometric information for S_T. (g) registered image $T(\varphi)$, $\mathcal{E}_r = 0.11$. (h) The deformation $\varphi(x) = x + \mathbf{u}(x)$. (i) R and T before the registration. (j) R and T after the registration.

Conclusion and perspectives

6

In this thesis, we have focused on the problem of deformable image registration. We have provided an overview of recent developments for image registration based on geometric information. Indeed, one of the main objectives of this thesis is the theoretical and numerical analysis of the similarity term of image registration methods. Three main aspects have been addressed: The transferability of results and techniques of geometric information detection by high-order operators or by variational computation in the domain of image registration. The integration of Blake-Zisserman energy in the field of image registration using deep learning to create neural networks that allow the prediction of geometric information detection and that allows, also, necessary deformation for the registration process, and theoretical analysis of the detection of important features via the topological gradient method. The study of existence of solutions of the proposed models. Numerical results were presented to illustrate the effectiveness and efficiency of the proposed models. Our major contribution consists of the following three developments:

In the first chapter, we provided a general introduction to digital images, with a focus on geometric information such as edges and thin structures. We also discussed classical problems in image processing, including restoration, segmentation, and registration.

In the second chapter, we presented the basic concepts of image registration, including the different types of transformations commonly used to align images. We also discussed challenges and limitations of image registration, and practical approaches to addressing them. Besides, we reviewed optimization algorithms commonly used to find optimal transformation parameters.

In the third chapter, we have proposed to use geometric information from the images to build a robust and efficient similarity term for a deformable registration model for multi-modality images. To extract this information, we employ the Blake-Zisserman's energy. This energy is well suited for detecting discontinuities at different scales. This has an advantage, for example when the image contains high-order features such as thin structures (points, filaments) that are not detectable by first-order derivatives. We gave a theoretical analysis of the proposed model by proving the existence of a solution. In addition, we gave a reliable and efficient numerical resolution of the image registration model based on the Gauss-Newton algorithm

and multilevel technique to accelerate the numerical computations for the solution of this model. As expected, experimental tests confirm that our proposed fidelity measure solves the problem of weak edges and second-order discontinuities with acceptable registration results.

In the fourth chapter, we have developed and presented an efficient unsupervised deep learning-based multilevel image registration approach benefiting from geometric information (edges and thin structures) extracted from the images using the Blake-Zisserman's energy, i.e., the image edges, during the training. We have proposed a new loss function defined by the Blake-Zisserman's function that can be used to achieve detection quality of geometric information based on deep learning without labeled data. Then, we used this geometric information in order to define a novel deep neural network architecture that performs multilevel image registration

In the fifth chapter, we have proposed to use the topological gradient method for image registration. A new variational model for image registration from tomographic data is given: first, a computation of the topological gradient associated to a second-order derivative in the cost function is given. Second, we have used the found topological gradient to detect the edges and thin structures for both images from X-ray tomographic data. Then, we use this geometric information in order to define a fidelity measure in the image registration process. In addition, we have shown the advantage of the found topological gradient which uses the first-order discontinuities for detection of geometric information. Furthermore, we have presented numerical results carried out on different images and which are obtained using the proposed approach. We also presented numerical results which illustrate the sensitivity of our model to additive white Gaussian noise, often abbreviated AWGN, in sinogram with different variances.

Bibliography

[Ado84] G Adomian. “A new approach to nonlinear partial differential equations”. In: *Journal of Mathematical Analysis and Applications* 102.2 (1984), pp. 420–434 (cit. on p. 79).

[AD04] Srinath Akula and Veerabhadram Devisetty. “Image based registration and authentication system”. In: *Proceedings of Midwest Instruction and Computing Symposium*. Vol. 4. 2004, p. 5 (cit. on pp. 23, 67).

[AB20] Amir Alavi and Ziv Bar-Joseph. “Iterative point set registration for aligning scRNA-seq data”. In: *PLoS Computational Biology* 16.10 (2020), e1007939 (cit. on pp. 23, 43, 91).

[AFM01] Luigi Ambrosio, Loris Faina, and Riccardo March. “Variational approximation of a second order free discontinuity problem in computer vision”. In: *SIAM Journal on Mathematical Analysis* 32.6 (2001), pp. 1171–1197 (cit. on p. 73).

[Ams03] Samuel Amstutz. “Aspects théoriques et numériques en optimisation de forme topologique”. PhD thesis. Toulouse, INSA, 2003 (cit. on p. 12).

[AF15] Samuel Amstutz and Jérôme Fehrenbach. “Edge detection using topological gradients: a scale-space approach”. In: *Journal of Mathematical Imaging and Vision* 52.2 (2015), pp. 249–266 (cit. on p. 97).

[AHM05] Samuel Amstutz, Imene Horchani, and Mohamed Masmoudi. “Crack detection by the topological gradient method”. In: *Control and Cybernetics* 34 (2005), pp. 81–101 (cit. on p. 97).

[ANV14] Samuel Amstutz, Antonio André Novotny, and Nicolas Van Goethem. “Topological sensitivity analysis for elliptic differential operators of order 2m”. In: *Journal of Differential Equations* 256.4 (2014), pp. 1735–1770 (cit. on pp. 72, 96, 97).

[AKR97] Steven Armstrong, Anil C Kokaram, and Peter JW Rayner. “Non-linear interpolation of missing image data using Min-Max functions”. In: *Proceedings of IEEE International Conference on Nonlinear Signal and Image Processing (NSIP)*. Citeseer. 1997 (cit. on p. 1).

[AD14] Gilles Aubert and Audric Drogoul. “A topological gradient based model for the detection of fine structures in 2D images”. In: *ESAIM: Control, Optimisation and Calculus of Variations* (2014) (cit. on p. 13).

[AD15] Gilles Aubert and Audric Drogoul. “Topological gradient for a fourth order operator used in image analysis”. In: *ESAIM: Control, Optimisation and Calculus of Variations* 21.4 (2015), pp. 1120–1149 (cit. on pp. 96, 97, 143–145).

[AKA06] Gilles Aubert, Pierre Kornprobst, and Giles Aubert. *Mathematical Problems in Image Processing: Partial Differential Equations and the Calculus of Variations*. Vol. 147. 2006 (cit. on p. 1).

[Aur09] Didier Auroux. "From restoration by topological gradient to medical image segmentation via an asymptotic expansion". In: *Mathematical and Computer Modelling* 49.11-12 (2009), pp. 2191–2205 (cit. on pp. 87, 97).

[AJR10] Didier Auroux, L. Jaafar-Belaid, and Badreddine Rjaibi. "Application of the topological gradient method to tomography". In: *Revue Africaine de la Recherche en Informatique et Mathématiques Appliquées* 13 (2010), pp. 91–104 (cit. on pp. 87, 95, 97).

[AM09] Didier Auroux and Mohamed Masmoudi. "Image processing by topological asymptotic expansion". In: *Journal of Mathematical Imaging and Vision* 33.2 (2009), pp. 122–134 (cit. on p. 95).

[Ava+08] Brian B. Avants, Charles L. Epstein, Murray Grossman, and James C. Gee. "Symmetric diffeomorphic image registration with cross-correlation: evaluating automated labeling of elderly and neurodegenerative brain". In: *Medical Image Analysis* 12.1 (2008), pp. 26–41 (cit. on p. 69).

[Bal+18] Guha Balakrishnan, Amy Zhao, Mert R. Sabuncu, John Guttag, and Adrian V. Dalca. "An unsupervised learning model for deformable medical image registration". In: *Proceedings of the IEEE Conference on Computer Vision and Pattern Recognition*. 2018, pp. 9252–9260 (cit. on pp. 65, 69).

[Bal+19] Guha Balakrishnan, Amy Zhao, Mert R. Sabuncu, John Guttag, and Adrian V. Dalca. "VoxelMorph: a learning framework for deformable medical image registration". In: *IEEE Transactions on Medical Imaging* 38.8 (2019), pp. 1788–1800 (cit. on pp. 65, 68, 69).

[BB00] Samit Basu and Yoram Bresler. "O (n/sup 2/log/sub 2/n) filtered backprojection reconstruction algorithm for tomography". In: *IEEE Transactions on Image Processing* 9.10 (2000), pp. 1760–1773 (cit. on p. 94).

[Bel+06] Lamia Jaafar Belaid, Mohamed Jaoua, Mohamed Masmoudi, and Lassaad Siala. "Image restoration and edge detection by topological asymptotic expansion". In: *Comptes Rendus Mathematique* 342.5 (2006), pp. 313–318 (cit. on p. 97).

[BCS20] Martin Beroiz, Juan B. Cabral, and Bruno Sanchez. "Astroalign: A Python module for astronomical image registration". In: *Astronomy and Computing* 32 (2020), p. 100384 (cit. on pp. 23, 43, 67, 91).

[BZ87] Andrew Blake and Andrew Zisserman. *Visual Reconstruction*. MIT press, 1987 (cit. on pp. 41, 46, 72).

[Blo+97] Peter Blomgren, Tony F. Chan, Pep Mulet, and Chak-Kuen Wong. "Total variation image restoration: numerical methods and extensions". In: *Proceedings of International Conference on Image Processing* 3 (1997), pp. 384–387 (cit. on p. 95).

[BM15] Alexander de Brebisson and Giovanni Montana. “Deep neural networks for anatomical brain segmentation”. In: *Proceedings of the IEEE Conference on Computer Vision and Pattern Recognition Workshops*. 2015, pp. 20–28 (cit. on p. 10).

[BMR13] Martin Burger, Jan Modersitzki, and Lars Ruthotto. “A hyperelastic regularization energy for image registration”. In: *SIAM Journal on Scientific Computing* 35.1 (2013), B132–B148 (cit. on pp. 31, 44, 75).

[BF95] James V Burke and Michael C Ferris. “A Gauss—Newton method for convex composite optimization”. In: *Mathematical Programming* 71.2 (1995), pp. 179–194 (cit. on p. 24).

[Cac+01] Pascal Cachier, Jean-Francois Mangin, Xavier Pennec, et al. “Multisubject non-rigid registration of brain MRI using intensity and geometric features”. In: *International Conference on Medical Image Computing and Computer-Assisted Intervention*. Springer. 2001, pp. 734–742 (cit. on p. 26).

[Cao+18] Xiaohuan Cao, Jianhuan Yang, Li Wang, et al. “Deep learning based inter-modality image registration supervised by intra-modality similarity”. In: *International Workshop on Machine Learning in Medical Imaging*. Springer, 2018, pp. 55–63 (cit. on pp. 65, 69).

[Cha99] Antonin Chambolle. “Finite-differences discretizations of the Mumford-Shah functional”. In: *ESAIM: Mathematical Modelling and Numerical Analysis* 33.2 (1999), pp. 261–288 (cit. on p. 72).

[CMM00] Tony Chan, Antonio Marquina, and Pep Mulet. “High-order total variation-based image restoration”. In: *SIAM Journal on Scientific Computing* 22.2 (2000), pp. 503–516 (cit. on p. 95).

[CLM19] Ke Chen, Lok Ming Lui, and Jan Modersitzki. “Image and surface registration”. In: *Handbook of Numerical Analysis*. Vol. 20. Elsevier, 2019, pp. 579–611 (cit. on p. 53).

[CC] Noppadol Chumchob and Ke Chen. “A robust affine image registration method”. en. In: (), p. 25 (cit. on pp. 44, 56).

[Col+95a] André Collignon, Dirk Vandermeulen, Paul Suetens, and Guy Marchal. “3D multi-modality medical image registration using feature space clustering”. In: *International Conference on Computer Vision, Virtual Reality, and Robotics in Medicine*. 1995, pp. 195–204 (cit. on p. 34).

[Col+95b] André Collignon, Dirk Vandermeulen, Paul Suetens, and Guy Marchal. “3D multi-modality medical image registration using feature space clustering”. In: *International Conference on Computer Vision, Virtual Reality, and Robotics in Medicine* 9 (1995), pp. 195–204 (cit. on p. 45).

[Dai03] Yu-Hong Dai. “A family of hybrid conjugate gradient methods for unconstrained optimization”. In: *Mathematics of Computation* 72.243 (2003), pp. 1317–1328 (cit. on p. 24).

[DPB96] Christos Davatzikos, Jerry L Prince, and R Nick Bryan. “Image registration based on boundary mapping”. In: *IEEE Transactions on Medical Imaging* 15.1 (1996), pp. 112–115 (cit. on p. 25).

[Dea07] Stanley R. Deans. *The Radon transform and some of its applications*. Courier Corporation, 2007 (cit. on p. 94).

[DM77] John E Dennis Jr and Jorge J Moré. “Quasi-Newton methods, motivation and theory”. In: *SIAM Review* 19.1 (1977), pp. 46–89 (cit. on p. 24).

[DG01] Lijun Ding and Ardeshir Goshtasby. “On the Canny edge detector”. In: *Pattern Recognition* 34.3 (2001), pp. 721–725 (cit. on p. 13).

[Dro14] Audric Drogoul. “Numerical analysis of the topological gradient method for fourth order models and applications to the detection of fine structures in imaging”. In: *SIAM Journal on Imaging Sciences* 7.4 (2014), pp. 2700–2731 (cit. on pp. 10, 96, 97).

[DR06] Marc Droske and Wolfgang Ring. “A Mumford–Shah level-set approach for geometric image registration”. In: *SIAM Journal on Applied Mathematics* 66.6 (2006), pp. 2127–2148 (cit. on pp. 36, 41, 46, 72).

[DR04] Marc Droske and Martin Rumpf. “A variational approach to nonrigid morphological image registration”. In: *SIAM Journal on Applied Mathematics* 64.2 (2004), pp. 668–687 (cit. on pp. 31, 75).

[EL06] Adrian N Evans and Xin U Liu. “A morphological gradient approach to color edge detection”. In: *IEEE Transactions on Image Processing* 15.6 (2006), pp. 1454–1463 (cit. on p. 13).

[FM02a] Bernd Fischer and Jan Modersitzki. “Fast diffusion registration”. In: *Contemporary Mathematics* 313 (2002), pp. 117–128 (cit. on pp. 31, 43, 44, 93).

[FM02b] Bernd Fischer and Jan Modersitzki. “Fast diffusion registration”. In: *Contemporary Mathematics* 313 (2002), pp. 117–128 (cit. on p. 75).

[GG84] Stuart Geman and Donald Geman. “Stochastic relaxation, Gibbs distributions, and the Bayesian restoration of images”. In: *IEEE Transactions on Pattern Analysis and Machine Intelligence* 6 (1984), pp. 721–741 (cit. on p. 1).

[Gig+11] Fabian Gigengack, Lars Ruthotto, Martin Burger, et al. “Motion correction in dual gated cardiac PET using mass-preserving image registration”. In: *IEEE Transactions on Medical Imaging* 31.3 (2011), pp. 698–712 (cit. on pp. 24, 43, 92).

[Gos05] Arthur Ardeshir Goshtasby. *2-D and 3-D Image Registration: For Medical, Remote Sensing, and Industrial Applications*. John Wiley & Sons, 2005 (cit. on pp. 23, 43, 67, 91).

[GM13] Samta Gupta and Susmita Ghosh Mazumdar. “Sobel edge detection algorithm”. In: *International Journal of Computer Science and Management Research* 2.2 (2013), pp. 1578–1583 (cit. on p. 13).

[HM06] Eldad Haber and Jan Modersitzki. “Intensity gradient based registration and fusion of multi-modal images”. In: *International Conference on Medical Image Computing and Computer-Assisted Intervention*. 2006, pp. 726–733 (cit. on pp. 35, 45).

[HM04] Eldad Haber and Jan Modersitzki. “Numerical methods for volume preserving image registration”. In: *Inverse Problems* 20.5 (2004), p. 1621 (cit. on pp. 31, 44).

[Had53] Jacques Hadamard. *1923Lectures on Cauchy’s Problem in Linear Partial Differential Equations*. 1953 (cit. on p. 4).

[Hil+01] Derek LG Hill, Philipp G Batchelor, Mark Holden, and David J Hawkes. “Medical image registration”. In: *Physics in Medicine & Biology* 46.3 (2001), R1 (cit. on pp. 23, 67).

[Hod+14] Erlend Hodneland, Arvid Lundervold, Jarle Rørvik, and Antonella Z. Munthe-Kaas. “Normalized gradient fields for nonlinear motion correction of DCE-MRI time series”. In: *Computerized Medical Imaging and Graphics* 38.3 (2014), pp. 202–210 (cit. on pp. 34, 45, 93).

[Hoo+21] Andrew Hoopes, Malte Hoffmann, Bruce Fischl, John Guttag, and Adrian V. Dalca. “Hypermorph: Amortized hyperparameter learning for image registration”. In: *International Conference on Information Processing in Medical Imaging*. 2021, pp. 3–17 (cit. on pp. 65, 69).

[Hou+19] Hamdi Houichet, Anis Theljani, Badreddine Rjaibi, and Maher Moakher. “A nonstandard higher-order variational model for speckle noise removal and thin-structure detection”. In: *Journal of Mathematical Study* 52 (2019), pp. 394–424 (cit. on pp. 10, 93, 96, 97).

[Hu+14] Wenrui Hu, Yuan Xie, Lin Li, and Wensheng Zhang. “A total variation based nonrigid image registration by combining parametric and non-parametric transformation models”. In: *Neurocomputing* 144 (2014), pp. 222–237 (cit. on pp. 31, 44, 93).

[Hu+18a] Yipeng Hu, Marc Modat, Eli Gibson, et al. “Label-driven weakly-supervised learning for multimodal deformable image registration”. In: *2018 IEEE 15th International Symposium on Biomedical Imaging (ISBI 2018)*. IEEE, 2018, pp. 1070–1074 (cit. on pp. 65, 69).

[Hu+18b] Yipeng Hu, Marc Modat, Eli Gibson, et al. “Weakly-supervised convolutional neural networks for multimodal image registration”. In: *Medical Image Analysis* 49 (2018), pp. 1–13 (cit. on pp. 65, 69).

[JC02] Hans J Johnson and Gary E Christensen. “Consistent landmark and intensity-based image registration”. In: *IEEE Transactions on Medical Imaging* 21.5 (2002), pp. 450–461 (cit. on p. 26).

[KR14] Lars Konig and Jan Ruhaak. “A fast and accurate parallel algorithm for non-linear image registration using normalized gradient fields”. In: *2014 IEEE 11th International Symposium on Biomedical Imaging (ISBI)* 38 (2014), pp. 580–583 (cit. on pp. 34, 45, 93).

[KLV09] H Kunze, D La Torre, and ER Vrscay. “A generalized collage method based upon the Lax–Milgram functional for solving boundary value inverse problems”. In: *Nonlinear Analysis: Theory, Methods & Applications* 71.12 (2009), e1337–e1343 (cit. on p. 11).

[Laj+22a] Mohamed Lajili, Badreddine Rjaibi, Didier Auroux, and Maher Moakher. “Edge detection from X-ray tomographic data for geometric image registration”. In: *Mathematical Methods in the Applied Sciences* (2022) (cit. on pp. 20, 72, 87).

[Laj+22b] Mohamed Lajili, Badreddine Rjaibi, Anis Theljani, and Maher Moakher. “Edge sketches for multi-modal image registration based on Blake–Zisserman type energy”. In: *Computational and Applied Mathematics* 41.7 (2022), pp. 1–20 (cit. on pp. 19, 41, 66, 70, 72, 73, 79, 109).

[Laj+22c] Mohamed Lajili, Anis Theljani, Maher Moakher, and Badreddine Rjaibi. “Multimodal image registration based on geometric similarity term”. In: *African Conference on Research in Computer Science and Applied Mathematics*. 2022 (cit. on p. 37).

[LA99] Hava Lester and Simon R Arridge. “A survey of hierarchical non-linear medical image registration”. In: *Pattern Recognition* 32.1 (1999), pp. 129–149 (cit. on pp. 23, 67).

[Lew83] Robert M. Lewitt. “Reconstruction algorithms: transform methods”. In: *Proceedings of the IEEE* 71.3 (1983), pp. 390–408 (cit. on pp. 93, 94).

[Liu+19] Jun Liu, Gurpreet Singh, Subhi Al’Aref, et al. “Image registration in medical robotics and intelligent systems: fundamentals and applications”. In: *Advanced Intelligent Systems* 1.6 (2019), p. 1900048 (cit. on pp. 23, 67).

[Loe+09] Dirk Loeckx, Pieter Slagmolen, Frederik Maes, Dirk Vandermeulen, and Paul Suetens. “Nonrigid image registration using conditional mutual information”. In: *IEEE Transactions on Medical Imaging* 29.1 (2009), pp. 19–29 (cit. on pp. 35, 45).

[LSD15] Jonathan Long, Evan Shelhamer, and Trevor Darrell. “Fully convolutional networks for semantic segmentation”. In: *Proceedings of the IEEE conference on computer vision and pattern recognition*. 2015, pp. 3431–3440 (cit. on p. 68).

[Mae+97] Frederik Maes, Andre Collignon, Dirk Vandermeulen, Guy Marchal, and Paul Suetens. “Multimodality image registration by maximization of mutual information”. In: *IEEE Transactions on Medical Imaging* 16.2 (1997), pp. 187–198 (cit. on pp. 34, 45, 69, 93).

[MV98] JB Antoine Maintz and Max A Viergever. “A survey of medical image registration”. In: *Medical Image Analysis* 2.1 (1998), pp. 1–36 (cit. on pp. 23, 67).

[Mäk+03] Timo Mäkelä et al. *Data registration and fusion for cardiac applications*. Helsinki University of Technology, 2003 (cit. on p. 15).

[MH80] David Marr and Ellen Hildreth. “Theory of edge detection”. In: *Proceedings of the Royal Society of London. Series B. Biological Sciences* 207.1167 (1980), pp. 187–217 (cit. on p. 12).

[Mas02a] M Masmoudi. “The topological asymptotic, in computational methods for control applications, H. Kawarada and J. Periaux, eds, GAKUTO Internat”. In: *Ser. Math. Sci. Appli. Gakkotosho, Tokyo* (2002) (cit. on pp. 10, 11, 87).

[Mas02b] Simon Masnou. “Disocclusion: a variational approach using level lines”. In: *IEEE Transactions on Image Processing* 11.2 (2002), pp. 68–76 (cit. on p. 1).

[Mod09] Jan Modersitzki. *FAIR: flexible algorithms for image registration*. SIAM, 2009 (cit. on pp. 24, 43, 56, 92).

[MS89] David Bryant Mumford and Jayant Shah. “Optimal approximations by piecewise smooth functions and associated variational problems”. In: *Communications on Pure and Applied Mathematics* (1989) (cit. on p. 10).

[Nat01] Frank Natterer. *The mathematics of computerized tomography*. 2001 (cit. on pp. 93, 94).

[PSS13] Konstantinos Papafitsoros, Carola Bibiane Schoenlieb, and Bati Sengul. “Combined first and second order total variation inpainting using split Bregman”. In: *Image Processing On Line* 3 (2013), pp. 112–136 (cit. on pp. 31, 44).

[PMV00] Josien PW Pluim, JB Antoine Maintz, and Max A. Viergever. “Image registration by maximization of combined mutual information and gradient information”. In: *International Conference on Medical Image Computing and Computer-Assisted Intervention*. 2000, pp. 452–461 (cit. on pp. 35, 45).

[PMV03] Josien PW Pluim, JB Antoine Maintz, and Max A. Viergever. “Mutual-information-based registration of medical images: a survey”. In: *IEEE Transactions on Medical Imaging* 22.8 (2003), pp. 986–1004 (cit. on pp. 34, 45, 69, 93).

[Poc+09] Thomas Pock, Daniel Cremers, Horst Bischof, and Antonin Chambolle. “An algorithm for minimizing the Mumford-Shah functional”. In: *2009 IEEE 12th International Conference on Computer Vision*. IEEE. 2009, pp. 1133–1140 (cit. on p. 72).

[PS15] Christiane Pöschl and Otmar Scherzer. “Distance measures and applications to multi-modal variational imaging”. In: *Handbook of Mathematical Methods in Imaging*. 2015 (cit. on p. 31).

[Qiu+21] Huaqi Qiu, Chen Qin, Andreas Schuh, Kerstin Hammernik, and Daniel Rueckert. “Learning diffeomorphic and modality-invariant registration using b-splines”. In: *Medical Imaging with Deep Learning*. 2021 (cit. on pp. 65, 68).

[Qua+20] Tri T. Quang, Wei F. Chen, Francis A. Papay, and Yang Liu. “Dynamic, Real-time, fiducial-free surgical navigation with integrated multimodal optical imaging”. In: *IEEE Photonics Journal* 13.1 (2020), pp. 1–13 (cit. on pp. 23, 43, 67, 91).

[Roc+01] Alexis Roche, Xavier Pennec, Grégoire Malandain, and Nicholas Ayache. “Rigid registration of 3-D ultrasound with MR images: a new approach combining intensity and gradient information”. In: *IEEE Transactions on Medical Imaging* 20.10 (2001), pp. 1038–1049 (cit. on p. 26).

[Roh+96] Karl Rohr, H Siegfried Stiehl, Rainer Sprengel, et al. “Point-based elastic registration of medical image data using approximating thin-plate splines”. In: *International Conference on Visualization in Biomedical Computing*. Springer. 1996, pp. 297–306 (cit. on p. 25).

[RFB15a] Olaf Ronneberger, Philipp Fischer, and Thomas Brox. “U-net: Convolutional networks for biomedical image segmentation”. In: *International Conference on Medical Image Computing and computer-Assisted Intervention*. 2015, pp. 234–241 (cit. on p. 10).

[RFB15b] Olaf Ronneberger, Philipp Fischer, and Thomas Brox. “U-net: Convolutional networks for biomedical image segmentation”. In: *International Conference on Medical image computing and computer-assisted intervention*. Springer, 2015, pp. 234–241 (cit. on p. 68).

[Rot+17] Holger R Roth, Hirohisa Oda, Yuichiro Hayashi, et al. “Hierarchical 3D fully convolutional networks for multi-organ segmentation”. In: *ArXiv Preprint ArXiv:1704.06382* (2017) (cit. on p. 10).

[Rud16] Sebastian Ruder. “An overview of gradient descent optimization algorithms”. In: *arXiv Preprint arXiv:1609.04747* (2016) (cit. on p. 24).

[ROF92a] Leonid I Rudin, Stanley Osher, and Emad Fatemi. “Nonlinear total variation based noise removal algorithms”. In: *Physica D: Nonlinear Phenomena* 60.1-4 (1992), pp. 259–268 (cit. on p. 9).

[ROF92b] Leonid I. Rudin, Stanley Osher, and Emad Fatemi. “Nonlinear total variation based noise removal algorithms”. In: *Physica D: Nonlinear Phenomena* 60.1-4 (1992), pp. 259–268 (cit. on pp. 93, 95).

[Ruh+13] Jan Ruhaak, Lars Konig, Marc Hallmann, et al. “A fully parallel algorithm for multimodal image registration using normalized gradient fields”. In: *2013 IEEE 10th International Symposium on Biomedical Imaging* 38 (2013), pp. 572–575 (cit. on pp. 34, 45, 93).

[SAM03] Bessem Samet, Samuel Amstutz, and Mohamed Masmoudi. “The topological asymptotic for the Helmholtz equation”. In: *SIAM Journal on Control and Optimization* 42.5 (2003), pp. 1523–1544 (cit. on p. 11).

[Sch06] Otmar Scherzer. *Mathematical Models for Registration and Applications to Medical Imaging*. Springer, 2006 (cit. on p. 43).

[Sch+15] Johannes Schindelin, Curtis T. Rueden, Mark C. Hiner, and Kevin W. Eliceiri. “The ImageJ ecosystem: An open platform for biomedical image analysis”. In: *Molecular Reproduction and Development* 82.7-8 (2015), pp. 518–529 (cit. on pp. 23, 43, 91).

[ST90] M Ibrahim Sezan and A Murat Tekalp. “Survey of recent developments in digital image restoration”. In: *Optical Engineering* 29.5 (1990), pp. 393–404 (cit. on p. 6).

[SZ99] Jan Sokolowski and Antoni Zochowski. “On the topological derivative in shape optimization”. In: *SIAM Journal on Control and Optimization* 37.4 (1999), pp. 1251–1272 (cit. on pp. 10, 87).

[SDP13] Aristeidis Sotiras, Christos Davatzikos, and Nikos Paragios. “Deformable medical image registration: A survey”. In: *IEEE Transactions on Medical Imaging* 32.7 (2013), pp. 1153–1190 (cit. on pp. 24, 43, 92).

[SL96] Richard Szeliski and Stéphane Lavallée. “Matching 3-D anatomical surfaces with non-rigid deformations using octree-splines”. In: *International Journal of Computer Vision* 18.2 (1996), pp. 171–186 (cit. on p. 25).

[TB21] Anis Theljani and Zakaria Belhachmi. “A discrete approximation of Blake and Zisserman energy in image denoising with optimal choice of regularization parameters”. In: *Mathematical Methods in the Applied Sciences* 44.5 (2021), pp. 3857–3871 (cit. on pp. 41, 46, 72, 73).

[TC19] Anis Theljani and Ke Chen. “An augmented Lagrangian method for solving a new variational model based on gradients similarity measures and high order regularization for multimodality registration”. In: *Inverse Problems and Imaging* (2019) (cit. on pp. 24, 34–36, 43, 45, 50, 69, 92, 93, 104).

[TYW01] Andy Tsai, Anthony Yezzi, and Alan S Willsky. “Curve evolution implementation of the Mumford-Shah functional for image segmentation, denoising, interpolation, and magnification”. In: *IEEE Transactions on Image Processing* 10.8 (2001), pp. 1169–1186 (cit. on p. 72).

[Ver+09] Tom Vercauteren, Xavier Pennec, Aymeric Perchant, and Nicholas Ayache. “Diffeomorphic demons: Efficient non-parametric image registration”. In: *NeuroImage* 45.1 (2009), S61–S72 (cit. on pp. 28, 44).

[VC02] Luminita A Vese and Tony F Chan. “A multiphase level set framework for image segmentation using the Mumford and Shah model”. In: *International Journal of Computer Vision* 50.3 (2002), pp. 271–293 (cit. on p. 72).

[Vog02] Curtis R. Vogel. *Computational Methods for Inverse Problems*. SIAM, 2002 (cit. on pp. 31, 44).

[Wei98] Joachim Weickert. *Anisotropic Diffusion in Image Processing*. Vol. 1. Teubner Stuttgart, 1998 (cit. on p. 1).

[XQ11] Chen Xing and Peihua Qiu. “Intensity-based image registration by nonparametric local smoothing”. In: *IEEE Transactions on Pattern Analysis and Machine Intelligence* 33.10 (2011), pp. 2081–2092 (cit. on pp. 31, 44).

[ZV13] Massimo Zanetti and Alfonso Vitti. “The Blake-Zisserman model for digital surface models segmentation”. In: *ISPRS Annals of Photogrammetry, Remote Sensing and Spatial Information Sciences* 5 (2013), W2 (cit. on pp. 41, 46, 73).

[ZTC19a] Daoping Zhang, Anis Theljani, and Ke Chen. “On a new diffeomorphic multimodality image registration model and its convergent Gauss-Newton solver”. In: *Journal of Mathematical Research with Applications* 39.6 (2019), pp. 633–656 (cit. on pp. 53, 56).

[ZTC19b] Daoping Zhang, Anis Theljani, and Ke Chen. “On a new diffeomorphic multimodality image registration model and its convergent gauss-newton solver”. In: *Journal of Mathematical Research with Applications* 39.6 (2019), pp. 633–656 (cit. on p. 109).

[ZCY16] Jin Zhang, Ke Chen, and Bo Yu. “A novel high-order functional based image registration model with inequality constraint”. In: *Computers & Mathematics with Applications* 72.12 (2016), pp. 2887–2899 (cit. on p. 75).

[Zha+21] Jin Zhang, Jun Hu, Zhisen Jiang, et al. “Automatic 3D image registration for nano-resolution chemical mapping using synchrotron spectro-tomography”. In: *Journal of Synchrotron Radiation* 28.1 (2021) (cit. on pp. 23, 43, 91).

[ZF05] Xiao-Qun Zhang and Jacques Froment. “Total variation based Fourier reconstruction and regularization for computer tomography”. In: *IEEE Nuclear Science Symposium Conference Record, 2005* 4 (2005), pp. 2332–2336 (cit. on pp. 93, 94).

[Zho98] X. P. Zhou. “Weak lower semicontinuity of a functional with any order”. In: *Journal of Mathematical Analysis and Applications* 221.1 (1998), pp. 217–237 (cit. on p. 51).

[ZF03] Barbara Zitova and Jan Flusser. “Image registration methods: a survey”. In: *Image and Vision Computing* 21.11 (2003), pp. 977–1000 (cit. on p. 43).

7 Appendix

7.1 Appendix A: Proof of Theorem 1.

In this section, we establish the proof of the expressions of the three real numbers δ_a, δ_l and δ_J. In this section, $x_0 = 0$ is taken for simplicity reasons.

As $l_\varepsilon(\cdot)$ is an independent linear form of ε, then we have $\delta_l = 0$.

Estimate of δ_a
We have:

$$\begin{aligned}(a_\varepsilon - a_0)(u_0, v_\varepsilon) &= \int_\Omega (\alpha_\varepsilon - \alpha_0)\Delta u_0 \Delta v_\varepsilon dx + \int_\Omega (\beta_\varepsilon - \beta_0)\nabla u_0 \nabla v_\varepsilon dx,\\ &= \int_{\omega_\varepsilon} (\alpha_1 - \alpha_0)\Delta u_0 \Delta v_\varepsilon dx + \int_{\omega_\varepsilon} (\beta_1 - \beta_0)\nabla u_0 \nabla v_\varepsilon dx,\\ &= \int_{\omega_\varepsilon} (\alpha_1 - \alpha_0)\Delta u_0 \Delta (v_\varepsilon - v_0) dx + \int_{\omega_\varepsilon} (\alpha_1 - \alpha_0)\Delta u_0 \Delta v_0 dx\\ &+ \int_{\omega_\varepsilon} (\beta_1 - \beta_0)\nabla u_0 \nabla (v_\varepsilon - v_0) dx + \int_{\omega_\varepsilon} (\beta_1 - \beta_0)\nabla u_0 \nabla v_0 dx.\end{aligned}$$

We notice $w_\varepsilon = v_\varepsilon - v_0$, then we obtain:

$$\begin{aligned}(a_\varepsilon - a_0)(u_0, v_\varepsilon) = &\int_{\omega_\varepsilon} (\alpha_1 - \alpha_0)\Delta u_0 \Delta w_\varepsilon dx + \int_{\omega_\varepsilon} (\alpha_1 - \alpha_0)\Delta u_0 \Delta v_0 dx\\ &+ \int_{\omega_\varepsilon} (\beta_1 - \beta_0)\nabla u_0 \nabla w_\varepsilon dx + \int_{\omega_\varepsilon} (\beta_1 - \beta_0)\nabla u_0 \nabla v_0 dx.\end{aligned}$$

We have v_0 and v_ε solution of the following problems, respectively:

$$\begin{cases} \Delta(\alpha_0 \Delta v_0) - \operatorname{div}(\beta_0 \nabla v_0) + R^* R v_0 + \mu v_0 = -DJ_0(u_0), & \text{in } \Omega,\\ \dfrac{\partial(\alpha_0 \Delta v_0)}{\partial n} - \beta_0 \dfrac{\partial v_0}{\partial n} = 0, & \text{on } \partial\Omega,\\ \Delta v_0 = 0, & \text{on } \partial\Omega, \end{cases} \tag{7.1}$$

and

$$\begin{cases} \Delta(\alpha_\varepsilon \Delta v_\varepsilon) - \operatorname{div}(\beta_\varepsilon \nabla v_\varepsilon) + R^* R v_\varepsilon + \mu v_\varepsilon = -DJ_\varepsilon(u_0), & \text{in } \Omega,\\ \dfrac{\partial \Delta(\alpha_\varepsilon v_\varepsilon)}{\partial n} - \beta_\varepsilon \dfrac{\partial v_\varepsilon}{\partial n} = 0, & \text{on } \partial\Omega,\\ \Delta v_\varepsilon = 0, & \text{on } \partial\Omega, \end{cases} \tag{7.2}$$

Then, we deduce that $w_\varepsilon = v_\varepsilon - v_0$ is a solution of the following problem

$$\begin{cases} \Delta(\alpha_\varepsilon \Delta w_\varepsilon) - \operatorname{div}(\beta_\varepsilon \nabla w_\varepsilon) + R^* R w_\varepsilon + \mu w_\varepsilon = G_\varepsilon, & \text{in } \Omega, \\ \dfrac{\partial(\alpha_\varepsilon \Delta w_\varepsilon)}{\partial n} - \beta_\varepsilon \dfrac{\partial w_\varepsilon}{\partial n} = g_\varepsilon, & \text{on } \partial\Omega, \\ \Delta w_\varepsilon = 0, & \text{on } \partial\Omega, \end{cases} \tag{7.3}$$

where

$$G_\varepsilon = \Delta((\alpha_0 - \alpha_\varepsilon)\Delta v_0) + \operatorname{div}((\beta_\varepsilon - \beta_0)\nabla v_0) + 2\Delta((\alpha_0 - \alpha_\varepsilon)\Delta u_0) + 2\operatorname{div}((\beta_\varepsilon - \beta_0)\nabla u_0),$$
$$g_\varepsilon = \frac{\partial((\alpha_0 - \alpha_\varepsilon)\Delta v_0)}{\partial n} + (\beta_\varepsilon - \beta_0)\frac{\partial v_0}{\partial n}.$$

By multiplying the first equation of (7.3) with a function $w_\varepsilon \in \mathcal{V}$, and integrating over Ω, we obtain

$$\int_\Omega \Delta(\alpha_\varepsilon \Delta w_\varepsilon) w_\varepsilon dx - \int_\Omega \operatorname{div}(\beta_\varepsilon \nabla w_\varepsilon) w_\varepsilon dx + \int_\Omega (R^* R w_\varepsilon) \cdot w_\varepsilon dx + \mu \int_\Omega |w_\varepsilon|^2 dx = \int_\Omega G_\varepsilon w_\varepsilon dx.$$

By applying Green's formula, we obtain

$$\begin{aligned} \int_\Omega G_\varepsilon w_\varepsilon dx = &- \int_\Omega \nabla(\alpha_\varepsilon \Delta w_\varepsilon) \nabla w_\varepsilon dx + \int_{\partial\Omega} \frac{\partial(\alpha_\varepsilon \Delta w_\varepsilon)}{\partial n} w_\varepsilon d\sigma + \int_\Omega \beta_\varepsilon |\nabla w_\varepsilon|^2 dx \\ &- \int_{\partial\Omega} \beta_\varepsilon \frac{\partial w_\varepsilon}{\partial n} w_\varepsilon d\sigma + \int_\Omega (R^* R w_\varepsilon) \cdot w_\varepsilon dx + \mu \int_\Omega |w_\varepsilon|^2 dx. \end{aligned}$$

Moreover,

$$\frac{\partial \Delta(\alpha_\varepsilon w_\varepsilon)}{\partial n} - \beta_\varepsilon \frac{\partial w_\varepsilon}{\partial n} = g_\varepsilon \text{ on } \partial\Omega,$$

which gives

$$\begin{aligned} \int_\Omega G_\varepsilon w_\varepsilon dx = &\int_\Omega \alpha_\varepsilon |\Delta w_\varepsilon|^2 dx - \int_{\partial\Omega} \alpha_\varepsilon \Delta w_\varepsilon \nabla w_\varepsilon \vec{n} d\sigma + \int_{\partial\Omega} g_\varepsilon w_\varepsilon d\sigma \\ &+ \int_\Omega \beta_\varepsilon |\nabla w_\varepsilon|^2 dx + \int_\Omega (R^* R w_\varepsilon) \cdot w_\varepsilon dx + \mu \int_\Omega |w_\varepsilon|^2 dx. \end{aligned}$$

Using the fact that $\Delta w_\varepsilon = 0$ on $\partial\Omega$, we deduce

$$\begin{aligned} \int_\Omega G_\varepsilon w_\varepsilon dx - \int_{\partial\Omega} g_\varepsilon w_\varepsilon d\sigma &= \int_\Omega \alpha_\varepsilon |\Delta w_\varepsilon|^2 dx + \int_\Omega \beta_\varepsilon |\nabla w_\varepsilon|^2 dx + \int_\Omega (R^* R w_\varepsilon) \cdot w_\varepsilon dx + \mu \int_\Omega |w_\varepsilon|^2 dx. \\ &\geq \min(\alpha_\varepsilon) \|\Delta w_\varepsilon\|^2_{L^2(\Omega)} + \min(\beta_\varepsilon) \|\nabla w_\varepsilon\|^2_{L^2(\Omega)} + \|R w_\varepsilon\|^2_{L^2(\Omega)} + \mu \|w_\varepsilon\|^2_{L^2(\Omega)}, \end{aligned}$$

which implies that

$$\int_\Omega G_\varepsilon w_\varepsilon dx - \int_{\partial\Omega} g_\varepsilon w_\varepsilon d\sigma \geq \min(\alpha_\varepsilon) \|\Delta w_\varepsilon\|^2_{L^2(\Omega)} + \min(\beta_\varepsilon) \|\nabla w_\varepsilon\|^2_{L^2(\Omega)} + \mu \|w_\varepsilon\|^2_{L^2(\Omega)}.$$

Hence, there exists $c = \min(\alpha_0, \alpha_1, \beta_0, \beta_1, \mu)$ such that

$$c\|w_\varepsilon\|^2_{H^2(\Omega)} \leq \int_\Omega G_\varepsilon w_\varepsilon dx - \int_{\partial\Omega} g_\varepsilon w_\varepsilon d\sigma.$$

On the other hand, we have

$$\begin{aligned}\int_\Omega G_\varepsilon w_\varepsilon dx - \int_{\partial\Omega} g_\varepsilon w_\varepsilon d\sigma = &\int_\Omega \Delta((\alpha_0-\alpha_\varepsilon)\Delta v_0)w_\varepsilon + \operatorname{div}((\beta_\varepsilon-\beta_0)\nabla v_0)w_\varepsilon dx \\ &+ 2\int_\Omega \Delta((\alpha_0-\alpha_\varepsilon)\Delta u_0)w_\varepsilon + \operatorname{div}((\beta_\varepsilon-\beta_0)\nabla u_0)w_\varepsilon dx \\ &+ \int_{\partial\Omega} \frac{\partial((\alpha_\varepsilon-\alpha_0)\Delta v_0)}{\partial n} w_\varepsilon d\sigma + \int_{\partial\Omega}(\beta_0-\beta_\varepsilon)\frac{\partial v_0}{\partial n} w_\varepsilon d\sigma.\end{aligned}$$

Then, by applying Hölder's inequality, we deduce

$$\begin{aligned}c\|w_\varepsilon\|^2_{H^2(\Omega)} \leq &\left[\int_\Omega [\Delta((\alpha_0-\alpha_\varepsilon)\Delta v_0)]^2 dx\right]^{\frac{1}{2}} \|w_\varepsilon\|_{L^2(\Omega)} + \left[\int_\Omega [\operatorname{div}((\beta_\varepsilon-\beta_0)\nabla v_0)]^2 dx\right]^{\frac{1}{2}} \|w_\varepsilon\|_{L^2(\Omega)} \\ &+ 2\left[\int_\Omega [\Delta(\alpha_0-\alpha_\varepsilon)(\Delta u_0)]^2 dx\right]^{\frac{1}{2}} \|w_\varepsilon\|_{L^2(\Omega)} + 2\left[\int_\Omega [\operatorname{div}((\beta_\varepsilon-\beta_0)\nabla u_0)]^2 dx\right]^{\frac{1}{2}} \|w_\varepsilon\|_{L^2(\Omega)} \\ &+ \left[\int_{\partial\Omega} (\frac{\partial((\alpha_\varepsilon-\alpha_0)\Delta v_0)}{\partial n})^2 d\sigma\right]^{\frac{1}{2}} \|w_\varepsilon\|_{0,\partial\Omega} + \left[\int_{\partial\Omega} (\beta_0-\beta_\varepsilon)^2 (\frac{\partial v_0}{\partial n})^2 d\sigma\right]^{\frac{1}{2}} \|w_\varepsilon\|_{0,\partial\Omega}.\end{aligned}$$

By using the trace Theorem and the fact that embeddings $H^2(\Omega) \hookrightarrow H^1(\Omega) \hookrightarrow L^2(\Omega)$ are continuous, we have

$$\begin{cases}\|w_\varepsilon\|_{0,\partial\Omega} \leq c\|w_\varepsilon\|_{1,\Omega}, \\ \|w_\varepsilon\|_{0,\Omega} \leq \|w_\varepsilon\|_{2,\Omega}, \\ \|w_\varepsilon\|_{1,\Omega} \leq \|w_\varepsilon\|_{2,\Omega}.\end{cases}$$

So, we deduce that

$$\|w_\varepsilon\|_{2,\Omega} \leq C_1[A+B+C+D+E+F], \tag{7.4}$$

where

$$
\begin{aligned}
A^2 &= \int_\Omega [\Delta((\alpha_0 - \alpha_\varepsilon)\Delta v_0)]^2 dx, \\
B^2 &= \int_\Omega (\mathrm{div}((\beta_\varepsilon - \beta_0)\nabla v_0))^2 dx, \\
C^2 &= \int_\Omega [\Delta((\alpha_0 - \alpha_\varepsilon)\Delta u_0)]^2 dx, \\
D^2 &= \int_\Omega [\mathrm{div}((\beta_\varepsilon - \beta_0)\nabla u_0)]^2 dx, \\
E^2 &= \int_{\partial\Omega} (\frac{\partial(\alpha_\varepsilon - \alpha_0)\Delta v_0}{\partial n})^2 d\sigma, \\
F^2 &= \int_{\partial\Omega} (\beta_0 - \beta_\varepsilon)^2 (\frac{\partial v_0}{\partial n})^2 d\sigma.
\end{aligned}
$$

Lemma 7.1.1 *We have*

$$E^2 = F^2 = 0.$$

PROOF 7 *We have $\alpha_\varepsilon = \alpha_0$ (respectively $\beta_\varepsilon = \beta_0$) on $\Omega \setminus \overline{\omega_\varepsilon}$, then according to the trace Theorem, we deduce $\alpha_\varepsilon = \alpha_0$ (respectively $\beta_\varepsilon = \beta_0$) on $\partial\Omega_\varepsilon = \partial\Omega \cup \partial\omega_\varepsilon$. Then, $E^2 = F^2 = 0$.*

Lemma 7.1.2 *We have*

$$A = \left[\int_\Omega [\Delta((\alpha_0 - \alpha_\varepsilon)\Delta v_0)]^2 dx\right]^{\frac{1}{2}} = O(\varepsilon).$$

PROOF 8 *We have*

$$
\begin{aligned}
A^2 &= \int_\Omega [\Delta((\alpha_0 - \alpha_\varepsilon)\Delta v_0)]^2 dx, \\
&= \int_{\omega_\varepsilon} [\Delta((\alpha_0 - \alpha_1)\Delta v_0)]^2 dx, \\
&= (\alpha_0 - \alpha_1)^2 \int_{\omega_\varepsilon} (\Delta^2 v_0(x))^2 - (\Delta^2 v_0(0))^2 + (\Delta^2 v_0(0))^2 dx.
\end{aligned}
$$

Using the following change of variable $(\frac{x_1}{a}, \frac{x_2}{b}) = \varepsilon z$, we obtain:

$$A^2 = (\alpha_0 - \alpha_1)^2 \int_{B(0,1)} [(\Delta^2 v_0(\varepsilon z))^2 - (\Delta^2 v_0(0))^2]\varepsilon^2 ab dz + (\alpha_0 - \alpha_1)^2 (\Delta^2 v_0(0))^2 \varepsilon^2 ab\pi.$$

As $\Delta^2 v_0$ is continuous in a neighborhood of 0, then there exists $M > 0$ such that

$$|\Delta^2 v_0(\varepsilon z)^2 - \Delta^2 v_0(0)^2| \leq M.$$

Thus,

$$A^2 \leq (\alpha_0 - \alpha_1)^2 \varepsilon^2 ab\pi (M + (\Delta^2 v_0(0))^2),$$

and therefore

$$A^2 = O(\varepsilon^2) \quad \Rightarrow \quad A = O(\varepsilon).$$

Lemma 7.1.3 *We have:*

$$B = \left[\int_\Omega (\mathrm{div}((\beta_\varepsilon - \beta_0)\nabla v_0))^2 dx\right]^{\frac{1}{2}} = O(\varepsilon),$$
$$C = \left[\int_\Omega [\Delta((\alpha_0 - \alpha_\varepsilon)\Delta u_0)]^2 dx\right]^{\frac{1}{2}} = O(\varepsilon),$$
$$D = \left[\int_\Omega (\mathrm{div}((\beta_\varepsilon - \beta_0)\nabla u_0))^2 dx\right]^{\frac{1}{2}} = O(\varepsilon).$$

PROOF 9 *We have*

$$B^2 = \int_\Omega (\mathrm{div}((\beta_\varepsilon - \beta_0)\nabla v_0))^2 dx = \int_{\omega_\varepsilon} (\beta_1 - \beta_0)^2 (\Delta v_0)^2 dx,$$
$$= (\beta_1 - \beta_0)^2 \left[\int_{\omega_\varepsilon} (\Delta v_0(x))^2 - (\Delta v_0(0))^2 dx + \int_{\omega_\varepsilon} (\Delta v_0(0))^2 dx\right].$$

Using the following change of variable $(\frac{x_1}{a}, \frac{x_2}{b}) = \varepsilon z$*, we obtain*

$$B^2 = (\beta_1 - \beta_0)^2 \left[\varepsilon^2 ab \int_{B(0,1)} (\Delta v_0(\varepsilon z))^2 - (\Delta v_0(0))^2 dz + \varepsilon^2 ab\pi \Delta v_0(0))^2\right].$$

As Δv_0 *is continuous in a neighborhood of 0, we obtain:*

$$|(\Delta v_0(\varepsilon z))^2 - (\Delta v_0(0))^2| = o(1).$$

Then, there exists $M > 0$ *such that*

$$B^2 \leq (\beta_1 - \beta_0)^2 \varepsilon^2 ab\pi \left[M + (\Delta v_0(0))^2\right],$$

which implies that

$$B^2 = O(\varepsilon^2) \ \Rightarrow B = O(\varepsilon).$$

By using some classical computation techniques, we obtain

$$C^2 = O(\varepsilon^2) \quad \Rightarrow \quad C = O(\varepsilon),$$
$$D^2 = O(\varepsilon^2) \quad \Rightarrow \quad D = O(\varepsilon).$$

According to inequality (7.4) and lemmas 7.1.1, 7.1.2 and 7.1.3, we deduce that

$$\|w_\varepsilon\|_{H^2(\Omega)} = O(\varepsilon). \tag{7.5}$$

Lemma 7.1.4 *We have*

$$\int_{\omega_\varepsilon} \nabla u_0 \nabla w_\varepsilon dx = o(\varepsilon^2).$$

PROOF 10 *We have*

$$\left| \int_{\omega_\varepsilon} \nabla u_0 \nabla w_\varepsilon dx \right| \leq \|\nabla u_0\|_{L^\infty(\omega\varepsilon)} \int_{\omega_\varepsilon} |\nabla w_\varepsilon| dx.$$

By applying Hölder's inequality for $p, q \in [1, +\infty]$ *such that* $\frac{1}{p} + \frac{1}{q} = 1$ *we obtain*

$$\left| \int_{\omega_\varepsilon} \nabla u_0 \nabla w_\varepsilon dx \right| \leq c \left(\int_{\omega_\varepsilon} 1 dx \right)^{\frac{1}{p}} \|\nabla w_\varepsilon\|_{L^q(\omega_\varepsilon)} \leq c \left(\varepsilon^2 ab \right)^{\frac{1}{p}} \|\nabla w_\varepsilon\|_{L^q(\omega_\varepsilon)}.$$

Choosing $p = \frac{3}{2}$ *and* $q = 3$ *in the above and since the embedding* $L^3(\Omega) \hookrightarrow L^2(\Omega)$ *is continuous, we obtain*

$$\left| \int_{\omega_\varepsilon} \nabla u_0 \nabla w_\varepsilon dx \right| \leq c \left(\varepsilon^2 ab \right)^{\frac{2}{3}} \|\nabla w_\varepsilon\|_{L^2(\Omega)} \leq c \left(\varepsilon^2 ab \right)^{\frac{2}{3}} \|w_\varepsilon\|_{H^2(\Omega)}.$$

Moreover

$$\|w_\varepsilon\|_{H^2(\Omega)} = O(\varepsilon).$$

Then,

$$\left| \int_{\omega_\varepsilon} \nabla u_0 \nabla w_\varepsilon dx \right| \leq c\varepsilon^{\frac{7}{3}} (ab)^{\frac{2}{3}},$$

which implies

$$\int_{\omega_\varepsilon} \nabla u_0 \nabla w_\varepsilon dx = o(\varepsilon^2).$$

Lemma 7.1.5 *We have*

$$\int_{\omega_\varepsilon} \Delta u_0 \Delta w_\varepsilon dx = -\varepsilon^2 (k_0^{a,b} + 1) \Delta v_0(x_0) \left(k_1^{a,b} \frac{\partial^2 u_0(x_0)}{\partial x^2} + k_2^{a,b} \frac{\partial^2 u_0(x_0)}{\partial y^2} + k_3^{a,b} \left(\frac{\partial^2 u_0(x_0)}{\partial x \partial y} + \frac{\partial^2 u_0(x_0)}{\partial y \partial x} \right) \right) + o(\varepsilon^2),$$

where

$$k_0^{a,b} = \frac{2\pi}{\frac{1}{2}\int_0^{2\pi} \sqrt{a^2\cos^2(\theta) + b^2\sin^2(\theta)}d\theta - \pi},$$
$$k_1^{a,b} = \int_0^{2\pi} \frac{a^2\cos^2(\theta)}{\sqrt{a^2\cos^2(\theta) + b^2\sin^2(\theta)}}\, d\theta,$$
$$k_2^{a,b} = \int_0^{2\pi} \frac{b^2\sin^2(\theta)}{\sqrt{a^2\cos^2(\theta) + b^2\sin^2(\theta)}}\, d\theta,$$
$$k_3^{a,b} = \int_0^{2\pi} \frac{ab\ \cos(\theta)\sin(\theta)}{\sqrt{a^2\cos^2(\theta) + b^2\sin^2(\theta)}}\, d\theta.$$

PROOF 11 *By applying Green's formula, we obtain*

$$\begin{aligned}\int_{\omega_\varepsilon} \Delta u_0 \Delta w_\varepsilon dx &= -\int_{\omega_\varepsilon} \nabla(\Delta u_0)\nabla w_\varepsilon dx + \int_{\partial\omega_\varepsilon} \frac{\partial \omega_\varepsilon}{\partial n}\Delta u_0 dx,\\ &= \int_{\omega_\varepsilon} \Delta^2 u_0 w_\varepsilon dx - \int_{\partial\omega_\varepsilon} w_\varepsilon \frac{\partial \Delta u_0}{\partial n} d\sigma + \int_{\partial\omega_\varepsilon} \frac{\partial w_\varepsilon}{\partial n}\Delta u_0 dx.\end{aligned}$$

As $\Delta^2 u_0$ is continuous in a neighborhood of x_0, we get

$$\left|\int_{\omega_\varepsilon} \Delta^2 u_0 w_\varepsilon dx\right| \leq \|\Delta^2 u_0\|_{L^\infty(\omega_\varepsilon)} \int_{\omega_\varepsilon} |w_\varepsilon| dx \leq c(ab)^{\frac{3}{4}}\varepsilon^{\frac{5}{2}}.$$

Then

$$\int_{\omega_\varepsilon} \Delta^2 u_0 w_\varepsilon dx = o(\varepsilon^2),$$

and according to Appendix B, we have

$$\int_{\partial\omega_\varepsilon} \frac{\partial \Delta u_0}{\partial n} w_\varepsilon d\sigma = o(\varepsilon^2),$$

and

$$\begin{aligned}\int_{\partial\omega_\varepsilon} \Delta u_0 \frac{\partial w_\varepsilon}{\partial n} d\sigma = &-\varepsilon^2(k_0^{a,b}+1)\Delta v_0(x_0)\\ &\left(k_1^{a,b}\frac{\partial^2 u_0(x_0)}{\partial x^2} + k_2^{a,b}\frac{\partial^2 u_0(x_0)}{\partial y^2} + k_3^{a,b}\left(\frac{\partial^2 u_0(x_0)}{\partial x \partial y} + \frac{\partial^2 u_0(x_0)}{\partial y \partial x}\right)\right) + o(\varepsilon^2).\end{aligned}$$

Then, we obtain

$$\begin{aligned}\int_{\omega_\varepsilon} \Delta u_0 \Delta w_\varepsilon dx = -\varepsilon^2(k_0^{a,b}+1)\Delta v_0(x_0) &\left(k_1^{a,b}\frac{\partial^2 u_0(x_0)}{\partial x^2} + k_2^{a,b}\frac{\partial^2 u_0(x_0)}{\partial y^2}\right.\\ &\left. + k_3^{a,b}\left(\frac{\partial^2 u_0(x_0)}{\partial x \partial y} + \frac{\partial^2 u_0(x_0)}{\partial y \partial x}\right)\right) + o(\varepsilon^2).\end{aligned}$$

Lemma 7.1.6 *We have*

$$\int_{\omega_\varepsilon} \nabla u_0 \nabla v_0 dx = \varepsilon^2 ab\pi \nabla u_0(0)\nabla v_0(0) + o(\varepsilon^2).$$

PROOF 12 *We have*

$$\int_{\omega_\varepsilon} \nabla u_0 \nabla v_0(x)dx = \int_{\omega_\varepsilon} (\nabla u_0 \nabla v_0)(x) - (\nabla u_0 \nabla v_0)(0)dx + \int_{\omega_\varepsilon} (\nabla u_0 \nabla v_0)(0)dx.$$

By using the following change of variable $(\frac{x_1}{a}, \frac{x_2}{b}) = \varepsilon z$*, we obtain*

$$\int_{\omega_\varepsilon} (\nabla u_0 \nabla v_0)(x)dx = \int_{B(0,1)} ab\varepsilon^2 \left[(\nabla u_0 \nabla v_0)(\varepsilon z) - (\nabla u_0 \nabla v_0)(0)\right] dz + \varepsilon^2 ab\pi (\nabla u_0 \nabla v_0)(0).$$

By applying the first-order Taylor formula in the neighborhood of 0, we obtain

$$|\nabla u_0(\varepsilon z)\nabla v_0(\varepsilon z) - \nabla u_0(0)\nabla v_0(0)| = O(\varepsilon).$$

Thus

$$\int_{\omega_\varepsilon} (\nabla u_0 \nabla v_0)(x)dx = o(\varepsilon^2) + \varepsilon^2 ab\pi \nabla u_0(0)\nabla v_0(0).$$

Lemma 7.1.7 *We have*

$$\int_{\omega_\varepsilon} (\Delta u_0 \Delta v_0)(x)dx = \varepsilon^2 ab\pi \Delta u_0(0)\Delta v_0(0) + o(\varepsilon^2).$$

PROOF 13 *We have*

$$\int_{\omega_\varepsilon} (\Delta u_0 \Delta v_0)(x)dx = \int_{\omega_\varepsilon} (\Delta u_0 \Delta v_0)(x) - (\Delta u_0 \Delta v_0)(0)dx + \int_{\omega_\varepsilon} (\Delta u_0 \Delta v_0)(0)dx.$$

By applying the change of variable $(\frac{x_1}{a}, \frac{x_2}{b}) = \varepsilon z$*, we obtain*

$$\int_{\omega_\varepsilon} (\Delta u_0 \Delta v_0)(x)dx = \int_{B(0,1)} ab\varepsilon^2 \left[(\Delta u_0 \Delta v_0)(\varepsilon z) - (\Delta u_0 \Delta v_0)(0)\right] dz + \varepsilon^2 ab\pi (\Delta u_0 \Delta v_0)(0).$$

By applying the first-order Taylor formula in the neighborhood of 0, we obtain

$$|\Delta u_0(\varepsilon z)\Delta v_0(\varepsilon z) - \Delta u_0(0)\Delta v_0(0)| = O(\varepsilon).$$

Then,

$$\int_{\omega_\varepsilon} (\Delta u_0 \Delta v_0)(x)dx = \varepsilon^2 ab\pi \Delta u_0(0)\Delta v_0(0) + o(\varepsilon^2).$$

Estimation of δ_J

The estimation of δ_J is based on the following hypothesis

$$J_\varepsilon(u_\varepsilon) - J_0(u_0) = DJ_\varepsilon(u_0)(u_\varepsilon - u_0) + f(\varepsilon)\delta_J + o(f(\varepsilon)). \tag{7.6}$$

We have

$$\begin{aligned} J_\varepsilon(u_\varepsilon) - J_0(u_0) &= \left[\int_\Omega \alpha_\varepsilon |\Delta u_\varepsilon|^2 dx - \int_\Omega \alpha_0 |\Delta u_0|^2 dx\right] + \left[\int_\Omega \beta_\varepsilon |\nabla u_\varepsilon|^2 dx - \int_\Omega \beta_0 |\nabla u_0|^2 dx\right], \\ &= K_\varepsilon^1 + K_\varepsilon^2. \end{aligned}$$

According to lemmas 7.1.8, 7.1.9 and 7.1.12 (Below), we get

$$K_\varepsilon^1 = (\alpha_1 - \alpha_0)ab\pi\varepsilon^2 |\Delta u_0(0)|^2 + 2\int_\Omega \alpha_\varepsilon \Delta u_0 \Delta(u_\varepsilon - u_0)dx + o(\varepsilon^2) + \int_\Omega \alpha_\varepsilon |\Delta(u_\varepsilon - u_0)|^2 dx$$

$$K_\varepsilon^2 = (\beta_1 - \beta_0)ab\pi\varepsilon^2 |\nabla u_0(0)|^2 + 2\int_\Omega \beta_\varepsilon \nabla u_0 \nabla(u_\varepsilon - u_0)dx + o(\varepsilon^2) + \int_\Omega \beta_\varepsilon \left|\nabla(u_\varepsilon - u_0)\right|^2 dx.$$

$$\int_\Omega \beta_\varepsilon \left|\nabla(u_\varepsilon - u_0)\right|^2 dx + \int_\Omega \alpha_\varepsilon \left|\Delta(u_\varepsilon - u_0)\right|^2 dx = o(\varepsilon^2).$$

Then, we obtain

$$\begin{aligned} J_\varepsilon(u_\varepsilon) - J_0(u_0) =& ab\pi\varepsilon^2 \left[(\alpha_1 - \alpha_0)|\Delta u_0(0)|^2 + (\beta_1 - \beta_0)|\nabla u_0(0)|^2\right] \\ &+ DJ_\varepsilon(u_0)(u_\varepsilon - u_0) + o(\varepsilon^2). \end{aligned}$$

Lemma 7.1.8 *We have*

$$\begin{aligned} \int_\Omega \alpha_\varepsilon |\Delta u_\varepsilon|^2 dx - \int_\Omega \alpha_0 |\Delta u_0|^2 dx = (\alpha_1 - \alpha_0)ab\pi\varepsilon^2 |\Delta u_0(0)|^2 + \int_\Omega \alpha_\varepsilon |\Delta(u_\varepsilon - u_0)|^2 dx \\ + 2\int_\Omega \alpha_\varepsilon \Delta u_0 \Delta(u_\varepsilon - u_0)dx + o(\varepsilon^2). \end{aligned}$$

PROOF 14 *We have*

$$\begin{aligned} \int_\Omega \alpha_\varepsilon |\Delta u_\varepsilon|^2 dx - \int_\Omega \alpha_0 |\Delta u_0|^2 dx &= \int_\Omega \alpha_\varepsilon |\Delta u_\varepsilon|^2 dx - \int_\Omega ((\alpha_0 - \alpha_\varepsilon) + \alpha_\varepsilon)|\Delta u_0|^2 dx, \\ &= -\int_\Omega (\alpha_0 - \alpha_\varepsilon)|\Delta u_0|^2 dx + \int_\Omega \alpha_\varepsilon (|\Delta u_\varepsilon|^2 - |\Delta u_0|^2)dx, \\ &= -\int_{\omega_\varepsilon} (\alpha_0 - \alpha_1)|\Delta u_0|^2 dx + \int_\Omega \alpha_\varepsilon \left(|\Delta u_\varepsilon|^2 - |\Delta u_0|^2\right) dx. \end{aligned}$$

On the one hand, we have

$$\int_{\omega_\varepsilon} |\Delta u_0(x)|^2 dx = \int_{\omega_\varepsilon} \left[|\Delta u_0(x)|^2 - |\Delta u_0(0)|^2\right] dx + \int_{\omega_\varepsilon} |\Delta u_0(0)|^2 dx.$$

By using the change of variable $(\frac{x_1}{a}, \frac{x_2}{b}) = \varepsilon z$ *and applying first-order Taylor's formula in the neighborhood of zero, we get*

$$\int_{\omega_\varepsilon} |\Delta u_0(x)|^2 dx = o(\varepsilon^2) + ab\pi\varepsilon^2 |\Delta u_0(0)|^2.$$

Furthermore, we have

$$\begin{aligned}\int_\Omega \alpha_\varepsilon \left(|\Delta u_\varepsilon|^2 - |\Delta u_0|^2\right) dx &= \int_\Omega \alpha_\varepsilon \left[|\Delta u_\varepsilon - \Delta u_0|^2 + 2\Delta u_0 \Delta(u_\varepsilon - u_0)\right] dx, \\ &= \int_\Omega \alpha_\varepsilon \left|\Delta(u_\varepsilon - u_0)\right|^2 dx + 2\int_\Omega \alpha_\varepsilon \Delta u_0 \Delta(u_\varepsilon - u_0) dx.\end{aligned}$$

Then, we get

$$\begin{aligned}\int_\Omega \alpha_\varepsilon |\Delta u_\varepsilon|^2 dx - \int_\Omega \alpha_0 |\Delta u_0|^2 dx = (\alpha_1 - \alpha_0) ab\pi\varepsilon^2 |\Delta u_0(0)|^2 + \int_\Omega \alpha_\varepsilon |\Delta(u_\varepsilon - u_0)|^2 dx \\ +2\int_\Omega \alpha_\varepsilon \Delta u_0 \Delta(u_\varepsilon - u_0) dx.\end{aligned}$$

Lemma 7.1.9 *We have*

$$\begin{aligned}\int_\Omega \beta_\varepsilon |\nabla u_\varepsilon|^2 dx - \int_\Omega \beta_0 |\nabla u_0|^2 dx = (\beta_1 - \beta_0) ab\pi\varepsilon^2 |\nabla u_0(0)|^2 + \int_\Omega \beta_\varepsilon \left|\nabla(u_\varepsilon - u_0)\right|^2 dx \\ + 2\int_\Omega \beta_\varepsilon \nabla u_0 \nabla(u_\varepsilon - u_0) dx + o(\varepsilon^2).\end{aligned}$$

PROOF 15 *We have*

$$\begin{aligned}\int_\Omega \beta_\varepsilon |\nabla u_\varepsilon|^2 dx - \int_\Omega \beta_0 |\nabla u_0|^2 dx &= \int_\Omega \beta_\varepsilon |\nabla u_\varepsilon|^2 dx - \int_\Omega \left((\beta_0 - \beta_\varepsilon) + \beta_\varepsilon\right) |\nabla u_0|^2 dx, \\ &= \int_\Omega \beta_\varepsilon \left(|\nabla u_\varepsilon|^2 - |\nabla u_0|^2\right) dx - \int_{\omega_\varepsilon} (\beta_0 - \beta_1) |\nabla u_0|^2 dx, \\ &= (\beta_1 - \beta_0) \left[\int_{\omega_\varepsilon} |\nabla u_0(x)|^2 - |\nabla u_0(0)|^2 dx + \int_{\omega_\varepsilon} |\nabla u_0(0)|^2 dx\right] \\ &+ \int_\Omega \beta_\varepsilon |\nabla(u_\varepsilon - u_0)|^2 dx + 2\int_\Omega \beta_\varepsilon \nabla u_0 \nabla(u_\varepsilon - u_0) dx.\end{aligned}$$

By using the variable, $(\frac{x_1}{a}, \frac{x_2}{b}) = \varepsilon z$*, and applying Taylor's formula to order 1 in the neighborhood of zero, we get the result.*

Let $X_\varepsilon = u_\varepsilon - u_0$, then it is easy to verify that X_ε is a solution of

$$\begin{cases} \Delta(\alpha_\varepsilon \Delta(X_\varepsilon)) - \operatorname{div}(\beta_\varepsilon \nabla(X_\varepsilon)) + R^* R(X_\varepsilon) + \mu X_\varepsilon = \Delta((\alpha_0 - \alpha_\varepsilon)\Delta u_0) + \operatorname{div}((\beta_\varepsilon - \beta_0)\nabla u_0), & \text{in } \Omega, \\ \dfrac{\partial(\alpha_\varepsilon \Delta(X_\varepsilon))}{\partial n} - \beta_\varepsilon \dfrac{\partial(X_\varepsilon)}{\partial n} = \dfrac{\partial((\alpha_0 - \alpha_\varepsilon)\Delta u_0)}{\partial n} + (\beta_\varepsilon - \beta_0)\dfrac{\partial u_0}{\partial n}, & \text{on } \partial\Omega, \\ \Delta(X_\varepsilon) = 0, & \text{on } \partial\Omega. \end{cases} \tag{7.7}$$

Using the same argument of the proof of (7.5), we show that

$$||X_\varepsilon||_{H^2(\Omega)} = O(\varepsilon). \tag{7.8}$$

Lemma 7.1.10 *We have*

$$\int_{\omega_\varepsilon} \Delta((\alpha_\varepsilon - \alpha_0)\Delta u_0)X_\varepsilon dx = o(\varepsilon^2).$$

PROOF 16 *We have*

$$\left|\int_{\omega_\varepsilon} \Delta((\alpha_\varepsilon - \alpha_0)\Delta u_0)X_\varepsilon dx\right| \leq \|\Delta((\alpha_\varepsilon - \alpha_0)\Delta u_0)\|_{L^\infty(\omega_\varepsilon)} \int_{\omega_\varepsilon} |X_\varepsilon| dx.$$

By applying Hölder's inequality with $p, q \in [1, +\infty]$ *such that* $\frac{1}{p} + \frac{1}{q} = 1$*, we get*

$$\begin{aligned}\left|\int_{\omega_\varepsilon} \Delta((\alpha_\varepsilon - \alpha_0)\Delta u_0)X_\varepsilon dx\right| &\leq c\left(\int_{\omega_\varepsilon} 1dx\right)^{\frac{1}{p}} \|X_\varepsilon\|_{L^q(\omega_\varepsilon)}, \\ &\leq c\left(\varepsilon^2 ab\right)^{\frac{1}{p}} \|X_\varepsilon\|_{L^q(\omega_\varepsilon)}.\end{aligned}$$

By choosing $p = \frac{4}{3}$ *and* $q = 4$ *in the above and since the injection of* $H^2(\Omega)$ *in* $L^4(\Omega)$ *is continuous, we have*

$$\left|\int_{\omega_\varepsilon} \Delta((\alpha_\varepsilon - \alpha_0)\Delta u_0)X_\varepsilon dx\right| \leq c\left(\varepsilon^2 ab\right)^{\frac{3}{4}} \|X_\varepsilon\|_{H^2(\Omega)}.$$

However,

$$\|X_\varepsilon\|_{H^2(\Omega)} = O(\varepsilon),$$

which gives

$$\left|\int_{\omega_\varepsilon} \Delta((\alpha_\varepsilon - \alpha_0)\Delta u_0)dx\right| \leq c\varepsilon^{\frac{5}{2}}(ab)^{\frac{3}{4}}.$$

and finishes the proof of the lemma.

Lemma 7.1.11 *We have*

$$\int_{\omega_\varepsilon} \Delta u_0 X_\varepsilon dx = o(\varepsilon^2) \quad \text{and} \quad \int_{\omega_\varepsilon} u_0 X_\varepsilon dx = o(\varepsilon^2).$$

PROOF 17 *We use the same approach as in the previous proof.*

Lemma 7.1.12 *We have*

$$\int_\Omega \beta_\varepsilon \left|\nabla(u_\varepsilon - u_0)\right|^2 dx + \int_\Omega \alpha_\varepsilon \left|\Delta(u_\varepsilon - u_0)\right|^2 dx = o(\varepsilon^2).$$

PROOF 18 *Let $X_\varepsilon = u_\varepsilon - u_0$. By applying Green's formula, we show that*

$$\begin{aligned}
&\int_\Omega \beta_\varepsilon |\nabla(X_\varepsilon)|^2 dx + \int_\Omega \alpha_\varepsilon \left|\Delta(X_\varepsilon)\right|^2 dx \\
&= -\int_\Omega \operatorname{div}\left(\beta_\varepsilon \nabla X_\varepsilon\right) X_\varepsilon dx + \int_{\partial\Omega} \beta_\varepsilon \frac{\partial X_\varepsilon}{\partial n} X_\varepsilon d\sigma - \int_\Omega \nabla(\alpha_\varepsilon \Delta(X_\varepsilon)) \nabla X_\varepsilon dx + \int_{\partial\Omega} \alpha_\varepsilon \frac{\partial X_\varepsilon}{\partial n} \Delta X_\varepsilon d\sigma, \\
&= -\int_\Omega \mathit{div}(\beta_\varepsilon \nabla X_\varepsilon) X_\varepsilon dx + \int_{\partial\Omega} \beta_\varepsilon \frac{\partial X_\varepsilon}{\partial n} X_\varepsilon d\sigma + \int_\Omega \Delta(\alpha_\varepsilon \Delta(X_\varepsilon)) X_\varepsilon dx - \int_{\partial\Omega} X_\varepsilon \frac{\partial(\alpha_\varepsilon \Delta X_\varepsilon)}{\partial n} d\sigma \\
&\qquad + \int_{\partial\Omega} \alpha_\varepsilon \frac{\partial X_\varepsilon}{\partial n} \Delta X_\varepsilon d\sigma.
\end{aligned}$$

By multiplying (7.7) by X_ε and integrating on Ω, we get

$$\begin{aligned}
&\int_\Omega \beta_\varepsilon |\nabla(X_\varepsilon)|^2 dx + \int_\Omega \alpha_\varepsilon |\Delta(X_\varepsilon)|^2 dx \\
&= -\int_\Omega |RX_\varepsilon|^2 dx + \int_\Omega \Delta((\alpha_0 - \alpha_\varepsilon)\Delta u_0) X_\varepsilon dx + \int_\Omega \mathit{div}\left((\beta_\varepsilon - \beta_0)\nabla u_0\right) X_\varepsilon dx \\
&\qquad - \mu \int_\Omega |X_\varepsilon|^2 dx + \int_{\partial\Omega} \frac{\partial((\alpha_\varepsilon - \alpha_0)\Delta u_0)}{\partial n} X_\varepsilon d\sigma + \int_{\partial\Omega} (\beta_0 - \beta_\varepsilon) \frac{\partial u_0}{\partial n} X_\varepsilon dx.
\end{aligned}$$

However, we have $\alpha_\varepsilon = \alpha_0$ (respectively $\beta_\varepsilon = \beta_0$) on $\Omega \setminus \overline{\omega_\varepsilon}$, then according to the trace Theorem, we deduce $\alpha_\varepsilon = \alpha_0$ (respectively $\beta_\varepsilon = \beta_0$) on $\partial\Omega$. Then, we have

$$\int_\Omega \beta_\varepsilon |\nabla(X_\varepsilon)|^2 dx + \int_\Omega \alpha_\varepsilon |\Delta(X_\varepsilon)|^2 dx \leq \int_\Omega \Delta((\alpha_0 - \alpha_\varepsilon)\Delta u_0) X_\varepsilon dx + \int_\Omega \operatorname{div}\left((\beta_\varepsilon - \beta_0)\nabla u_0\right) X_\varepsilon dx$$

by resorting to Lemmas 7.1.10 and 7.1.11 which finishes the proof.

7.2 Appendix B: Technical computations for the Proof of Lemma 7.1.5

We recall that E denotes the ellipse and $\mathbb{R}^2 \setminus E$ the exterior domain. We denoted by $W^2(\mathbb{R}^2 \setminus E)$ the weighted Sobolev space defined by:

$$\begin{aligned}
W^2(\mathbb{R}^2 \setminus E) = \Bigg\{ & u, \frac{u}{(1+r^2)\log(2+r^2)} \in L^2(\mathbb{R}^2 \setminus E), \\
& \frac{\nabla u}{(1+r^2)^{\frac{1}{2}} \log(2+r^2)} \in L^2(\mathbb{R}^2 \setminus E), \nabla^2 u \in L^2(\mathbb{R}^2 \setminus E), \Bigg\}
\end{aligned}$$

with $r = \|x\|$ and $W^2(\mathbb{R}^2 \setminus E)/\wp_1$ the functional quotient space, where $\wp_1$ is the set of polynomial of degree less or equal than 1.
We assume that $H_\varepsilon = w_{\varepsilon|\Omega_\varepsilon}$ is the solution of the following problem

$$\begin{cases} \alpha_0 \Delta^2 H_\varepsilon - \beta_0 \Delta H_\varepsilon + R^* R H_\varepsilon + \mu H_\varepsilon = 0, & \text{in } \Omega_\varepsilon, \\ \alpha_0 \dfrac{\partial(\Delta H_\varepsilon)}{\partial n} - \beta_0 \dfrac{\partial H_\varepsilon}{\partial n} = g_\varepsilon(0), & \text{on } \partial\Omega, \\ \Delta H_\varepsilon = 0, & \text{on } \partial\Omega. \\ \alpha_0 \dfrac{\partial(\Delta H_\varepsilon)}{\partial n} - \beta_0 \dfrac{\partial H_\varepsilon}{\partial n} = -\alpha_0 \dfrac{\partial(\Delta u_0)}{\partial n} + \beta_0 \dfrac{\partial(u_0)}{\partial n}, & \text{on } \partial\omega_\varepsilon, \\ \Delta H_\varepsilon = -\Delta v_0, & \text{on } \partial\omega_\varepsilon. \end{cases} \tag{7.9}$$

By splitting H_ε as $H_\varepsilon = \varepsilon^2 T(\frac{x}{\varepsilon}) + e_\varepsilon$, we show that $T_\varepsilon \in W^2(\mathbb{R}^2 \setminus E)/\wp_1$ solution for the exterior problem

$$\begin{cases} \Delta^2 T = 0, & \text{in } \mathbb{R}^2 \setminus E, \\ \alpha_0 \frac{\partial \Delta T}{\partial n} = 0, & \text{on } \partial E, \\ \Delta T = -\Delta v_0(0), & \text{on } \partial E, \end{cases} \tag{7.10}$$

and e_ε is the solution of the following problem

$$\begin{cases} \alpha_0 \Delta^2 e_\varepsilon - \beta_0 \Delta e_\varepsilon + R^* R e_\varepsilon + \mu e_\varepsilon = F_\varepsilon & \text{in } \Omega_\varepsilon, \\ \alpha_0 \dfrac{\partial \Delta e_\varepsilon}{\partial n} - \beta_0 \dfrac{\partial e_\varepsilon}{\partial n} = -\dfrac{\alpha_0}{\varepsilon} \dfrac{\partial T(\frac{x}{\varepsilon})}{\partial n} + \beta_0 \varepsilon \dfrac{\partial T(\frac{x}{\varepsilon})}{\partial n} + g_\varepsilon(0) & \text{on } \partial\Omega, \\ \Delta e_\varepsilon = -\Delta(T(\frac{x}{\varepsilon})) & \text{on } \partial\Omega. \\ \alpha_0 \dfrac{\partial \Delta e_\varepsilon}{\partial n} - \beta_0 \dfrac{\partial e_\varepsilon}{\partial n} = -\alpha_0 \left(\dfrac{1}{\varepsilon} \dfrac{\partial T(\frac{x}{\varepsilon})}{\partial n} + \dfrac{\partial(\Delta u_0)}{\partial n} \right) + \beta_0 \left(\varepsilon \dfrac{\partial T(\frac{x}{\varepsilon})}{\partial n} + \dfrac{\partial u_0}{\partial n} \right) & \text{on } \partial\omega_\varepsilon, \\ \Delta e_\varepsilon = -\left(\Delta v_0 - \Delta v_0(0)\right) & \text{on } \partial\omega_\varepsilon, \end{cases} \tag{7.11}$$

with $F_\varepsilon = \beta_0 \Delta T(\frac{x}{\varepsilon}) - \varepsilon^2 R^* R T(\frac{x}{\varepsilon}) - \mu \varepsilon^2 T(\frac{x}{\varepsilon})$.

Lemma 7.2.1 *We have*

$$\int_{\partial\omega_\varepsilon} w_\varepsilon \frac{\partial \Delta u_0}{\partial n}\, dx = o(\varepsilon^2).$$

PROOF 19 *According to Lemma B6 in [AD15], we have*

$$\|w_\varepsilon\|_{0,\Omega_\varepsilon} = O(-\varepsilon^2 \log(\varepsilon)).$$

Using the Cauchy-Schwartz inequality and the trace theorem, we show that:

$$\left| \int_{\partial\omega_\varepsilon} w_\varepsilon \frac{\partial \Delta u_0}{\partial n} dx \right| \leq \|w_\varepsilon\|_{0,\Omega_\varepsilon} \left(\int_{\partial\omega_\varepsilon} |\Delta u_0|^2 d\sigma \right)^{\frac{1}{2}}.$$

By taking the change of variable $(\frac{x_1}{\varepsilon}, \frac{x_2}{\varepsilon}) = \varepsilon z$*, we obtain*

$$\left(\int_{\partial\omega_\varepsilon} |\Delta u_0|^2 d\sigma\right)^{\frac{1}{2}} = O(\sqrt{\varepsilon}).$$

Then we deduce

$$\int_{\partial\omega_\varepsilon} w_\varepsilon \frac{\partial \Delta u_0}{\partial n}\, dx = o(\varepsilon^2).$$

From Theorem B.3 in [AD15], the authors show that the following exterior problem:

$$(\mathcal{P}_{ext}) \begin{cases} \Delta^2 T = 0, & \text{in } \mathbb{R}^2 \setminus E, \\ \frac{\partial \Delta T}{\partial n} = g_1, & \text{on } \partial E, \\ \Delta T = g_2, & \text{on } \partial E, \end{cases} \tag{7.12}$$

where $g_1 \in H^{-\frac{3}{2}}(\partial E)$ and $g_2 \in H^{-\frac{1}{2}}(\partial E)$ admits a unique solution $T \in W^2(\mathbb{R}^2 \setminus E)/_{\wp_1}$, given by

$$T(x) = \int_{\partial E} \lambda_1(y) E(x-y) d\sigma(y) + \int_{\partial B} \lambda_2(y) \partial_{n_y} E(x-y) d\sigma(y), \forall x \in \mathbb{R}^2 \setminus E,$$

where $E(x-y) = -\frac{1}{8\pi}\|x-y\|^2 \log(\|x-y\|)$ and λ_1, λ_2 satisfy:

$$\begin{aligned} -\frac{\lambda_1(x)}{2} + \int_{\partial E} \lambda_1(y) \partial_{n_x}(\Delta E(x-y)) d\sigma(y) + \oint_{\partial E} \lambda_2(y) \partial_{n_x}(\Delta(\partial_{n_y} E(x-y))) d\sigma(y) \\ + a_0 + a_1 x + a_2 x_2 = g_1(x) \\ \frac{\lambda_2(x)}{2} + \int_{\partial E} \lambda_1(y) \Delta_x(E(x-y)) d\sigma(y) + \int_{\partial E} \lambda_2(y) \Delta_x(\partial_{n_y} E(x-y)) d\sigma(y) \\ - a_1 n_1(x) - a_2 n_2(x) = g_2(x) \end{aligned}$$

$$\begin{aligned} \langle \lambda_1, 1 \rangle &= 0, \\ \langle \lambda_1, x_1 \rangle + \langle \lambda_2, n_1 \rangle &= 0, \\ \langle \lambda_1, x_2 \rangle + \langle \lambda_2, n_2 \rangle &= 0, \end{aligned}$$

where $x = (x_1, x_2) \in \partial E$, $n = (n_1, n_2)$, $\oint$ denotes the principal Cauchy value and $a_1, a_2, a_3 \in \mathbb{R}$. Moreover, the jump relation across ∂E is the following:

$$\begin{aligned} g_1(x) - \partial_n(\Delta(L^T))(x) &= -\lambda_1(x), \\ g_2(x) - \Delta(L^T)(x) &= \lambda_2(x), \end{aligned}$$

where L^T is the solution of the following problem:

$$\begin{cases} \Delta^2 L^T = 0, & \text{in } E, \\ \partial_n L^T = \partial_n T, & \text{on } \partial E, \\ L^T = T, & \text{on } \partial E. \end{cases} \tag{7.13}$$

By setting $x = (a\cos(\varphi), b\sin(\varphi))$ and $y = (a\cos(\theta), b\sin(\theta))$ and using the same computation technique of λ_1 and λ_2 in [AD15] pages 18-20, with $g_1 = 0$ and $g_2 = -\Delta v_0(0)$, we show that:

$$\begin{aligned} &\Delta_x(E(x-y)) = -\frac{2}{8\pi}(\log(2(1-\cos(\varphi-\theta)))), \\ &\Delta_x(\partial_{n_y} E(x-y)) = \frac{-1}{4\pi}, \\ &\partial_{n_x}(\Delta E(x-y)) = \frac{-1}{4\pi}, \\ &\partial_{n_x}\Delta(\partial_{n_y}(E(x-y)) = \frac{2}{8\pi(1-\cos(\varphi-\theta))}, \\ &a_0 = a_1 = a_2 = 0, \\ &\lambda_1 = 0 \text{ and } \lambda_2 = k_0^{a,b}\Delta v_0(0) \text{(see details below)}, \\ &\oint_{\partial E} \partial_{n_x}(\Delta(\partial_{n_y} E(x-y)))d\sigma(y) = 0. \end{aligned}$$

We have λ_2 satisfies:

$$\frac{\lambda_2}{2} + \int_{\partial E} \lambda_2 \Delta_x(\partial_{n_y} E(x-y))d\sigma(y) = -\Delta v_0(0),$$

from which we deduce

$$\frac{\lambda_2}{2} - \frac{\lambda_2}{4\pi}\int_{\partial E} d\sigma(y) = -\Delta v_0(0).$$

So if $a \neq b$, we obtain:

$$\lambda_2 = k_0^{a,b}\Delta v_0(0),$$

where

$$k_0^{a,b} = \frac{2\pi}{\frac{1}{2}\int_0^{2\pi}\sqrt{a^2\cos^2(\theta) + b^2\sin^2(\theta)}d\theta - \pi}.$$

Lemma 7.2.2

$$\int_{\partial\omega_\varepsilon} \partial_n w_\varepsilon \Delta u_0 d\sigma(x) = -\varepsilon^2(k_0^{a,b}+1)\Delta v_0(0)\left(k_1^{a,b}\frac{\partial^2 u_0(0)}{\partial x^2} + k_2^{a,b}\frac{\partial^2 u_0(0)}{\partial y^2} + k_3^{a,b}\left(\frac{\partial^2 u_0(0)}{\partial x \partial y} + \frac{\partial^2 u_0(0)}{\partial y \partial x}\right)\right) + o(\varepsilon^2),$$

where

$$k_0^{a,b} = \frac{2\pi}{\frac{1}{2}\int_0^{2\pi}\sqrt{a^2\cos^2(\theta)+b^2\sin^2(\theta)}d\theta - \pi},$$

$$k_1^{a,b} = \int_0^{2\pi}\frac{a^2\cos^2(\theta)}{\sqrt{a^2\cos^2(\theta)+b^2\sin^2(\theta)}}\,d\theta,$$

$$k_2^{a,b} = \int_0^{2\pi}\frac{b^2\sin^2(\theta)}{\sqrt{a^2\cos^2(\theta)+b^2\sin^2(\theta)}}\,d\theta,$$

$$k_3^{a,b} = \int_0^{2\pi}\frac{ab\ \cos(\theta)\sin(\theta)}{\sqrt{a^2\cos^2(\theta)+b^2\sin^2(\theta)}}\,d\theta.$$

PROOF 20 *We have*

$$\begin{aligned}\int_{\partial\omega_\varepsilon} \partial_n w_\varepsilon \Delta u_0 d\sigma(x) &= \int_{\partial\omega_\varepsilon} \partial_n H_\varepsilon \Delta u_0 d\sigma(x),\\ &= \int_{\partial\omega_\varepsilon} \partial_n \varepsilon^2 T(\frac{x}{\varepsilon})\Delta u_0 d\sigma(x) + \int_{\partial\omega_\varepsilon} \partial_n e_\varepsilon \Delta u_0 d\sigma(x),\end{aligned}$$

Using classical calculation techniques as it is done in Lemma 7.2.1, we show

$$\int_{\partial\omega_\varepsilon} \partial_n e_\varepsilon \Delta u_0 d\sigma(x) = o(\varepsilon^2),$$

then, we deduce

$$\int_{\partial\omega_\varepsilon} \partial_n w_\varepsilon \Delta u_0 d\sigma(x) = \int_{\partial\omega_\varepsilon} \partial_n \varepsilon^2 T(\frac{x}{\varepsilon})\Delta u_0 d\sigma(x) + o(\varepsilon^2).$$

By writing $\tilde{u}_0(x) = u_0(x) - u_0(0) - \nabla u_0(0)$*, we get*

$$\int_{\partial\omega_\varepsilon} \partial_n \varepsilon^2 T(\frac{x}{\varepsilon})\Delta u_0 d\sigma(x) = \int_{\partial\omega_\varepsilon} \partial_n \varepsilon^2 T(\frac{x}{\varepsilon})\Delta \tilde{u}_0 d\sigma(x).$$

By applying Green's formula, we obtain

$$\int_{\partial\omega_\varepsilon} \partial_n \varepsilon^2 T(\frac{x}{\varepsilon})\Delta u_0 d\sigma(x) = \int_{\omega_\varepsilon} \Delta(\varepsilon^2 T(\frac{x}{\varepsilon}))\Delta(\tilde{u_0})dx + \int_{\omega_\varepsilon} \nabla(\varepsilon^2 T(\frac{x}{\varepsilon}))\nabla(\Delta(\tilde{u_0}))dx.$$

Using classical calculation techniques as it is done in Lemma 7.1.4, we show :

$$\int_{\omega_\varepsilon} \nabla(\varepsilon^2 T(\frac{x}{\varepsilon}))\nabla(\Delta(\tilde{u_0}))dx = o(\varepsilon^2).$$

Then, we deduce

$$\int_{\partial\omega_\varepsilon} \partial_n \varepsilon^2 T(\frac{x}{\varepsilon})\Delta u_0 d\sigma(x) = \int_{\omega_\varepsilon} \Delta(\varepsilon^2 T(\frac{x}{\varepsilon}))\Delta(\tilde{u_0})dx + o(\varepsilon^2).$$

By applying Green's formula, we obtain

$$\begin{aligned}\int_{\omega_\varepsilon} \Delta(\varepsilon^2 T(\frac{x}{\varepsilon}))\Delta(\tilde{u_0})dx = &\int_{\omega_\varepsilon} \underbrace{\Delta^2(\varepsilon^2 T(\frac{x}{\varepsilon}))}_{=0}\, \tilde{u_0}dx \\ &+ \int_{\partial\omega_\varepsilon} \left[\partial_n \tilde{u_0}\Delta\left(\varepsilon^2 T(\frac{x}{\varepsilon})\right) - \partial_n\left[\Delta\left(\varepsilon^2 T(\frac{x}{\varepsilon})\right)\right]\tilde{u_0}\right] d\sigma.\end{aligned}$$

By using the change of variable $x = \varepsilon y$, we obtain

$$\begin{aligned}\int_{\omega_\varepsilon} \Delta(\varepsilon^2 T(\frac{x}{\varepsilon}))\Delta(\tilde{u_0})dx &= \varepsilon\int_{\partial E} \Delta\left(L^T(y)\right)\partial_n\tilde{u_0}(\varepsilon y)\, d\sigma(y) - \int_{\partial E}\partial_n\left(\Delta(L^T)\right)\tilde{u_0}(\varepsilon y)\, d\sigma(y) \\ &= \varepsilon\int_{\partial E} \Delta\left(L^T(y)\right)\underbrace{\left(\partial_n\tilde{u_0}(\varepsilon y) - \varepsilon\nabla^2 u_0(0)y.n\right)}_{=o(\varepsilon)} d\sigma(y) \\ &\quad +\varepsilon^2\int_{\partial E}\Delta\left(L^T(y)\right)\nabla^2 u_0(0)y.n\, d\sigma(y) \\ &\quad -\int_{\partial E}\partial_n\left(\Delta(L^T)\right)\underbrace{\left(\tilde{u_0}(\varepsilon y) - \frac{\varepsilon^2}{2}\nabla^2 u_0(0)y.y\right)}_{=o(\varepsilon^2)} d\sigma(y) \\ &\quad -\tfrac{\varepsilon^2}{2}\int_{\partial E}\partial_n\left(\Delta(L^T)\right)\nabla^2 u_0(0)y.y\, d\sigma(y) \\ &= \varepsilon^2\int_{\partial E}\Delta\left(L^T(y)\right)\nabla^2 u_0(0)y.n\, d\sigma(y) \\ &\quad -\tfrac{\varepsilon^2}{2}\int_{\partial E}\partial_n\left(\Delta(L^T)\right)\nabla^2 u_0(0)y.y\, d\sigma(y) + o(\varepsilon^2).\end{aligned}$$

According to the jump relation across ∂E and the values of λ_1, λ_2, g_2 and g_1, we deduce

$$\begin{aligned}\int_{\omega_\varepsilon}\Delta\left(\varepsilon^2 T(\frac{x}{\varepsilon})\right)\Delta(\tilde{u_0})dx &= \varepsilon^2\int_{\partial E}(-\lambda_2 + g_2(y))\nabla^2 u_0(0)y.n\, d\sigma(y) + o(\varepsilon^2), \\ &= -\varepsilon^2\left(k_0^{a,b}+1\right)\Delta v_0(0)\int_{\partial E}\frac{\nabla^2 u_0(0)y.y}{\|y\|}\, d\sigma(y) + o(\varepsilon^2).\end{aligned}$$

By setting $y = (a\cos(\theta), b\sin(\theta))$, we show that:

$$\begin{aligned}\nabla^2 u_0(0)y.y = &a^2\cos^2(\theta)\frac{\partial^2 u_0(0)}{\partial x^2} + ab\cos(\theta)\sin(\theta)\frac{\partial^2 u_0(0)}{\partial x\partial y} \\ &+ ab\cos(\theta)\sin(\theta)\frac{\partial^2 u_0(0)}{\partial y\partial x} + b^2\sin^2(\theta)\frac{\partial^2 u_0(0)}{\partial y^2}.\end{aligned}$$

Then, we deduce that:

$$\int_{\omega_\varepsilon} \Delta(\varepsilon^2 T(\frac{x}{\varepsilon}))\Delta(\tilde{u_0})dx = -\varepsilon^2(k_0^{a,b}+1)\Delta v_0(0)\left(k_1^{a,b}\frac{\partial^2 u_0(0)}{\partial x^2} + k_2^{a,b}\frac{\partial^2 u_0(0)}{\partial y^2} + k_3^{a,b}(\frac{\partial^2 u_0(0)}{\partial x \partial y} + \frac{\partial^2 u_0(0)}{\partial y \partial x})\right) + o(\varepsilon^2),$$

where

$$k_0^{a,b} = \frac{2\pi}{\frac{1}{2}\int_0^{2\pi}\sqrt{a^2\cos^2(\theta)+b^2\sin^2(\theta)}d\theta - \pi},$$

$$k_1^{a,b} = \int_0^{2\pi}\frac{a^2\cos^2(\theta)}{\sqrt{a^2\cos^2(\theta)+b^2\sin^2(\theta)}}\,d\theta,$$

$$k_2^{a,b} = \int_0^{2\pi}\frac{b^2\sin^2(\theta)}{\sqrt{a^2\cos^2(\theta)+b^2\sin^2(\theta)}}\,d\theta,$$

$$k_3^{a,b} = \int_0^{2\pi}\frac{ab\ \cos(\theta)\sin(\theta)}{\sqrt{a^2\cos^2(\theta)+b^2\sin^2(\theta)}}\,d\theta.$$

Then, we deduce that

$$\int_{\partial\omega_\varepsilon} \partial_n \varepsilon^2 T(\frac{x}{\varepsilon})\Delta u_0 d\sigma(x) = -\varepsilon^2(k_0^{a,b}+1)\Delta v_0(0)\left(k_1^{a,b}\frac{\partial^2 u_0(0)}{\partial x^2} + k_2^{a,b}\frac{\partial^2 u_0(0)}{\partial y^2} + k_3^{a,b}(\frac{\partial^2 u_0(0)}{\partial x \partial y} + \frac{\partial^2 u_0(0)}{\partial y \partial x})\right) + o(\varepsilon^2).$$